MONOPULSE WIDEBAND WAVEGUIDE BASED TRAVELLING WAVE ARRAY ANTENNA

A THESIS SUBMITTED TO
THE GRADUATE SCHOOL OF NATURAL AND APPLIED SCIENCES
OF
MIDDLE EAST TECHNICAL UNIVERSITY

BY

GÖKHAN GÜLTEPE

IN PARTIAL FULFILLMENT OF THE REQUIREMENTS
FOR
THE DEGREE OF MASTER OF SCIENCE
IN
ELECTRICAL AND ELECTRONICS ENGINEERING

SEPTEMBER 2017

Approval of the thesis:

MONOPULSE WIDEBAND WAVEGUIDE BASED TRAVELLING WAVE ARRAY ANTENNA

submitted by **GÖKHAN GÜLTEPE** in partial fulfillment of the requirements for the degree of **Master of Science in Electrical and Electronics Engineering Department, Middle East Technical University** by,

Prof. Dr. Gülbin Dural Ünver
Dean, Graduate School of **Natural and Applied Sciences** ________________

Prof. Dr. Tolga Çiloğlu
Head of Department, **Electrical and Electronics Engineering** ________________

Prof. Dr. Özlem Aydın Çivi
Supervisor, **Electrical and Electronics Eng. Dept., METU** ________________

Examining Committee Members:

Prof. Dr. Sencer Koç
Electrical and Electronics Eng. Dept., METU ________________

Prof. Dr. Özlem Aydın Çivi
Electrical and Electronics Eng. Dept., METU ________________

Prof. Dr. Gülbin Dural
Electrical and Electronics Eng. Dept., METU ________________

Assoc. Prof. Dr. Lale Alatan
Electrical and Electronics Eng. Dept., METU ________________

Prof. Dr. Vakur B. Ertürk
Electrical and Electronics Eng. Dept., Bilkent University ________________

Date: 12.09.2017

I hereby declare that all information in this document has been obtained and presented in accordance with academic rules and ethical conduct. I also declare that, as required by these rules and conduct, I have fully cited and referenced all material and results that are not original to this work.

Name, Last Name: GÖKHAN GÜLTEPE

Signature :

ABSTRACT

MONOPULSE WIDEBAND WAVEGUIDE BASED TRAVELLING WAVE ARRAY ANTENNA

Gültepe, Gökhan
M.Sc., Department of Electrical and Electronics Engineering
Supervisor : Prof. Dr. Özlem Aydın Çivi

September 2017, 87 pages

A novel, travelling-wave, waveguide-based antenna array structure with dual-plane monopulse capability is developed. It is an end-fed, broad wall longitudinal slotted, ridged waveguide-based printed antenna array. Even if the structure is scalable, it is designed to operate in S-band. The structure consists of printed antennas on two interleaved waveguide arrays whose dimensions are shrinked to make interleaving operation possible to keep inter-element spacings the same in both the azimuth and elevation planes. The inherently wideband printed antennas, linearly tapered slot antennas (LTSA), are excited via probes inserted into the waveguides to control the amplitude of the radiated E-field to generate desired sum and difference patterns. These LTSAs are expected to eliminate the narrow frequency characteristics of the slots on waveguides, and to improve the bandwidth. Besides, the unit cell of the array is modelled as 5-port networks to handle the couplings between array elements by using their scattering parameters. The array with desired radiation patterns is generated by a code implementation, which chooses the preoptimized array elements with proper radiation control parameters in MATLAB™. Also, a method to improve radiation patterns

is presented to ease the coupling related degredations in the radiation patterns. Finally, a 30-element monopulse array with 25 dB Taylor and Taylor-like difference distributions is generated in MATLAB^{TM}, simulated in HFSS^{TM}, and manufactured. The manufactured array is measured in planar near-field measurement setup, and the measurement results are verified after the comparison with the simulated ones.

Keywords: Slotted Waveguide Arrays, Printed Antennas, LTSA, Travelling Wave Arrays, Monopulse Radar.

ÖZ

TEK DARBE GENİŞ BANTLI DALGA KILAVUZU TABANLI İLERLEYEN DALGA DİZİ ANTEN

Gültepe, Gökhan
Yüksek Lisans, Elektrik ve Elektronik Mühendisliği, Bölümü
Tez Yöneticisi : Prof. Dr. Özlem Aydın Çivi

Eylül 2017 , 87 sayfa

Tek darbe kabiliyetine sahip, yeni bir ilerleyen-dalga, dalga kılavuzu bazlı baskı devre anten dizisi geliştirilmiştir. Bu, sondan beslemeli, yarıkları uzun kenarda iletim yönüne paralel açılmış, sırtlı dalga kılavuzu tabanlı baskı devre anten dizisidir. Yapının boyutları istenilen frekans bandına göre oranlanabilir olsa da, bu tezde S-bantta çalışacak şekilde tasarlanmıştır. Elemanlar arası mesafeyi yanca ve yükselişte korumak için boyutları küçültülmüş ve böylece iç içe geçmesine olanak sağlanmış iki dalga kılavuzu dizi üzerine yerleştirilmiş baskı antenlerden oluşmaktadır. Geniş bantlı baskı devre antenler, LTSA'lar, uygun toplam ve fark örüntülerini üretecek şekilde dalga kılavuzları içerisine daldırılmış miller tarafından uyarılmaktadırlar. Bunların, dalga kılavuzlarındaki yarıkların dar frekans özelliklerini ortadan kaldırması ve dizinin bant genişliğini artırması beklenmiştir. Bunun yanı sıra, dizinin birim elemanının S-parametreleri kullanılıp 5-kapılı bir kutu olarak ifade edilmesiyle elemanlar arası etkileşimlerin de modellenmesi sağlanmıştır. İstenilen ışıma örüntülerini sağlayabilen dizi, önceden en uygun duruma getirilmiş dizi elemanları arasından uygun ışıma kontrol parametrelerine sahip dizi elemanlarını seçen ve onların S-parametrelerini aşamalı olarak birbirine bağlayan bir kod yardımıyla MATLAB^{TM} ortamında modellenmiştir. Ayrıca, ışıma örüntülerini iyileştiren bir yöntem de sunulmuştur. Sonuçta, 30 elemanlı ve 25 dB Taylor ve Taylor'a benzeyen fark dağılımına sahip bir dizi MATLAB^{TM} ortamında modellenmiş, HFSS^{TM} yazılımında benzetim yapılarak doğrulanmış ve üretilmiştir. Üretilen dizi, düzlemsel yakın alan ölçüm yöntemi uygulanarak elde edilen sonuçların benzetim yöntemindekilerle karşılaştırılmasıyla doğrulanmıştır.

Anahtar Kelimeler: Yarıklı Dalga Kılavuzu Diziler, Baskı Devre Antenler, LTSA, İlerleyen Dalga Tipi Diziler, Tek Darbe Radarlar.

To my recently deceased uncle and my colleague

M. Murat Araol

ACKNOWLEDGMENTS

The author would like to express his sincere gratitude to his supervisor Prof.Dr. Özlem Aydın Çivi, for her support, guidance, and technical suggestions and comments throughout the study.

The author would like to thank and express his deep and sincere appreciation to his colleague Doğanay Doğan for proposing this topic to him, and providing motivation, support and his valuable experience throughout the study.

The author is grateful to Aselsan for providing both financial and technical opportunities to complete this study.

The author thanks to Ömer Faruk Yalım and Volkan Altunsoy for their help in manufacturing process.

The author is very thankful to Ozan Ağma, Gizem Aktaş, Selin Aktaş, Sena Alkış, Mehmet Gökcan Bayrak (a.k.a. Gönenç), Osman Cerlet, Berkay Çalışkan, Tolga Dağdelen, Ömürcan Demiralp, Arda Deveci, Ece Durmaz, Ozan Hazır, Oğuzhan Kaya, Barış Karademir, Dilem Karakaya, Enis Kobal, Abdullah Onur Koyuncu, Semih Küçük, Meltem Parlak, Murat Özatay, Fırat Taban, Büşra Timur, Taylan Yapıcı, Burak Alptuğ Yılmaz for their invaluable friendship and support. An 11-year old friendship with most of them shaped my life in happy, sad, and funny moments.

The author wishes to thank to his family for providing every possible support, motivation, and patience. This study would be hard to finish without their encouragement and faith.

The author is grateful to his deceased uncle M. Murat Araol, who is also an electrical engineer, for his encouragement, faith, and support.

TABLE OF CONTENTS

LIST OF TABLES

TABLES

LIST OF FIGURES

FIGURES

LIST OF ABBREVIATIONS

ECCM	Electronic Counter-countermeasure
LTSA	Linearly Tapered Slot Antenna
PEC	Perfect Electric Conductor
PML	Perfectly Matched Layer
SLL	Side Lobe Level
SWGA	Slotted Waveguide Array
VSWR	Voltage Standing Wave Ratio

CHAPTER 1

INTRODUCTION

This introductory chapter articulates the background and motivation of the study. Expressing the current state of the issue, the purpose and the brief explanation of the study mentioned. Finally, the outline of the thesis is given.

1.1 Background of the Study

Slotted waveguide arrays serve feasible solutions to several applications, such as radars. This is because they are suitable for high power systems, and producible to relatively low costs while they provide mechanical durability. Also, using row phase shifters, they can have scanning ability.

Modern radars demand to locate and track the location of a target precisely by using only one RF pulse, considering electronic counter-countermeasure (ECCM) methods. For this reason, slotted waveguide arrays are made capable of performing monopulse operation in one dimension with the use of a proper beamforming network including row phase shifters. Nevertheless, the rows require special aperture distribution as they provide inherent beamforming. For example, a travelling-wave array is designed to have monopulse capability with interleaved rows. Its adjacent rows are excited using distinct aperture distributions synthesized from Taylor and Bayliss amplitude taper distributions [1]. The interleaved rows have the same beam squint angle, propagation constant and slot spacing. To maintain the element spacing among the rows of the interleaved arrays, waveguide dimensions are shrinked using ridges. However, this poses a limitation on the frequency bandwidth of the slots, which is around 6%. To ease this impact, the slots are opened as tilted on broad wall, but they impose high cross-polarization, resulting in butterfly lobes.

1.2 Purpose of the Study

In order to overcome restrictions mentioned in Section 1.1, a novel hybrid antenna structure, introduced in the literature as the first time, with a pending patent application [2] is proposed in this thesis. It is an end-fed, ridged, broad wall slotted, travelling-wave, interleaved waveguide array exciting the printed antennas inserted in the slots etched on waveguides. It is low loss and low profile. When saying low profile, it is, of course, a little larger in depth from a conventional slotted waveguide array due to the geometry of the hybrid structure. Yet, it is much smaller compared to monopulse antenna arrays with stripline divider networks in [3] if low loss structures are concerned. It performs dual-plane monopulse operation with the use of simultaneous sum and difference patterns obtained by using interleaved waveguide arrays. There is a beamformer network in one plane to decrease the number of T/R (Transmit/Receive) blocks. To do so, a waveguide array is used.

An illustration of the proposed array is given in Figure 1.1. It can be seen that there are interleaved sum and difference rows. The elements in any row, and the rows of sum or difference arrays are separated by a distance d. That is, one element of sum or difference arrays fits in an area of d/2 by d. The distance d is 50 mm in this design. Since a waveguide row could not fit into standard WR284 dimensions (72.136 mm x 34.036 mm) for S-band, a ridged waveguide is designed. A printed antenna is placed and fed by a probe inserted into a slot opened on the broad wall of waveguides. The use of printed antennas improves the frequency bandwidth of closely spaced waveguide arrays, operates in at least 15% bandwidth.

Thus, without violating much the low profile specification of the array due to shrinked dimensions, a low loss antenna array offering dual plane monopulse operation is realized by using this novel configuration. It is concluded that using slotted waveguides as a beamformer of printed antennas in one dimension enhances the bandwidth of closely spaced slotted waveguide arrays. In the other dimension, digital beamform-

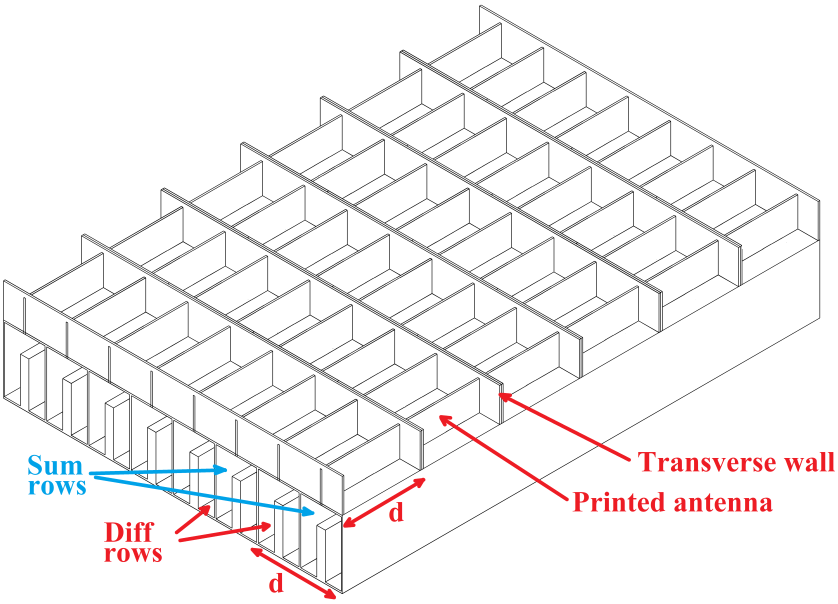

Figure 1.1: An illustration of a portion of the proposed hybrid array [2]

ing can be used to obtain any desired pattern. Finally, the full array is demonstrated in Figure 1.2.

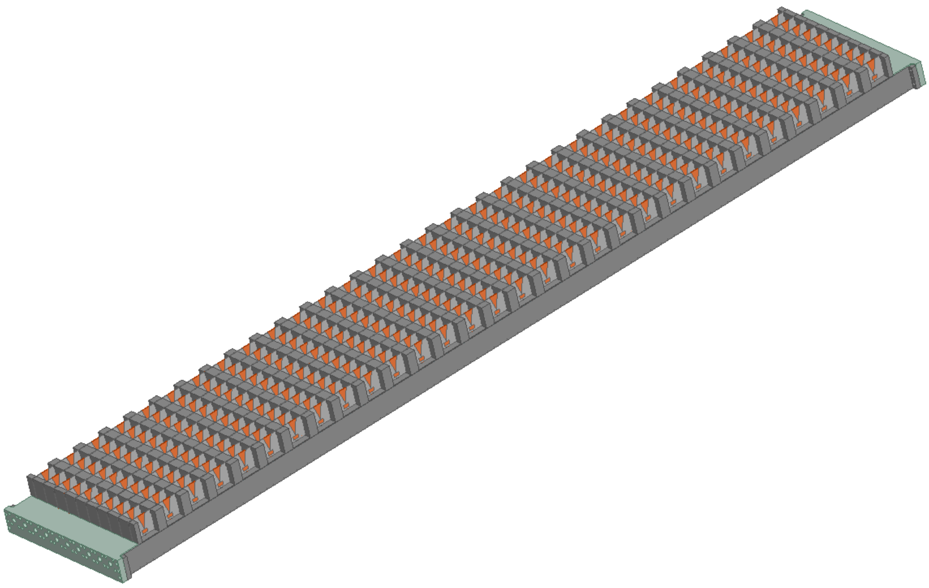

Figure 1.2: The full monopulse array structure

1.3 Organization of the Thesis

A brief literature survey about the issues related to the proposed structure is presented in Chapter 2. Slotted waveguide arrays, the radiation mechanism of rectangular slots, resonant and non-resonant arrays, the principle of operation of radars and especially monopulse radars are expressed.

In Chapter 3, a novel slotted waveguide-based printed antenna is brought into focus. The geometry of the proposed hybrid radiating element is demonstrated, and the radiation mechanism of the element is expressed in detail. Also, the unit cell design of the hybrid radiating element for monopulse radar antenna is illustrated, considering the infinite array approach.

Chapter 4 concentrates on a planar array designed with the use of the unit cell described in Chapter 3. The hybrid design method of the array which models it as a multi-port network is explained. Indeed, the method chooses antenna elements satisfying the requirements, and cascades scattering parameters of them to create a linear array, which is the unit cell of the planar array. Next, the radiation patterns formed by the array are obtained by a code implementation in MATLAB™. The array is modelled in HFSS™, and the patterns attained from different programs are compared to verify the method.

Chapter 5 demonstrates the obtained radiation patterns. Then, it describes a synthesis method to improve those patterns. Hence, it illustrates the final sum and difference radiation patterns.

In Chapter 6, the monopulse array prototype and its manufacturing process are mentioned as well as the coaxial to waveguide adapter designed for the array to be measured in anechoic chamber. Then, the measurement results are given.

Finally, an assessment of the overall accomplishments of this study takes place in Chapter 7, as well as the discussion about future work for further improvement.

CHAPTER 2

LITERATURE SURVEY

2.1 Slotted Waveguide Arrays

Slotted waveguide array (SWGA) has been a promising alternative in radar applications since the World War II [4]. It provides relatively inexpensive, easily manufacturable, low loss, low profile, more efficient, high power and more durable solutions with respect to its counterparts.

In the early studies of Stevenson, Stegen, and Oliner, a waveguide was turned into a radiating aperture by coupling the internal fields of it to the slots opened on one of its walls [5, 6, 7]. Indeed, the slots were excited by discontinuity of the surface currents on the waveguide walls in the vicinity of them, which explains briefly the radiation mechanism behind the slotted waveguide arrays. Later, Elliot accomplished modelling of the slots via their admittances [8, 9].

2.1.1 Rectangular Waveguide Slots

The fundamental mode in a rectangular waveguide is TE_{10} mode. The fields of this mode have a sinusoidal variation in the transverse directions, and a cosinusoidal one in the axial or propagation direction. The surface currents due to the H-field are illustrated in Figure 2.1 when the boundary conditions are applied to the waveguide walls.

Looking at the surface current distribution demonstrated in Figure 2.1, it can be deduced that if a slot geometry interrupts the surface currents, there exists an induced

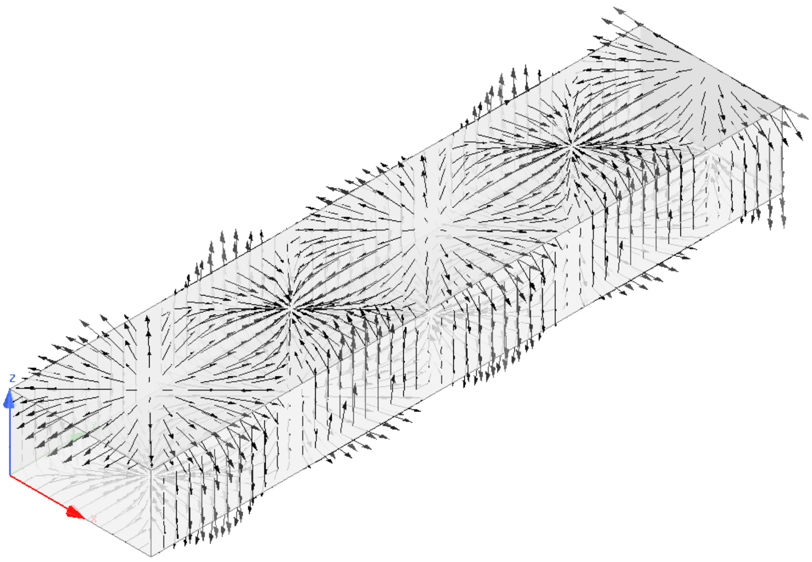

Figure 2.1: Surface currents for TE_{10} mode

E-field across the long edges of that slot. This leads the slot to radiate. There is an important point that the slot is thin in one of its directions; otherwise, it should be considered as an aperture because the slot also disturbs the surface currents in the other direction. There are various slot types, such as offset broadwall slots, inclined broad wall slots, and inclined edge wall slots etc. [8]. The slot geometries are depicted in Figure 2.2.

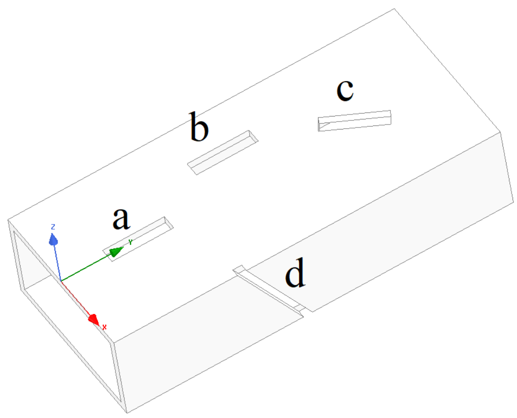

Figure 2.2: Several types of slots: (a) longitudinal broadwall slot, (b) longitudinal offset broadwall slot, (c) inclined broadwall slot, (d) inclined edge wall slot

Non-offset longitudinal broad wall slot in Figure 2.2(a) does not radiate since the currents have a null at the longitudinal bilateral axis of the waveguide. However, if the same slot is opened to the broad wall with an offset as in Figure 2.2(b), it starts behaving as a radiator. The larger the offset is, the higher the radiated power from the slot becomes. For the inclined slots in Figure 2.2(c) and (d), the radiated power goes up with an increase in the inclination angle [8].

Besides, it has been proven that the slots, such as the ones in Figure 2.2 (b) and (d), disturbing the transverse surface currents can be modelled as shunt admittances, whilst the ones as in Figure 2.2 (c) interrupting the axial surface currents can be considered as series impedances [10]. The shunt and series model illustrations are given in Figure 2.3 and Figure 2.4, respectively. When the transmission line design approach is considered, the conductance or the resistance of the slot for the shunt and the series representations, respectively, is mostly determined by the offset or the inclination angle of it, whereas the susceptance or the reactance of the slot depends on the length of it. For instance, a resonant slot whose length is a half guided wavelength has an impedance with a zero imaginary part [11]. That is, the susceptance or the reactance is zero in resonance.

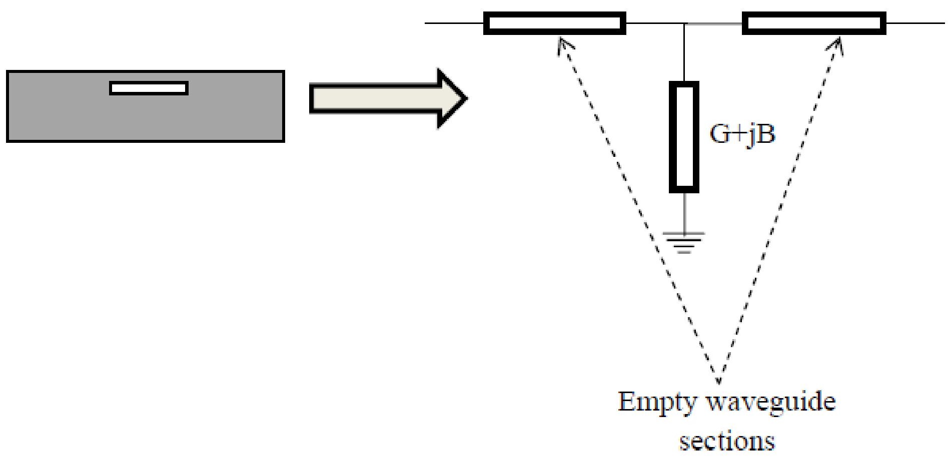

Figure 2.3: Shunt representation of the longitudinal offset broadwall slot [11]

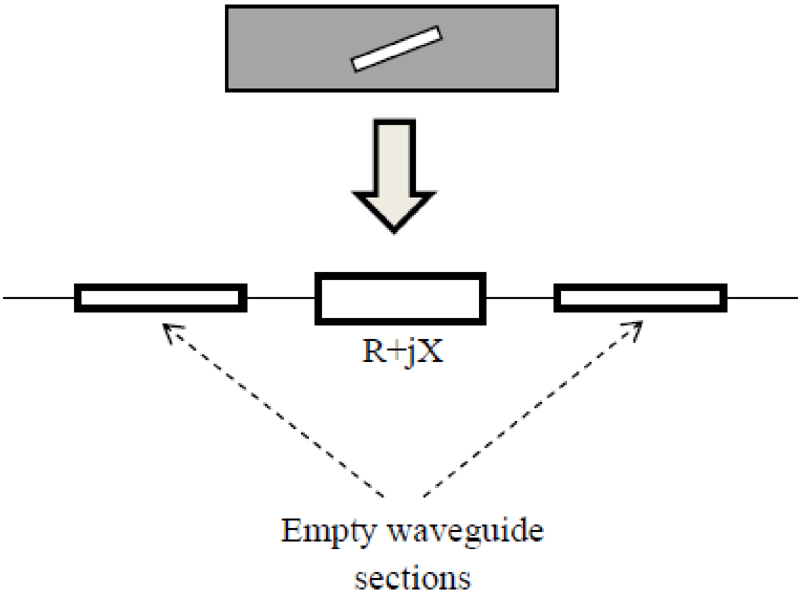

Figure 2.4: Series representation of the inclined broadwall slot [11]

2.1.2 Array Types

Slotted waveguide arrays can be categorized into two groups namely, travelling wave or non-resonant arrays, and standing wave or resonant arrays.

2.1.2.1 Standing Wave Type Arrays

A resonant type slotted waveguide array is excited by a standing wave due to a short circuit termination one or three quarters of a guided wavelength away from the last slot. The slot spacing is kept as a half guided wavelength at the center frequency. The array is fed from the center, and the feed point is a quarter wavelength away from the left and right nearest slots' centers. In this configuration, the admittances of the slots normalized with respect to the characteristic admittance of the waveguide are added up to 1 from the short termination to the feed point for each rows' left and right sides [11]. The imaginary part of the input impedance becomes zero only at the center frequency, which results in a resonant behavior.

In addition, there occurs a 180 degree phase difference between sequential slots due to the half guided wavelength slot spacing. To make all the slots in-phase for a broadside array, the successive slots are placed accordingly to cancel this phase reversal. For instance, consecutive offset longitudinal broad wall slots are placed at different sides of the longitudinal bilateral axis. In this way, the main beam is at boresight independent of the operating frequency.

With the above mentioned slot spacings, voltage maxima occur at slot centers, and the radiation from each slot becomes in-phase when their admittance angles are designed to be the same. However, as the operating frequency deviates from the center frequency, this voltage pattern becomes degenerate, and the radiation pattern deteriorates. This is why it is called as a resonant array. The degradation is more severe for the slots further away the feed point at the center of the array; hence, the frequency bandwidth gets narrower as the number of slots increases. The resonant type is not a smart choice to make a large array with low side lobe and large frequency bandwidth [11].

2.1.2.2 Travelling Wave Type Arrays

A non-resonant type slotted waveguide array is excited by a travelling wave since waveguide is terminated with a load where the remaining or non-radiated power is absorbed. The wave travelling through the waveguide excites the slots regardless of the slot locations. Yet, the slot spacing should be different from and not be very close to a half guided wavelength. Otherwise, the reflections from the slots are summed up in-phase, and it deteriorates the array performance [10]. At the same time, the radiating elements should have reflections as low as possible.

Furthermore, there occurs a phase difference between sequential slots as a product of the slot spacing and the propagation constant. Because of this, the main beam deviates from broadside. To decrease the angle of deviation, the same phase reversal operation as in resonant case is performed in non-resonant array [11]. Giving additional 180 degree phase shift, main beam occurs at a low squint angle near boresight. In this case, the squint angle of the main beam changes with the operating frequency. This is unintentional when there is a need for wide instantaneous bandwidth, but it can be still used in other applications. Non-resonant array offers a wider frequency bandwidth than its resonant counterpart does since the excitation of the slots is independent of the slot spacing. Yet, the array performance can still degrade owing to the fluctuation in the slot conductances with changing frequency.

2.2 An Overview of Monopulse Radars

A radar, accounting for radio detection and ranging, is a device which can find the location of a target with respect to its location. It basically sends a short RF pulse as an electromagnetic wave propagating through space. When the radiated electromagnetic wave faces a reflective target, some of the energy is scattered back towards the radar. Radar is capable of determining the location of the target after receiving and processing the echo signal.

Radar consists of many parts, one of which is an antenna. It converts the incident RF signal into an electromagnetic wave propagating through space, and vice versa. It also shapes the radiated energy; for instance, it narrows the main beam to increase directivity and gain so as to improve angular resolution and the quality of the reception of weak echo signals.

Besides the determination of the position of an object, a radar is able to track an object. A method of tracking is scanning the area in the vicinity of the target. In other words, the radar directs its beam around the target on a circular path sequentially in time as depicted in Figure 2.5 [12]. Collecting the echo signals in consecutive time divisions, and comparing the amplitude of them, the location of the target can be tracked. Actually, this method is devised after the concept of lobe switching or sequential lobing, which sequentially generates two beams slightly tilted to either side of boresight [12]. The target's location is on the side in which the antenna receives a stronger signal from either one of these two beams.

Nonetheless, these methods are vulnerable to the errors due to the amplitude fluctuations over time arising from weather conditions, electronic countermeasures and the motion of the target. Any combination of them may lead to false positioning, so monopulse radar was developed as a solution.

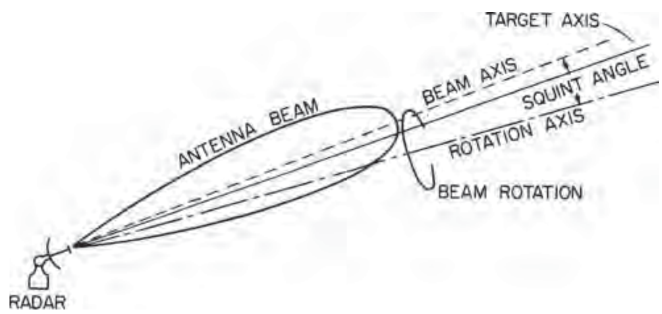

Figure 2.5: Conical scan [12]

Monopulse radar was devised to overcome conical scanning radars' vulnerability to unpredicted amplitude fluctuations between successive bursts in time. It samples the received echo corresponding to a single RF pulse via two simultaneous channels with offset beams. Since the sampling in the two channels is performed at the same time, it discards the possibility of amplitude fluctuations. Even if they require more complex hardware, modern monopulse radars have advantages over conical scanning ones since they provide more efficient and accurate angle measurement. Yet, in some applications, conical scanning radars are more practical and useful [12].

There are two basic types of monopulse, namely amplitude-comparison and phase-comparison monopulse [13]. In the amplitude-comparison type, there are two offset beams overlapping and intersecting at the null axis as illustrated in Figure 2.6. When a signal received from a direction deviated from that axis, the signal strengths in the two channels differ. The magnitude of that difference gives the angular position of the received signal with respect to null axis, whilst the sign of it determines in which side of the null axis the signal exists. In the phase-comparison type, the angular direction of the target is found by looking at the phase difference of signals received by two antennas. That the distances between the phase centers of the antennas and the location of the target are different leads to an inherent phase difference among channels [14].

There is, also, another angle-sensing method, namely sum-and-difference. In this method, the direction can be found with the use of amplitude or phase comparison, but the angular measurements are performed by sum-and-difference discriminator. In common, amplitude comparison is used for sum-and-difference monopulse radars

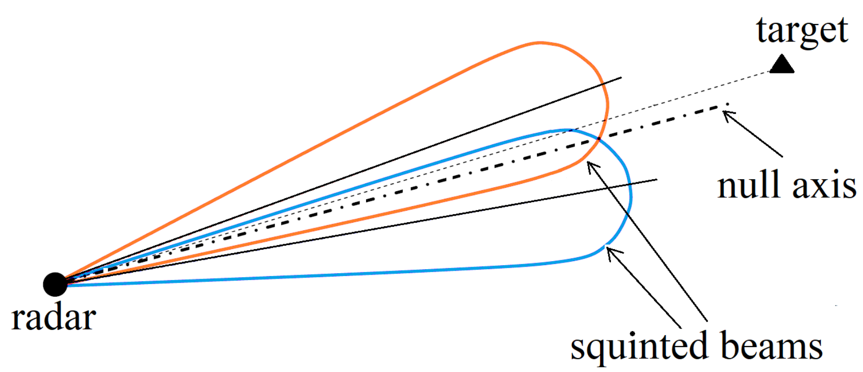

Figure 2.6: Amplitude-comparison monopulse radiation patterns

[11]. The radiation patterns of the channels are called as sum and difference, and shown in Figure 2.7.

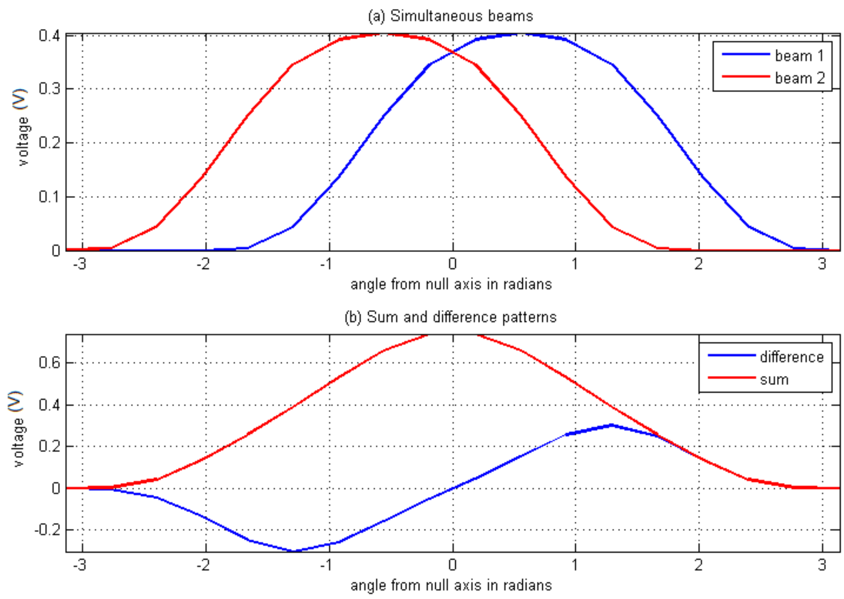

Figure 2.7: (a)Simultaneous beams, (b)Sum and difference radiation patterns

It can be seen in Figure 2.7 that the signal in the difference channel changes its phase with respect to the incoming signals' angular position to the null axis. Also, at the null axis, the difference channel has a signal with zero amplitude. So, the difference channel is used to check the beam direction with respect to the target tracked when the sum channel is taken as a reference source. Since the sum channel has a pattern like pencil or fan beam, it is used to determine the range and velocity of the target [14].

Furthermore, in order to obtain efficient sum-and-difference patterns, special excitation distributions are used. These provide low side lobe level, null axis with a large slope, and narrow beamwidth, considering a phased array with a corporate feed network including phase shifters and attenuators. Taylor and Bayliss tapers for sum and difference patterns, respectively, are common efficient distributions used for monopulse operation to achieve previously mentioned specifications [15]. Sample Taylor and Bayliss distributions to give 40 dB side lobes are demonstrated in Figure 2.8, and corresponding sum and difference channel patterns are depicted in Figure 2.9.

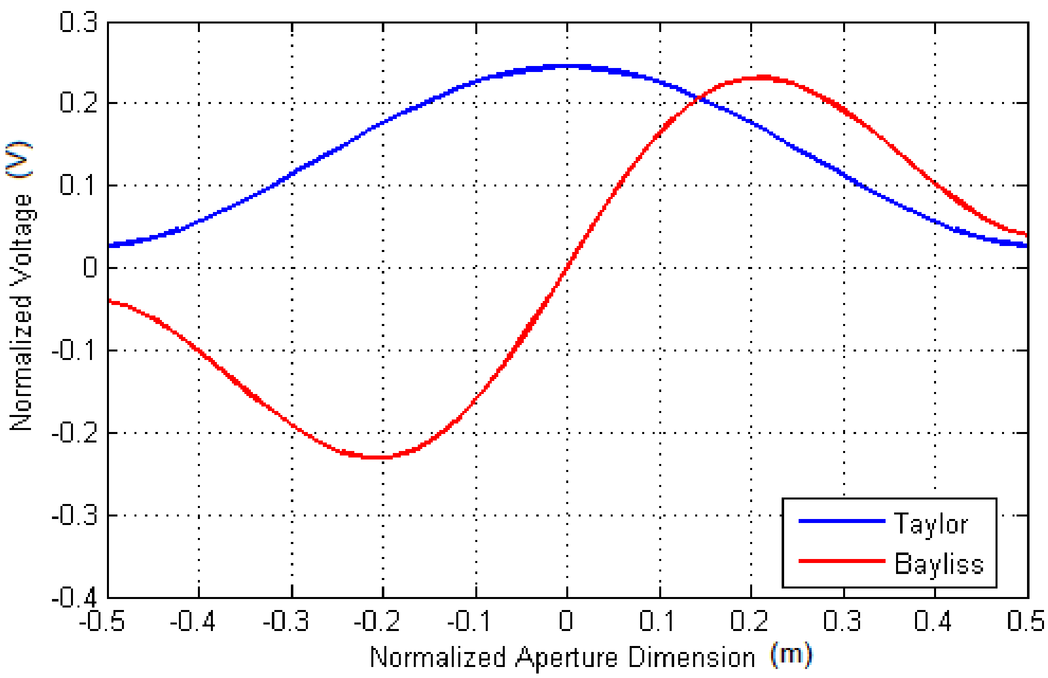

Figure 2.8: An example of Taylor and Bayliss distributions

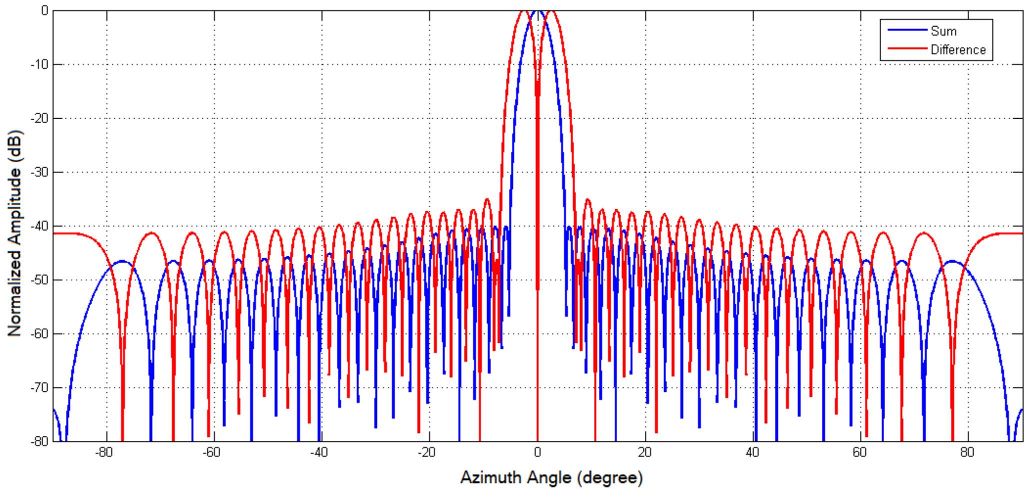

Figure 2.9: Sum and Difference patterns for 40 dB Taylor and Bayliss taper

2.2.1 Monopulse Antenna Structures

Basic monopulse approach uses 4 horn antennas placed on a 2-by-2 rectangular grid, and it is explained in detail by Barton and Sherman in [16], as well as its successors and the applications in an array environment.

Similarly, modern monopulse antenna arrays divides the aperture into 4 quadrants to obtain sum and difference patterns in azimuth and elevation as described in [18] and [19]. A visualization of a monopulse array in this configuration is given in Figure 2.10. By the way, several large monopulse arrays using this method like Russian Zhuk-ME AESA radar array are given in [17].

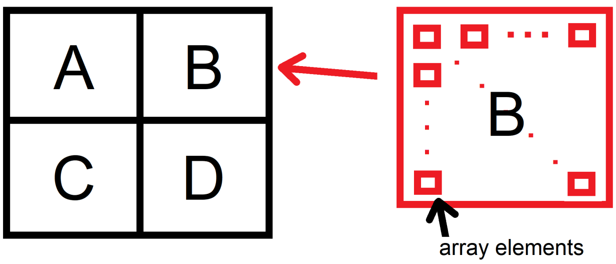

Figure 2.10: Quadrants on an array aperture

In this configuration, sum pattern is obtained by summing the inputs from all quadrants:

$$\sum = A + B + C + D \tag{2.1}$$

where A, B, C, and D represents the beamformed patterns of the quadrants.

There are two difference patterns to be obtained, namely elevation and azimuth difference patterns. According to the configuration in Figure 2.10, they can be obtained by:

$$\Delta_{elevation} = (A + B) - (C + D) \tag{2.2}$$

$$\Delta_{azimuth} = (A + C) - (B + D) \tag{2.3}$$

A, B, C, and D can be obtained by a combiner network or a digital beamforming circuitry. For instance, a microstrip patch antenna array can perform monopulse operation when there is a microstrip divider/combiner feed network added as in [20]. Also, a dipole array fed by a low loss stripline network for monopulse operation is presented by Kinsey in [3]. It has 180°hybrid couplers to obtain sum and difference patterns in azimuth plane. The same configuration is realized on waveguides using magic tees in [21].

Besides, for low-loss applications, a slotted waveguide array is a promising solution, as well as being low profile and light-weight. It is actually an inherent beamformer of many elements. Yet, due to their non-resonant behavior, travelling-wave type of arrays are, generally, preferred. For a travelling-wave waveguide array design, the aperture is divided into 2, instead of 4 as in Figure 2.10. For instance, A and B, C and D are combined by interleaving two arrays as depicted in Figure 2.11, where d is the element spacing in both azimuth and elevation planes.

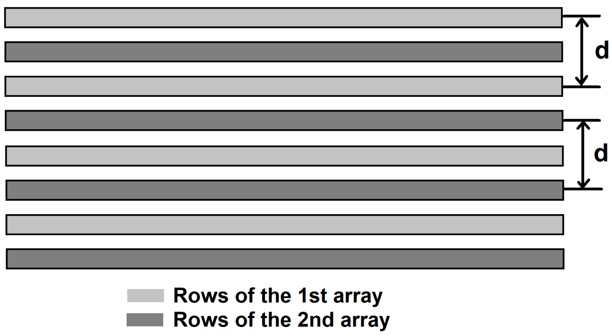

Figure 2.11: Interleaved waveguide arrays

To perform monopulse operation, 1st and 2nd arrays are made to have main beams with different squint angles [22]. That is, the arrays are designed to have different propagation constants. Or, they are excited by different modes [23]. Both of them have overlapped beams to have monopulse operation. However, these have sensitivity and gain related problems [1]. So, the interleaved arrays are designed to have identical propagation constants and inter-element spacings. This provides that the main lobe of sum and two-lobe of difference patterns keep overlapping even if the operating frequency changes. For instance, the 1st array in Figure 2.2 is designed as a sum array, whereas the 2nd one is difference array [24]. Hence, monopulse operation is handled in azimuth plane. In elevation, the data collected from the rows are combined after necessary phase-shifter and attenuator arrangements.

In this study, a novel structure based on an interleaved waveguide array like in [24] is presented. There are hybrid structures in literature like the one in [25], which is a series-fed patch array where the center elements are fed by a SWGA. However, the hybrid structure proposed in this study is completely different and novel, and especially designed for monopulse operation. In fact, it has interleaved sum and difference arrays, but the radiating element is not a slot on a waveguide but a printed antenna fed by a probe inserted in slotted waveguide. Printed antenna with wideband characteristics is chosen so that the proposed array has wider bandwidth compared to conventional slotted waveguide arrays. Besides, the array is still be considered as a light-weight and a low profile one due to the shrinkage of the waveguide dimensions for interleaving.

CHAPTER 3

A NOVEL SLOTTED WAVEGUIDE-BASED PRINTED ANTENNA

This chapter shows and explains the design steps and the characterization of the novel antenna structure. As both sum and difference arrays are to be fitted into the same aperture area by interleaving their rows like interdigitated ones, the waveguide dimensions should be shortened. So, an appropriate waveguide, at first, is designed since the waveguides used are non-standard. Next, a carefully designed printed antenna is integrated to the waveguide. The characterization is performed using infinite array approach, so the mutual coupling between the antenna elements are taken into consideration. The data extracted from the characterization, later, will be used to design an array presented in Chapter 4.

Before starting to explain the details of the design, the requirements of the design are determined:

- Antenna operates in S-band between 2.9 and 3.3 GHz
- Antenna performs dual-plane monopulse operation.
- Antenna generates simultaneous sum and difference patterns.
- A row of the antenna has 30-elements.
- SLL of the antenna is -25 dB.
- There is a fixed beamformer in one dimension to reduce the number of T/R blocks.

- The reflection from each element should be low enough to be cascaded for a travelling-wave array design.
- The radiation phase and amplitude of each radiating element should be easily controlled.
- The printed antennas inserted in the slotted waveguide should allow monopulse operation in a large frequency band while they are closely spaced in one dimension.
- The amplitude of radiation from the unit cell of hybrid structure can vary in a large range for amplitude tapering to design an array with low side lobes.
- Antenna should be low loss and low profile.
- The structure should be easily manufactured.
- The design process should be reliable and simple.

For a low loss and low profile design, slotted waveguide array is considered. Otherwise, the beamforming network will be lossy. For instance. The loss for Rogers 4003 substrate around 3 GHz is 0.05 dB/inch [26]. Considering a 30-element array with 50 mm element spacing, the loss is approximately 3 dB for a row. On the other hand, the loss of a aluminum waveguide around 3 GHz is 0.001 dB/inch [27]. Even if the loss specification is satisfied by choosing a waveguide solution, regular slotted waveguide arrays are mostly narrow band. This is even worse when the rows of them are closely spaced. Since the design requires nearly 15% bandwidth, regular waveguide solutions do not fulfill the requirement. Hence, in this study, a new antenna structure based on slotted waveguide arrays is proposed. Creating a hybrid structure composed of a slotted waveguide and printed antennas seems to be a solution to the bandwidth limitation. This is because printed antenna elements can offer wideband solutions.

Besides, when it comes to manufacturability, PCB antennas can be easily produced with high accuracy. And, waveguides can be simply produced with CNC milling techniques.

3.1 A Proper Ridged Waveguide Design

The proposed array structure consists of two interleaved arrays for sum and difference radiation patterns. Because of this, the waveguide dimensions should be shortened in order to maintain the inter-element spacing d in both azimuth and elevation planes of the planar array to avoid grating lobes as illustrated in Figure 3.1. A closer view is given in Figure 3.2. To do so, a ridge is placed through the waveguide. For the travelling-wave array, the element spacing d is kept away from a half guided wavelength λ_g, and is 0.36 guided wavelength λ_g at the design frequency which is also the center frequency. This spacing d corresponds to nearly a half free-space wavelength ($0.5\ \lambda_0$) at the center frequency. As 2 rows should fit into this spacing, the width of each row with the wall thickness is made to be 0.18 guided wavelength λ_g. So, a ridged waveguide is designed, as shown in Figure 3.3, in HFSS™, satisfying this limitation.

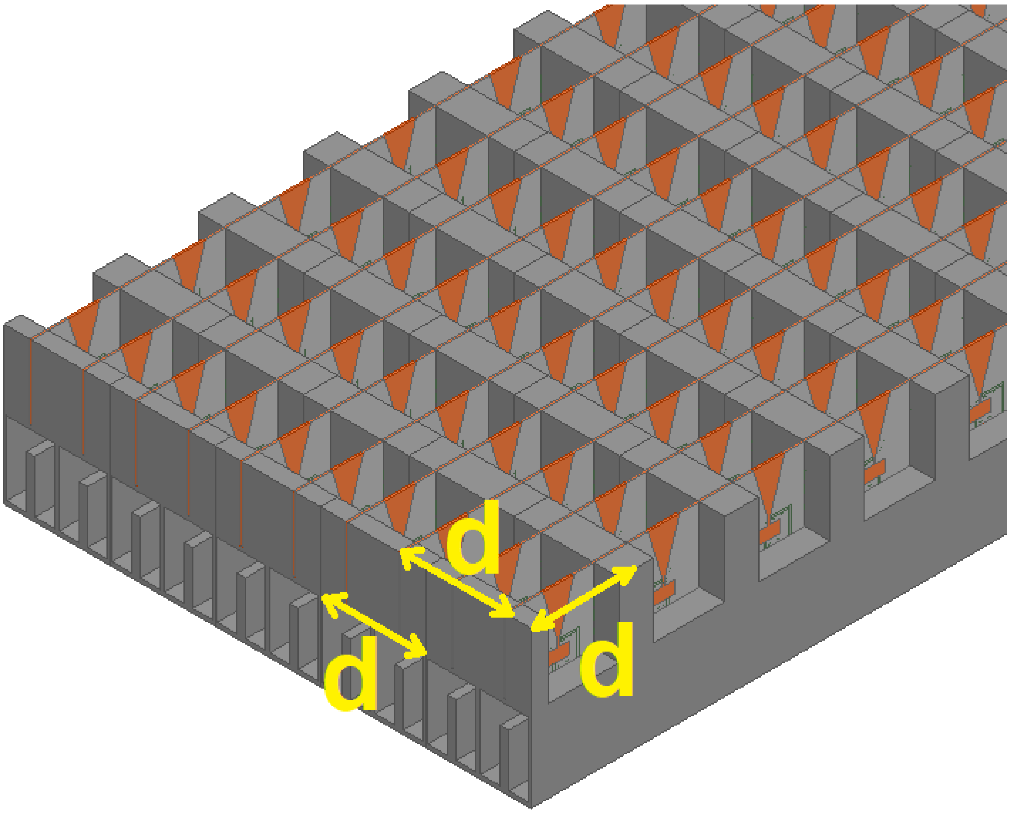

Figure 3.1: Dimension shrinkage to keep inter-element distance d constant

It is known that placing a ridge to narrow the waveguide dimension where the strongest E-field occurs lowers the cut-off frequency of the waveguide [28]. Chen gives the calculation of the ridge parameters in [28]. In this design, the ridge height and width is optimized in HFSS™ to make the cut-off frequency below the operating frequency band of the waveguide. In Table 3.1, the dimensions of the ridged waveguide are given, as well as the standard WR284 dimensions. The cut-off frequency is placed far enough from the operating frequency band around 3 GHz. The propagation constant β_{g} versus frequency is drawn in Figure 3.4. It is seen that, the cut-off frequency is at 2.3 GHz, and it is well below the frequency band between 2.9 and 3.3 GHz.

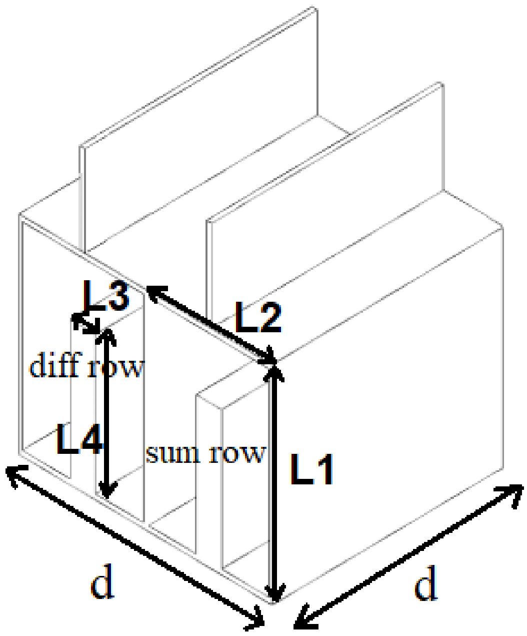

Figure 3.2: A closer view of the array structure

Table3.1: Ridged Waveguide Dimensions

Dimension	Ridged Waveguide (mm)	WR284 Waveguide (mm)
L1	35	34.036
L2	23	72.136
L3	4	-
L4	25	-
d	50	-

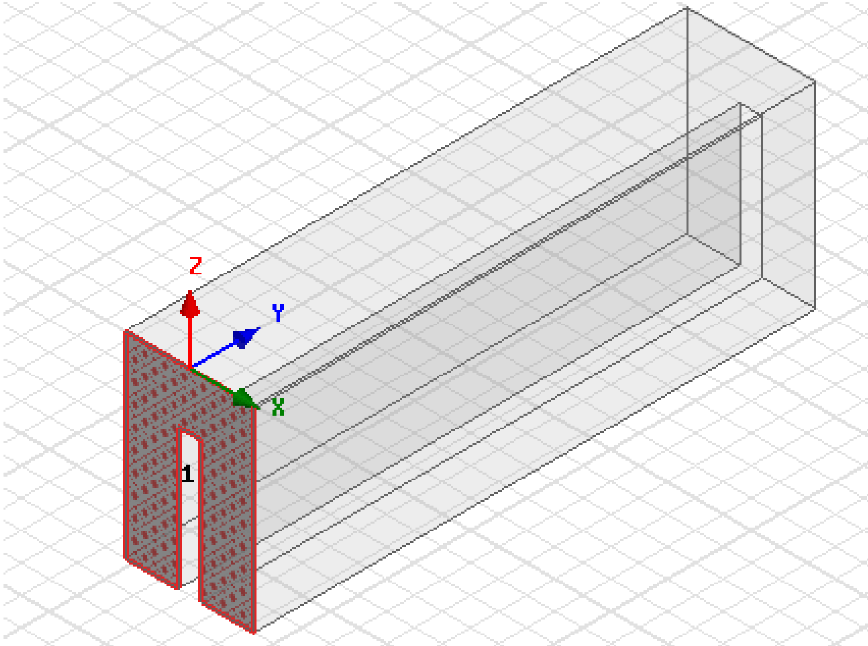

Figure 3.3: A ridged waveguide whose width fits in 0.18 guided wavelength λ_g

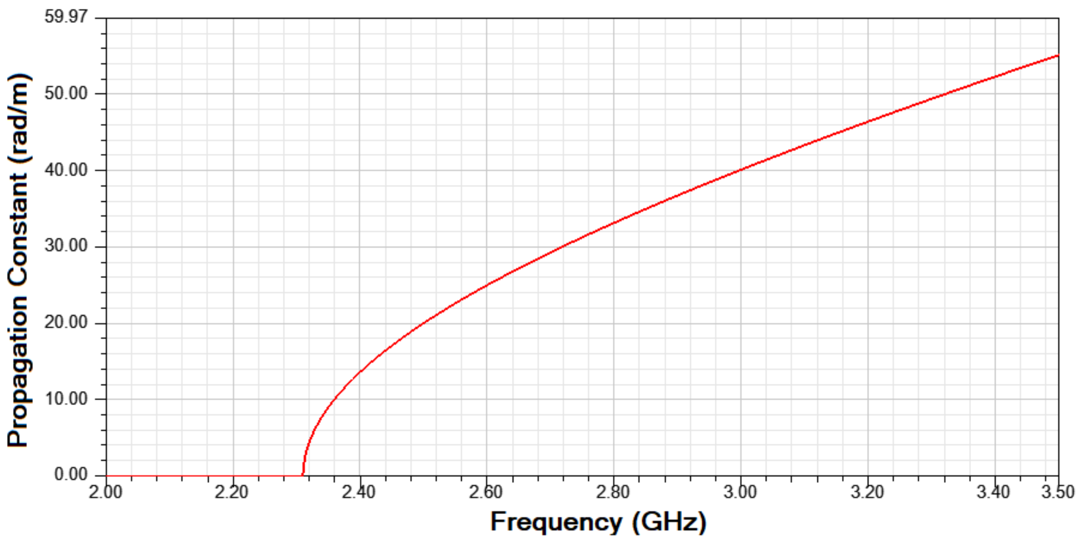

Figure 3.4: Propagation constant of the ridged waveguide

3.2 Placing a Probe on the Ridged Waveguide

In a terminated waveguide, when the load is mismatched, the voltage and current waves propagating towards the termination reflect back from the load. The amplitude of the reflection is related to the the ratio of mismatch. Due to this reflection, there occurs a backwards propagating wave. The combination of these two waves creates a standing wave. Measuring the standing wave pattern, the information about the load can be gathered. The measurement technique is called as voltage standing wave ratio (VSWR) measurement.

In VSWR measurements or slotted line measurements, a waveguide with a slit opened longitudinally at the center of the broad wall is used because the slots at the center on the wall do not radiate. This prevents inadvertent measurement error owing to a leakage. When a tiny probe penetrates the slit, it can sample the voltage pattern in the waveguide. The reason why the probe used is small is that the probe distorts the voltage because of the reflection from itself, and that the reflection and distortion get more deteriorating as the penetration increases. In fact, it behaves as a shunt admittance imposed to the transmission line, decreasing the impedance of the standing wave at the probe position [29]. The amount of decrease is directly related to the distortion.

In the structure proposed, a longitudinal rectangular slot is opened at the center of the broad wall. This is because these slots do not radiate and not allow butterfly lobes to exist in radiation patterns. Then, a probe is inserted into the slot, penetrating the waveguide as shown in Figure 3.5. This is similar to a broad wall adapter or the probe in VSWR measurement. The probe is, actually, a metal strip sandwiched into dielectric layers. The sum of the thicknesses of the dielectric layers and the width of the slot is kept the same to guarantee the position of the probe. Also, existence of dielectric layers provides that the probe is not shorted to waveguide wall. The probe strip turns into a rectangular coaxial connector in the broad wall, leaving a connection interface to the outside world. Thus, any radiating element can be connected to this port interface provided that the impedance of the port interface and the radiating element are matched.

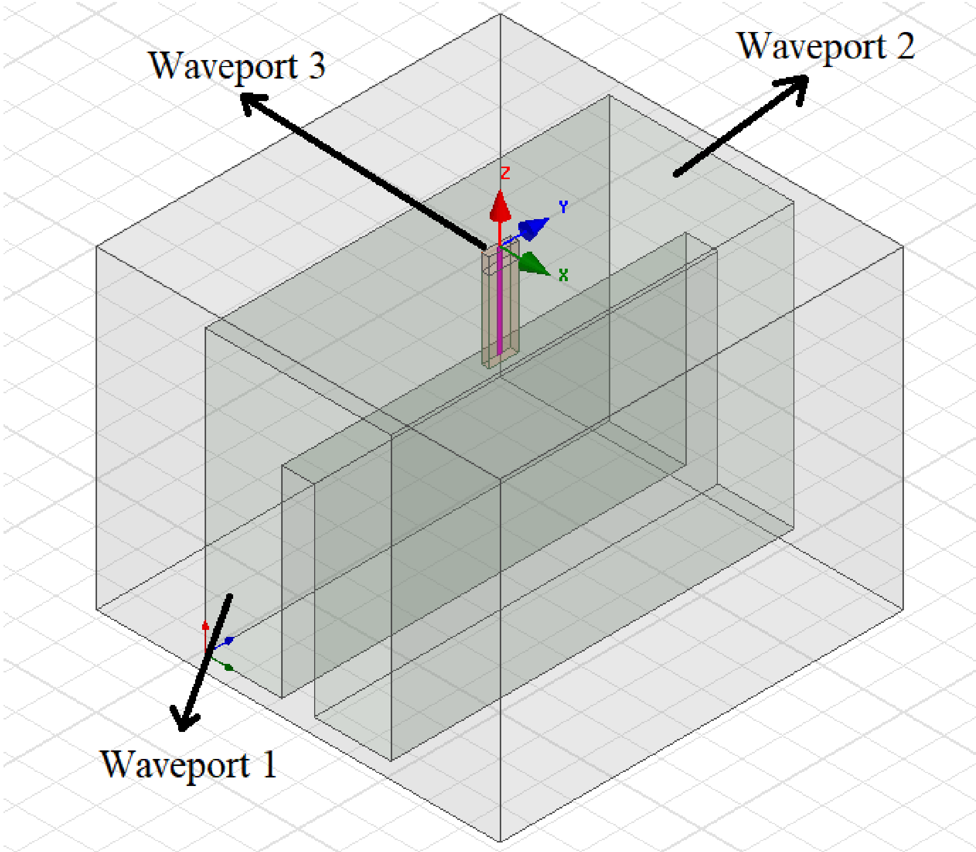

Figure 3.5: Probe structure

The above described structure is modelled in HFSS^{TM} as in Figure 3.5. Waveports are assigned to the input and output of the waveguide and to the rectangular coaxial port on the slot. Waveport 1 in Figure 3.5 is the input port, and Waveport 3 corresponds to the port which will be connected to the radiating element. The model is simulated for several probe lengths using a parameter sweep over an S-band frequency range. S_{11} which represents the reflected power from the probe is plotted in Figure 3.6 for several probe penetration lengths. Also, the power transmitted to the slot, S_{31}, is illustrated in Figure 3.7 for several probe lengths. The arrows in Figure 3.6 and Figure 3.7 show the direction of increase in the length of the probe (L_p), and L_p changes from 1.4 mm to 9.9 mm with 0.5 mm steps. Besides, when the probe gets thicker, the transferred power increases as well as the scattered one. The width of the probe is optimized to minimize the ratio of the returns loss, $|S_{11}|^2$, to the transferred power, $|S_{31}|^2$. Hence, a slot whose width and length are 1 mm and 3 mm, respectively, is opened on the broad wall. Then, a probe whose width is 0.9 mm is placed in that slot after being sandwiched between 0.5 mm Rogers 4003 substrates.

The simulations show that an increase in probe penetration results in an increase in the power transferred to the Waveport 3, as well as the reflection from it. However, S_{11} is below -10 dB. This is seen to be acceptable when these unit cells are cascaded to form an array. It is, also, seen that both $|S_{11}|^2$ and $|S_{31}|^2$ climb up with an increase in the probe length, so $|S_{21}|^2$ decreases. Nevertheless, it is acceptable as long as $|S_{11}|^2$ is smaller than $|S_{31}|^2$ when an array is formed.

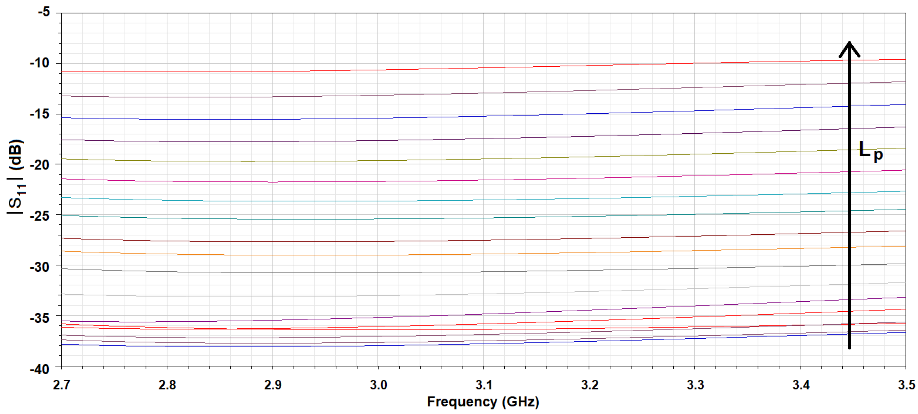

Figure 3.6: Reflected power from the slot for several probe lengths (Probe length increases in the arrow direction from 1.4 mm to 9.9 mm with 0.5 mm steps.)

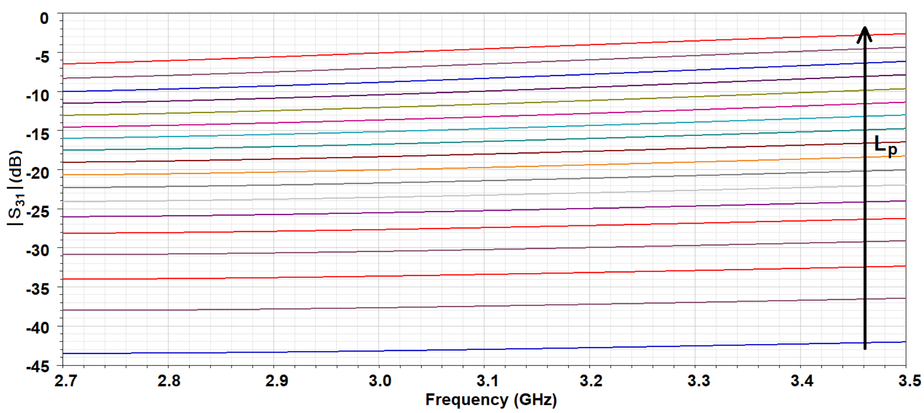

Figure 3.7: Transmitted power from the slot for several probe lengths (Probe length increases in the arrow direction from 1.4 mm to 9.9 mm with 0.5 mm steps.)

Hence, the amplitude of radiated power from the slot can be controlled by the probe length, i.e. adjusting probe length is a control mechanism to obtain desired amplitude taper in the array. Yet, the radiation phase is still an issue to be controlled. A method to control the phase is addressed in Section 3.4.1.

3.3 Placing a Radiating Element on the Slotted Waveguide

In this novel antenna structure proposed, a printed antenna can be used as a radiating element. This element may be Vivaldi, dipole or monopole etc. Since Gibson [30] first introduced Vivaldi antennas in 1979, they have been widely used in wideband applications. Then, Yngvesson et al. [31] compared different type of tapered slot antennas. One of them is linearly tapered slot antenna (LTSA). Its difference from Vivaldi is that its taper is linear instead of an exponential one.

In this design, the antenna element is shown as a stripline-fed LTSA like in [32]. It is chosen because it is a wideband antenna. Yet, another antenna satisfying the requirements can be used. The antenna is designed on Rogers 4003 substrate to operate in S-band around 3 GHz. The detailed explanation of the LTSA is given in Section 3.3.1.

The LTSA is fed via a stripline terminated with a fan like structure, which is used for wideband impedance matching. The reason why a stripline-fed type is chosen is to be consistent with geometry of the designed probe, which is connected to an LTSA. The stripline excites the antenna via a slot; in fact, fields on the feed line couples to the slot. The slot is terminated with a cavity in one end. The cavity is placed there for impedance matching. The other side of the slot flares to increase the frequency bandwidth. The aperture length of the end of the flare determines the lowest frequency of operation. To avoid the undesired parallel plate modes which may exist in the stripline LTSA, vias are placed around the feed line. The input impedance of the LTSA is nothing but the impedance of Port 3 shown in Figure 3.5. For a desirable performance, the LTSA is to be matched to the port on the probe penetrating the waveguide. That is, Z_{ant} should be equal to Z_{probe} as shown in Figure 3.8. Moreover, PEC walls are inserted between the consecutive LTSAs of a linear array as demonstrated in Figure 3.9. The reason for this is to prevent possibly existing parallel plate modes between the closely spaced antennas of the sum and difference arrays.

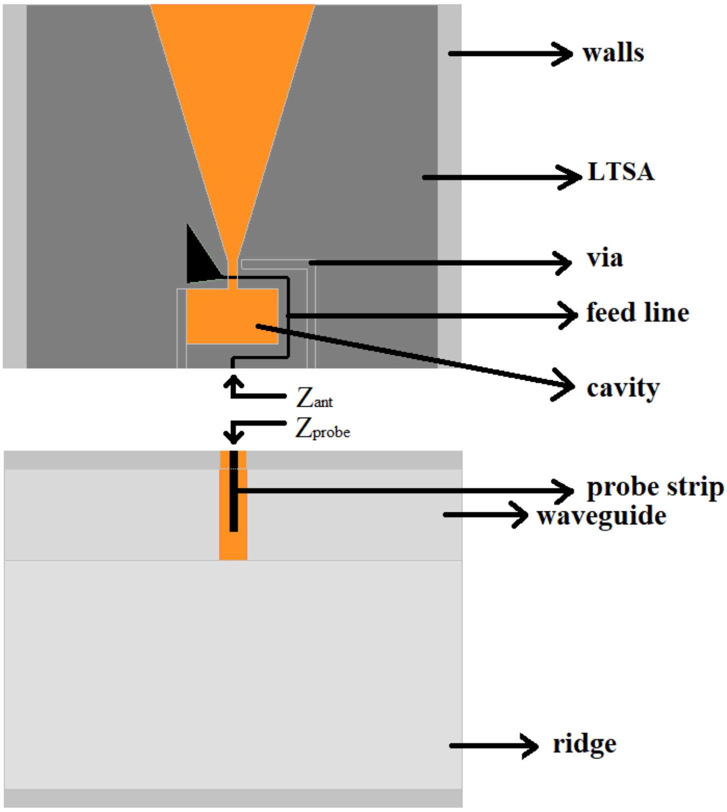

Figure 3.8: LTSA and waveguide with a probe

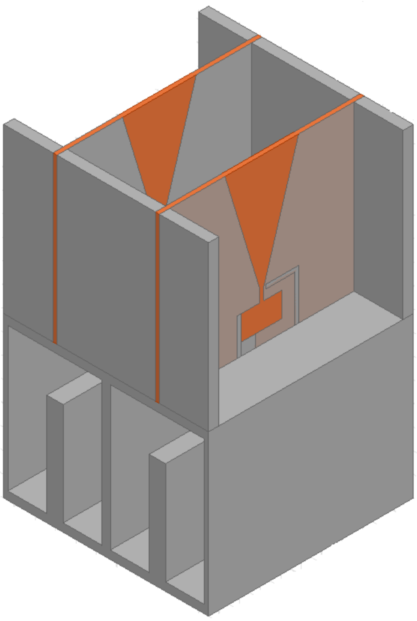

Figure 3.9: Two LTSAs placed side by side on waveguide for sum and difference rows

3.3.1 Linearly Tapered Slot Antenna

It is mentioned that different excitation coefficients can be obtained varying the probe lengths. It is required to minimize the return loss of each probe in order to decrease the couplings between the slots; otherwise, the array pattern degrades due to the constructive interference of the reflected signals. Hence, an antenna element is designed satisfying low reflection even for the case where array elements are closely spaced. The detailed view of the antenna is depicted in Figure 3.10. The LTSA is a stripline-fed type, and Rogers 4003 substrates with relative permittivity 3.38 and thickness 0.5 mm is used in the antenna. The antenna parameters shown in Figure 3.10 are optimized in HFSS^{TM} when there is another LTSA placed 0.25 λ_0 apart. The optimized parameters are shown in Table 3.2.

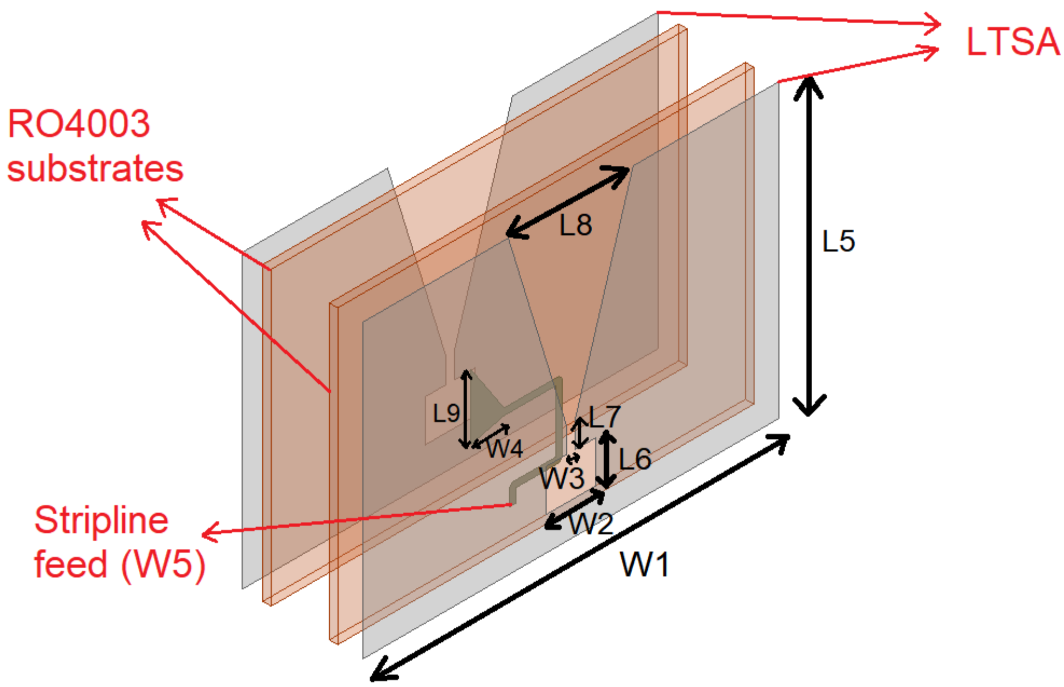

Figure 3.10: Detailed view of the LTSA

Table3.2: LTSA Dimensions

L5	35 mm	L6	6 mm	L7	3 mm	L8	15 mm	L9	7 mm
W1	50 mm	W2	10 mm	W3	1 mm	W4	4 mm	W5	0.3 mm

The unit cell shown in Figure 3.11 consists of two LTSAs and PEC walls to suppress parallel plate modes which may occur between conducting plates of closely spaced LTSAs. It is periodic in the two horizontal dimensions, and it is terminated via PML boundary in the vertical direction. The antennas are fed from a waveport at the lower end of the feed line whose dimensions are equal to the ones of the slot opened on the waveguide. With the optimized parameters that minimizes the scattered power, the return loss of the antenna is demonstrated in Figure 3.12.

It can be seen in Figure 3.12, LTSA has a return loss below -13 dB between 2.9 and 3.3 GHz. Therefore, the antenna can be used as a radiating element. Yet, even if the antenna is optimized as explained, it should be tuned when it is placed on the waveguide.

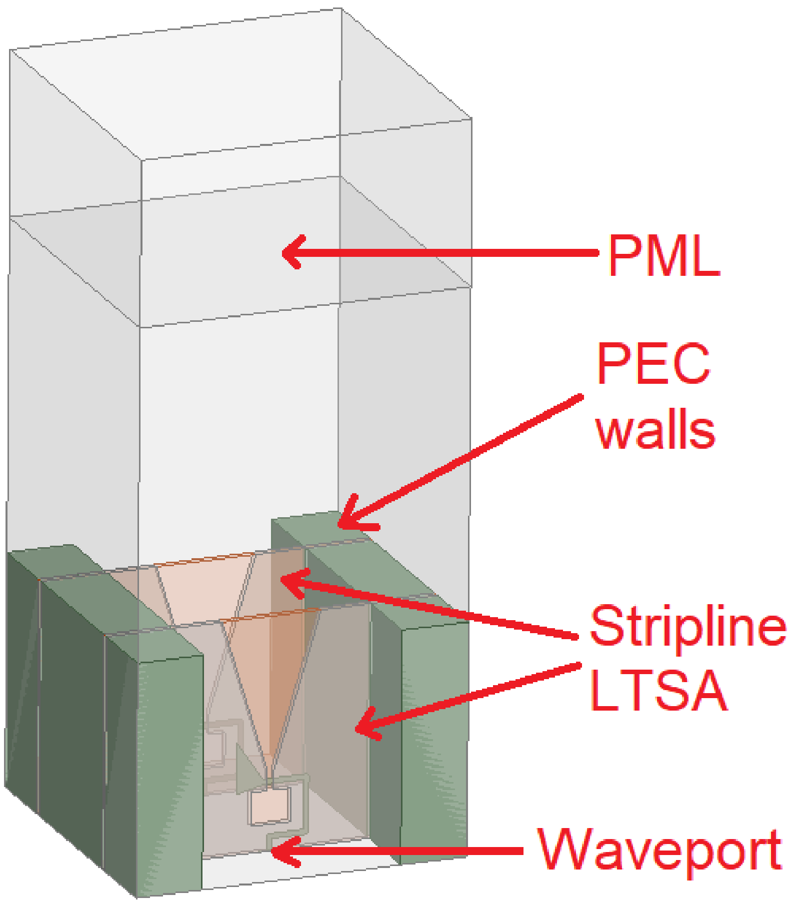

Figure 3.11: Unit cell view of the LTSAs

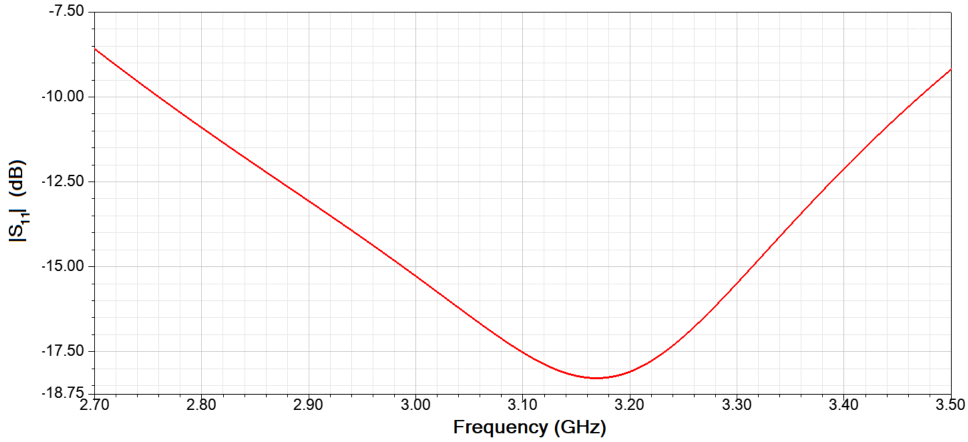

Figure 3.12: Return loss of the LTSAs

3.4 Characterization of the Hybrid Structure

3.4.1 Radiation Control Mechanisms

Control mechanisms on radiation amplitude and phase should be found to design an array by using the hybrid structure including two elements side by side for sum and difference arrays. That is, radiation amplitude and phase should be controlled independently varying some parameters. There are a lot of parameters affecting frequency bandwidth, reflection coefficient, and the magnitude and phase of radiated E-field. These are the length of the flared end, the height of the LTSA, the gap width of the LTSA, the dimensions of the cavity on the LTSA, the balun structure terminating the feed line, the width and length of the feed line, the width, length and height of the slot opened on the broad wall, the dimensions of the ridged waveguide, the thickness and height of the walls between successive LTSAs, the width and length of the probe, and the permittivity and thickness of the dielectric substrate.

It is mentioned in Section 3.2 that the reflection from each cascaded hybrid element may lead the radiation characteristics of the elements to deviate from the desired ones even when the radiation amplitudes and phases of them are controlled and adjusted. Furthermore, the coupling between adjacent elements may alter the desired excitations. Hence, first of all, the reflection coefficient and the coupling between adjacent elements should be minimized. When it is accomplished, the non-radiated power is almost transmitted to the next element, considering a travelling-wave array design. For this purpose, all the parameters except the length of the probe and feed line are swept, and an optimal solution is found minimizing the couplings and reflections.

It is also stated in Section 3.2 that when a probe is inserted into a waveguide from its broad wall, the length of it determines the power coupled to it. So, this is the control mechanism on the radiation amplitude. Nevertheless, the phase of radiated field is not stable, and changes with the length of the probe. Unless a control mechanism for the phase is found, creating an array by cascading the hybrid structures is non-sense. It is realized that there is no other parameter than the length of the feed line to simply control the radiation phase. Actually, increasing the length of the feed line imposes a phase shift. The varying phase with the change in the probe length can be compensated by an imposition of a specific phase shift. Thus, the radiation phases of the hybrid elements can be made equal to each other with a probe length and feed line length pair as depicted in Figure 3.13. The characterization to find the desired pairs is explained in Section 3.4.3.

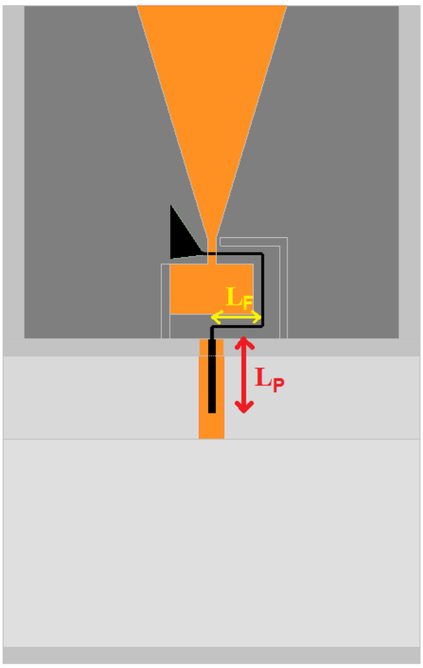

Figure 3.13: The parameters of control mechanism on radiation amplitude and phase: probe length, feed line length

3.4.2 Infinite Array Approach

In order to characterize the hybrid structure to determine its radiation amplitude and phase, it is modelled in HFSS^{TM} using infinite array approach. The approach models the structure as if there are infinitely many identical elements in both direction, and their excitations differ only by a phase shift. In infinite array analysis, edge effects due to the finiteness of the array are ignored. The structure is in a box whose width and length are the element spacings of the planar array in the two dimensions. The height of the box is determined according to the boundaries on the planes with the normal vector parallel to the third dimension. This box is called a "unit cell" since any of the elements in an infinite array can be treated equivalently. When boundary conditions are applied and ports are assigned to the unit cell, the solution represents the behavior of the element in the infinite array.

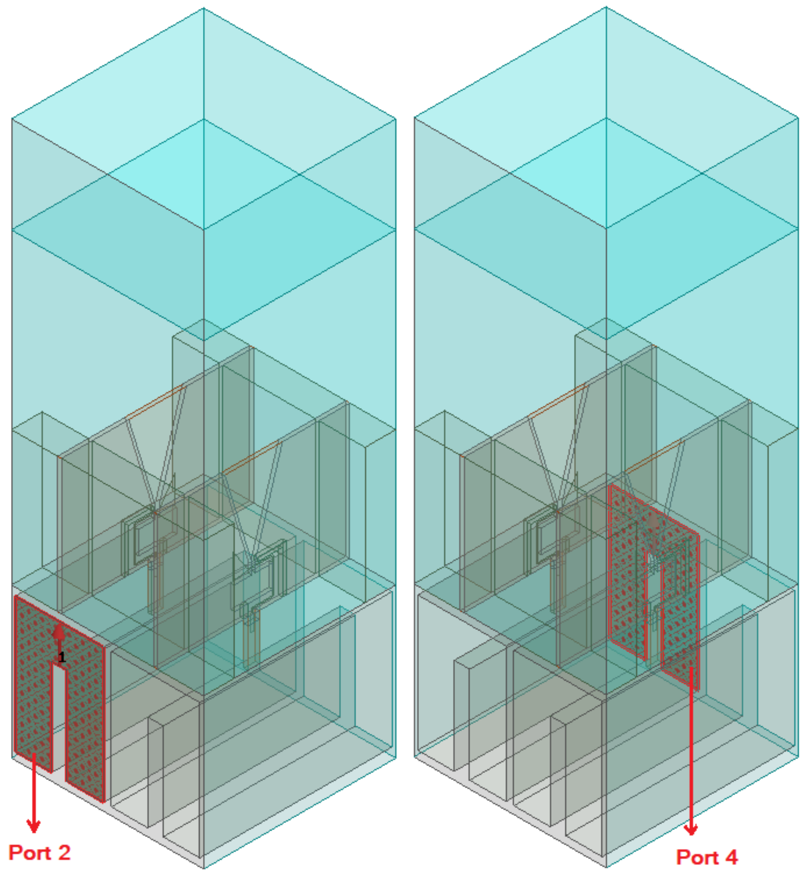

Figure 3.14: Waveport assignments to the waveguide ports of sum array

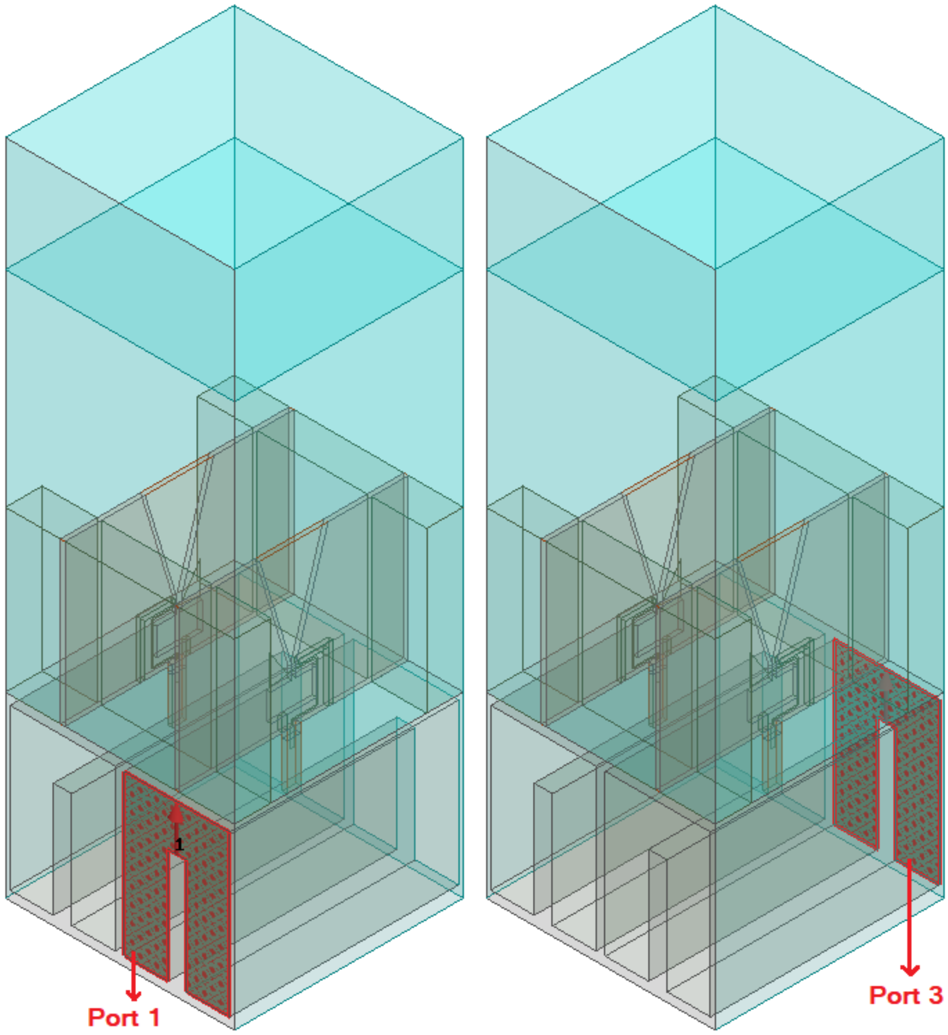

Figure 3.15: Waveport assignments to the waveguide ports of difference array

Waveports are assigned to the external boundaries of waveguides as illustrated in Figure 3.14 and Figure 3.15. A modal solution is performed by finding the eigenvalues of the boundary value problem on waveports. Using the propagation constants and patterns of the modes, and exciting the port with these patterns, generalized scattering parameters are calculated. There is an important point in this calculation that any higher-order mode is to be suppressed for an accurate result; otherwise, the calculated parameters are misleading [14].

The boundaries of the unit cell are handled with the use of master and slave boundaries in HFSS^{TM} as demonstrated in Figure 3.16. This provides periodicity in an infinite array. The field distribution in the master boundary is tried to match the one in the slave boundary in simulation. Yet, a progressive phase shift can be imposed on these boundaries. The phase difference is determined according to the scan or squint angle.

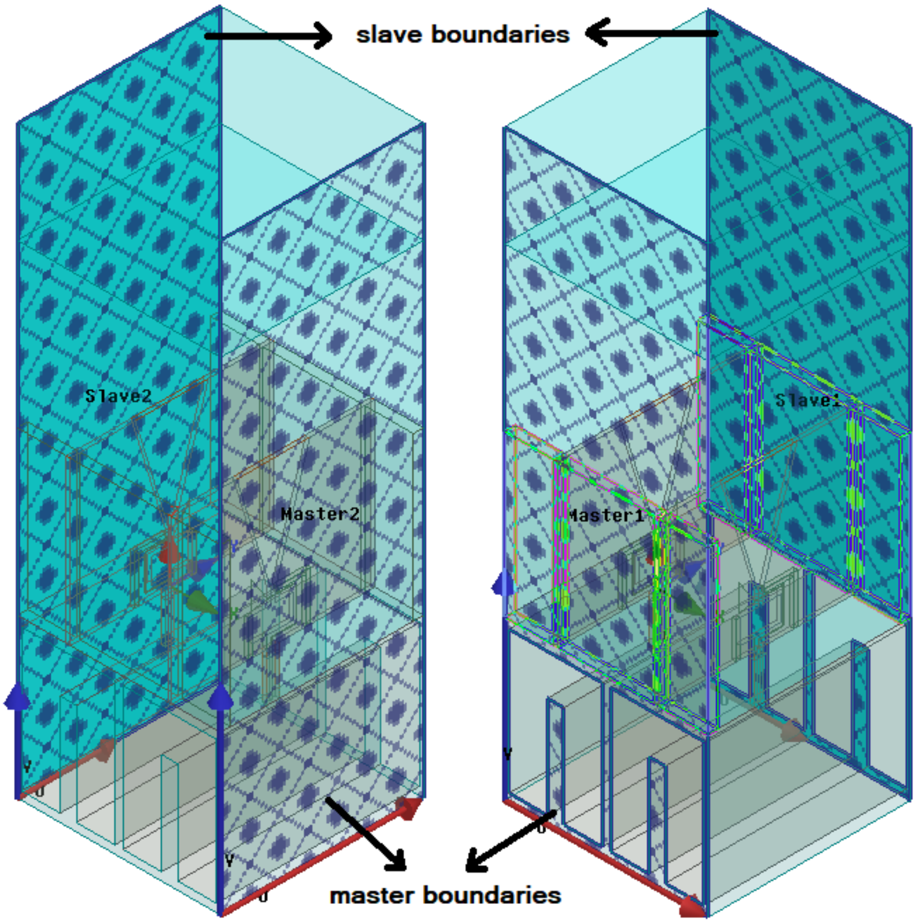

Figure 3.16: Master and slave boundaries assigned to unit cell

Since it is a travelling wave array, a phase shift is imposed on the master and slave boundaries in the longitudinal direction of the waveguide. In the transverse direction, the phase shift is zero, and it is a broadside array. The phase shift is calculated by:

$$shift = \beta_g \times d - \pi \tag{3.1}$$

where d is the element spacing in the longitudinal direction, and β_g is the propagation constant of the waveguide.

Moreover, a perfectly matched boundary (PML) is assigned to the the upper face as shown in Figure 3.17. It is a virtual representation of an anisotropic material which completely absorbs the incident electromagnetic fields. So, there will be no reflection from the upper face.

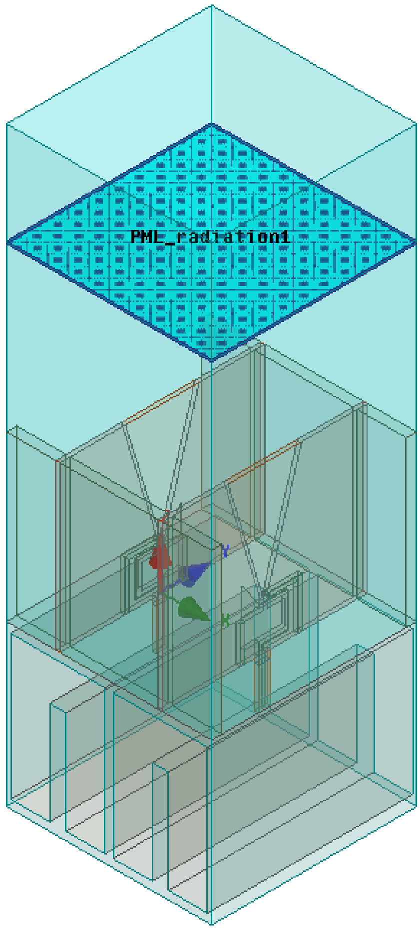

Figure 3.17: Absorbing boundary condition (PML) on the upper face

Instead of PML boundary, Floquet port can be used since the array is periodic in both directions. It resembles a waveport, and works based on modal decomposition. Even if it is more suitable to the modelling process which is mentioned in Chapter 4, it is not used because it does not allow the phase shift to depend on an intrinsic variable, such as frequency. However, a frequency sweep is needed for characterization, and the phase delay changes with frequency. Thus, PML boundary is used instead of Floquet port.

3.4.3 Determination of Radiation Characteristics

When the radiation control mechanisms are found, all other parameters affecting the radiation from the unit cell are fixed provided that the return loss is minimized. So, the parameters that can only be swept are the lengths of the probe and the feed line as they are shown in Figure 3.18. The impact of control parameters on the radiation

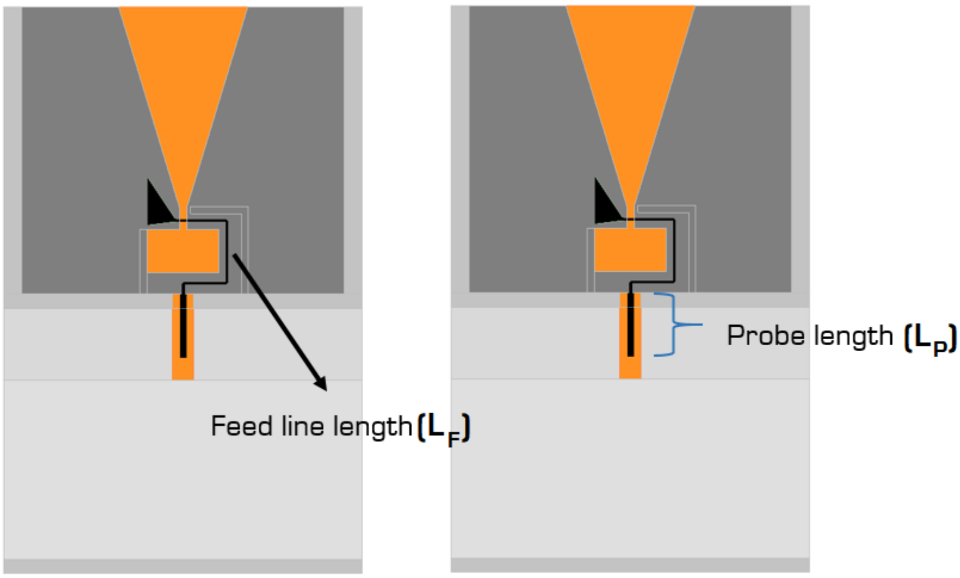

Figure 3.18: Radiation control parameters

is examined in HFSS^{TM} using the unit cell described in Section 3.4.2. To do so, the length of the feed line is fixed, and the probe length is swept. This operation is repeated for several lengths of the feed line. Of course, the step resolution of the fixed variable is determined considering the error caused by the interpolation which will be performed later to make the data continuous for an accurate design solution. The same procedure is applied to sweep the length of the feed line when the probe length is fixed to several values. In fact, the sweep is performed on 2D data points whose axes are the feed line length and the probe length.

For a fixed length of the feed line, the probe length is swept for the magnitude of radiated power over frequency. The magnitude of radiated power is calculated exciting an input port by an incident field with 1W power. By doing so, radiated powers are normalized. The radiated power can be calculated by subtracting the transferred powers to the other waveports and the return loss of the input port 1 from the incident power.

$$P_{radiation} = 1 - \sum_{n=1}^{4} |S_{n1}|^2 \tag{3.2}$$

Since the model is symmetric, for any input port, the calculated radiated powers are equal. The frequency response of this sweep is seen to be extremely flat as depicted in Figure 3.19. It can be inferred from the Figure 3.19 that the design can operate in a wide frequency band when compared to a slotted waveguide array.

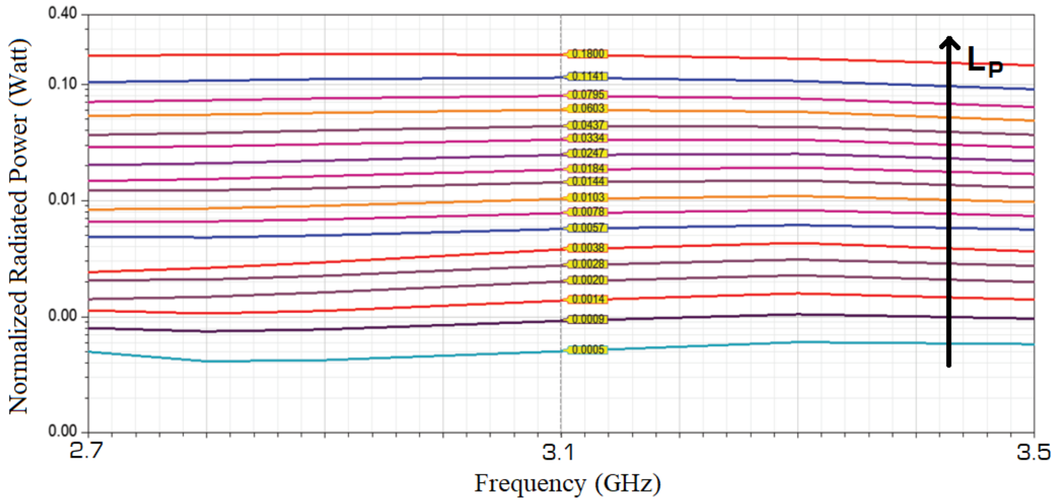

Figure 3.19: Extremely flat frequency response of the unit cell for a fixed length of the feed line (6.5 mm) for a swept probe length (1.4 mm to 9.9 mm with 0.5 mm steps, where the arrow indicates the direction of increase

Nonetheless, the radiated power slightly decreases for a fixed probe length when the feed line lengthens as illustrated in Figure 3.20. This is because the stripline between the conducting plates of LTSA is covered by vias on one side to suppress any parallel plate modes between these plates, which may cause undesired radiation. Since the distance between the vias and the sripline is fixed, these vias moves with the length of the feed line. Hence, this affects the radiation amplitude. Yet, this can be compensated if the desired design parameters are chosen using the 2D interpolated data.

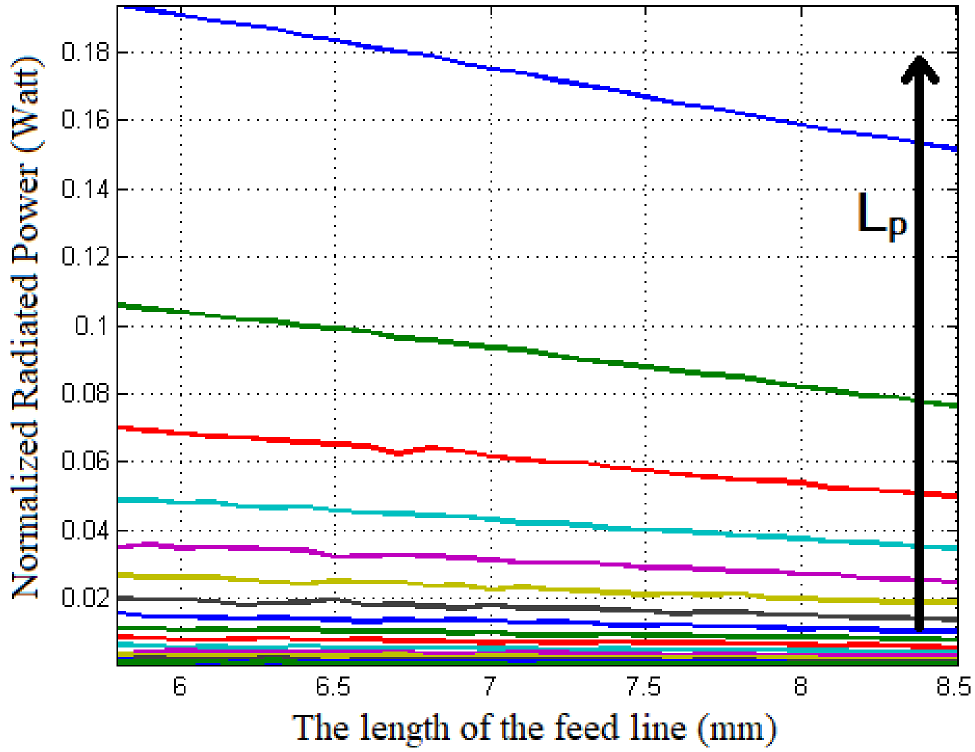

Figure 3.20: Radiated power for several fixed probe lengths (1.4 mm to 9.9 mm with 0.5 mm steps, where the arrow indicates the direction of increase) when the feed line lengthens

Therefore, Figure 3.19 and Figure 3.20 show that different excitation levels can be obtained by selecting a proper probe length.

However, it can be seen in Figure 3.21 that different excitation levels lead to the phase of the radiated E-field to be different, and that the phase response is monotonically decreasing, which needs compensation. Otherwise, the random phase error on the aperture distribution degrades the desired radiation pattern, and leads to an increase in the side lobe levels. For the sake of completeness, the radiated E-field is defined as:

$$\vec{E}(r,\theta,\phi) = \frac{e^{-j\vec{k}.\vec{r}}}{r}\vec{F}(\theta,\phi) \tag{3.3}$$

The far-field pattern is the plot of magnitude of F(θ,ϕ) with respect to θ and ϕ. The argument of F is defined as the phase of the radiated field:

$$\theta_{\text{rad field}} = arg(F_\theta(\theta,\phi)) \tag{3.4}$$

The reason why it is the θ component instead of the ϕ one is because the unit cell is modelled in Section 3.4.2 in a way that the array lies on y-axis, whose boresight is in z-axis as it can be seen in Figure 3.17.

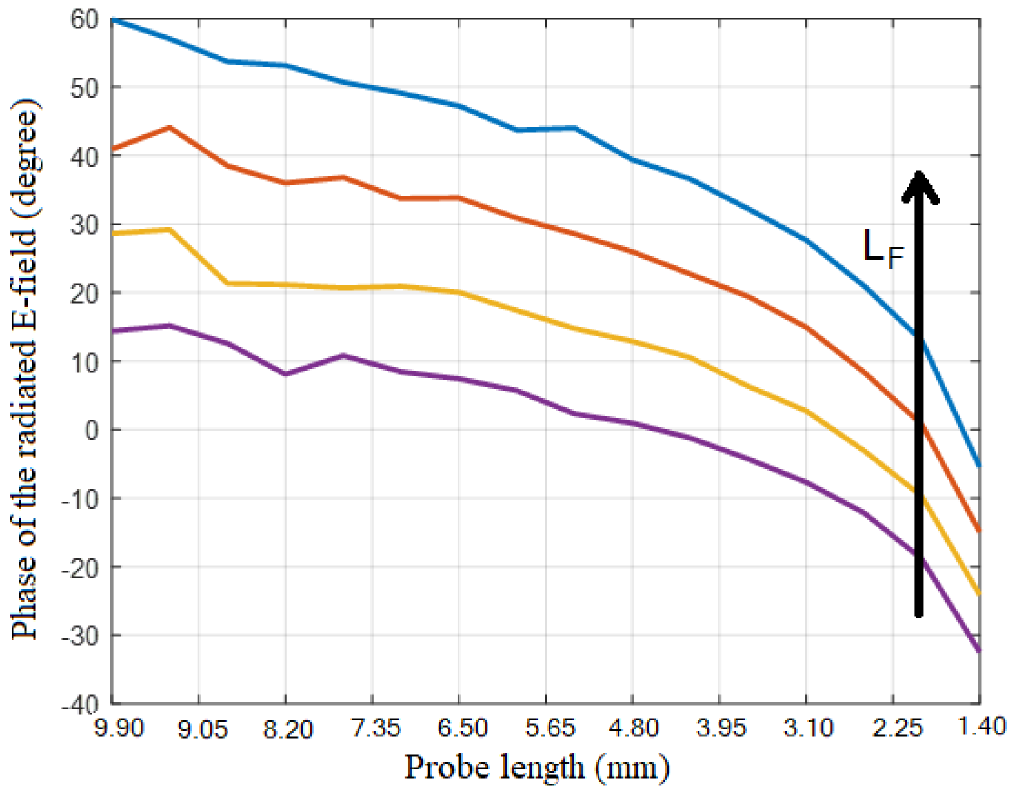

Figure 3.21: Phase response of different excitation levels for a fixed sample feed line length L_F(5.5 mm to 8.5 mm, with 1 mm steps in the direction of the arrow)

Similarly, for a fixed probe length, the length of the feed line is swept. The variation in the phase of radiated E-field is observed with respect to the change in the length of the feed line as demonstrated in Figure 3.22. It is seen that the relation between the phase of radiated E-field and the length of the feed line is almost linear. So, it can be inferred from Figure 3.22 that varying the length of the feed line, any phase shift can be given to compensate the undesired phase variation due to the change in the probe length for different excitation levels.

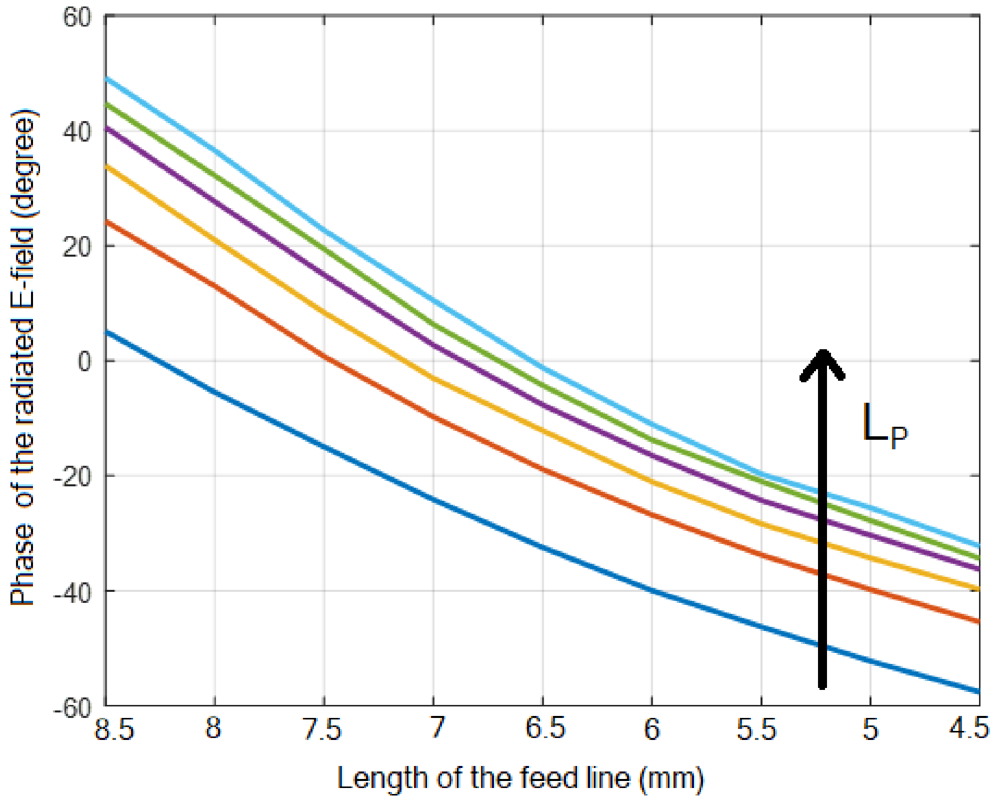

Figure 3.22: Phase shift vs. the length of the feed line for several fixed probe lengths (5 mm to 10 mm, with 1 mm steps in the direction of the arrow)

Thus, since not only the relation between the phase of radiated E-field and the length of the feed line is nearly linear, but also the one between the probe length and the phase of the radiated E-field is monotonically decreasing/increasing, the deviation of the far field phase due to different excitation levels can be taken under control by using both parameters. Thus, the phases of all the elements in the array can be made equal.

All in all, the parameter sweep on both the length of the feed line and the probe length provides an agility to find an appropriate parameter set for the array to have a desired amplitude distribution on the aperture with a small phase error among the elements of the array.

Finally, it is known that there are two parameters controlling the phase of the radiated E-field and the amplitude of the radiated power. The relation between the controlled mechanisms and the parameters are not linear, and the mechanisms are actually functions of both parameters. So, a parameter sweep is performed varying both radiation control parameters. The values of these functions, namely the phase of the radiated E-field and the amplitude of the radiated power, for a parameter pair are illustrated in Figure 3.23 and Figure 3.24, respectively. Using the data given in Figure 3.23 and Figure 3.24, an efficient way of creating an array with a desired aperture field distribution is explained in Chapter 4.

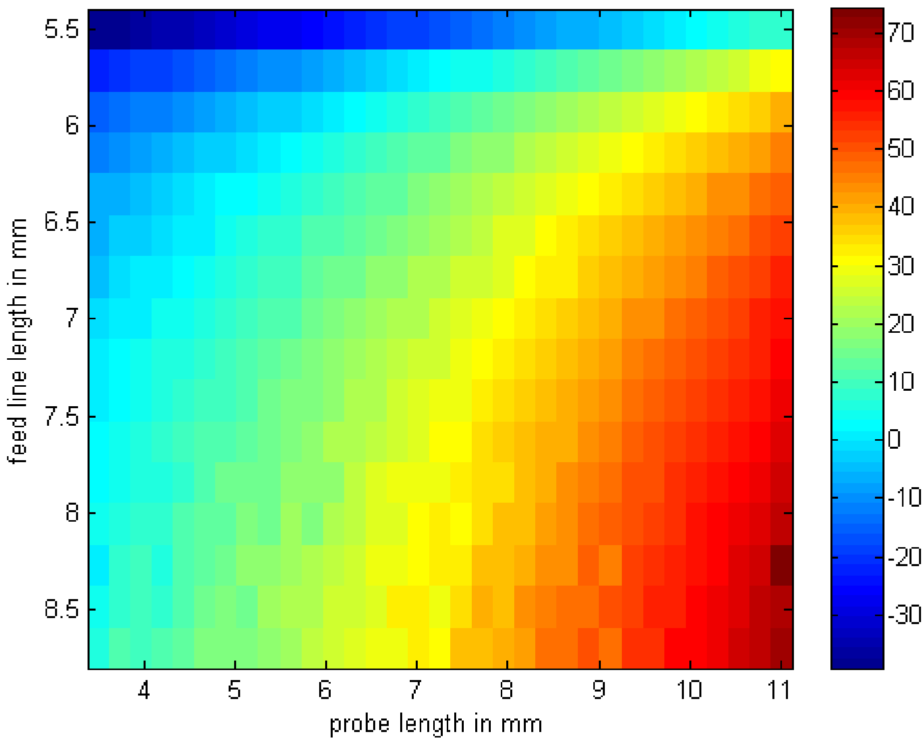

Figure 3.23: Phase of the radiated E-field versus control parameters

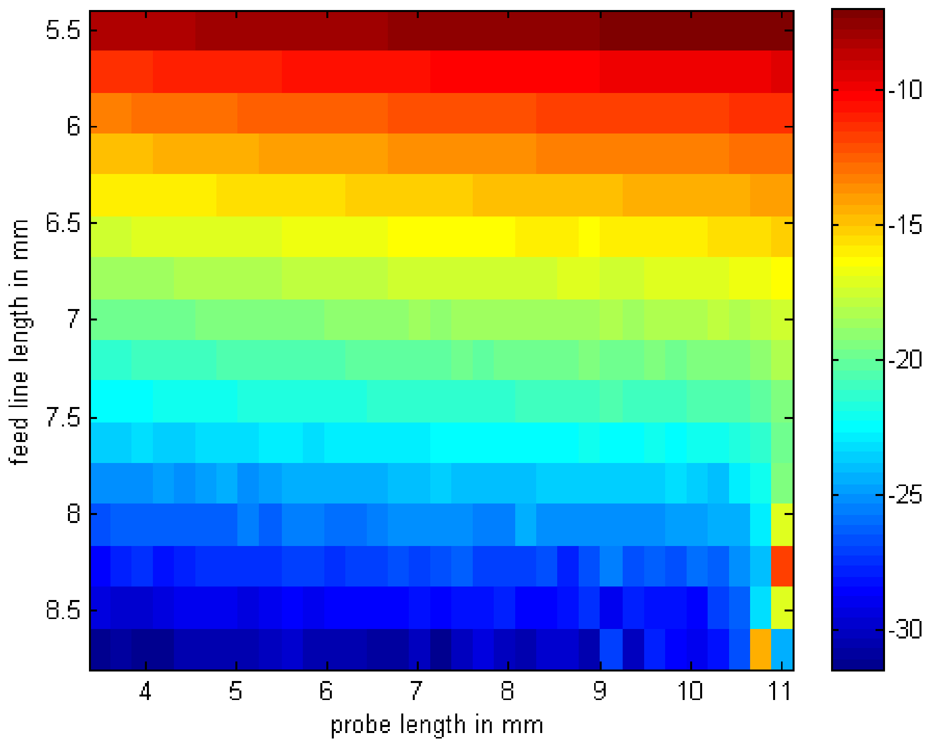

Figure 3.24: Radiated power versus control parameters

CHAPTER 4

MATHEMATICAL MODELLING OF SLOTTED WAVEGUIDE-BASED PRINTED ANTENNA ARRAY

In this chapter, a method to design the array is proposed. Firstly, the reason why the conventional travelling-wave array design method is not preferred is stated in Section 4.1. Then, how the unit cells characterized in Chapter 3 is described as 5-port networks is explained in Section 4.2. Next, the linear monopulse array design approach is given in Section 4.3. Finally, the mathematical model of the used design method is verified with simulations in Section 4.4.

4.1 Determination of the Design Method

The array is first designed using the conventional travelling-wave array design method as explained by Elliott in [8]. This method determines the conductances of the shunt slots iteratively. However, it does not handle the coupling between the adjacent sum and difference elements because it is not included in the initial assumptions of the method. So, a new method including the mentioned couplings is proposed and verified.

When the array is designed calculating conductances iteratively, it is seen that there occurs a severe jump in the middle in the near field amplitude distribution of the array as shown in Figure 4.1. This is because the phase reversal mechanism is intentionally missed in the middle of difference rows to have a Taylor-like difference distribution, whereas it is applied for every successive element in sum rows. By not giving an extra π radians phase shift in the middle of difference rows as shown in Figure 4.2, the phases of the elements on either side of difference rows from the middle become opposite. However, this is unpredicted and not modelled in conventional method.

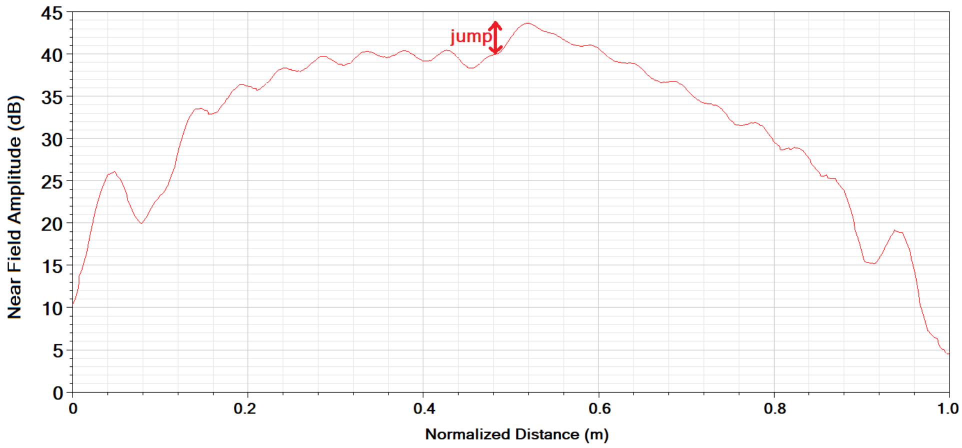

Figure 4.1: Near-field amplitude distribution of the array designed with conventional method. The array length is scaled to 1 m, and the near-field is measured at a distance $\lambda/2$ from the array.

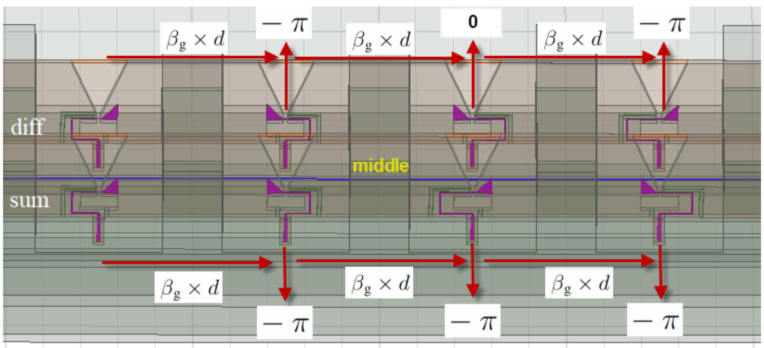

Figure 4.2: Phase reversal mechanisms in the middle of the sum and difference arrays

When the proposed method is used, the jump seen in Figure 4.1 does not appear as it can be seen in Figure 4.3. This is because the model explained in Section 4.2 and Section 4.3 handles the coupling between sum and difference rows.

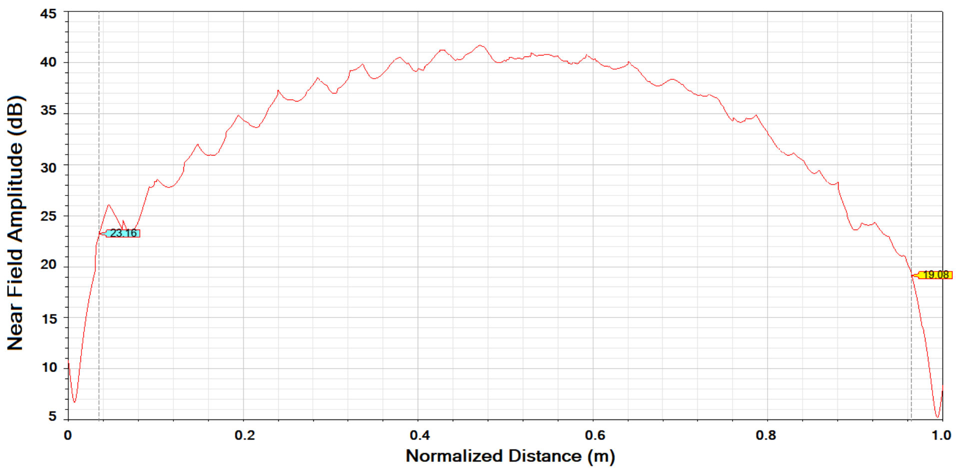

Figure 4.3: Near-field amplitude distribution of the array designed with proposed method. The array length is scaled to 1 m, and the near-field is measured at a distance $\lambda/2$ from the array.

4.2 Network Representation of the Unit Cells

In Chapter 3, modelling of unit cell is explained. Radiation control parameters are also discussed. After sweeping the length of the probe and the feed line to obtain different excitation levels with a constant phase of the array elements, 4-port scattering parameters are exported from HFSS^{TM}. The reason why the exported S-matrices are in the form of 4x4 matrices is as explained before that there is a PML boundary behaving as an absorber instead of a waveport. The field infringe upon this boundary is only be seen in the exported S-matrices as the unit cell becomes lossy due to the absorbing boundary; that is, the energy is not conserved. In fact, the energy is conserved when the field upon the PML boundary is taken into consideration.

The extracted 4-port S-matrices represent the inter-relation of the waveports at the input and the output of the sum and difference elements placed side by side as depicted in Figure 4.4. Here, the field on the PML boundary should be added to the network by adding a new port (port 5) representing the radiated field. While doing so, the fact that there is no reflection from the PML boundary is taken into consideration since it is an absorbing boundary condition. Since the energy within the unit cell is conserved, the magnitude of the radiated E-field ($|S_{5n}|$) can be calculated easily using the scattering parameters representing the transferred power from the input waveport to the other waveports when the incident power on the input port is 1 Watt. The phase of the radiated E-field ($\theta_{\text{rad field}}$) calculated with the use of far field setup in HFSS$^{\text{TM}}$ is taken as the phase of S_{5n} as in:

$$S_{5\text{n}} = \sqrt{1 - |S_{1\text{n}}|^2 - |S_{2\text{n}}|^2 - |S_{3\text{n}}|^2 - |S_{4\text{n}}|^2} \times \theta_{\text{rad field}} \tag{4.1}$$

where n is the waveport number indicated in Figure 4.4.

The self parameters of the 5$^{\text{th}}$ port can be taken as zero as well as the power transmitted from the 5$^{\text{th}}$ port to the waveports for simplicity. Since only the radiated E-field determining the far field pattern is considered in the design approach, it can be assumed that there is no return loss at this port if there exists an incident wave from far-field to the port. In other words, the scattered portion of an incident wave coming from far field does not affect the solution as it is off the scope. Besides, using a PML boundary, it is made sure that there is no field reflected from it. So, the insertion losses S_{n5} can be taken as zero to be convenient.

$$S_{55} = 0 \tag{4.2}$$

$$S_{\text{n}5} = 0, \qquad for\ n{=}1, 2, 3, 4 \tag{4.3}$$

where n is the corresponding waveport number, which is 1, 2, 3 or 4 as shown in Figure 4.4.

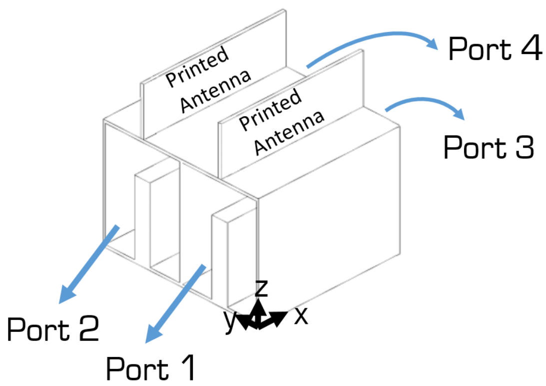

Figure 4.4: Waveports represented by the exported 4-port network

With these assumptions and calculations, any unit cell with a specified probe and feed line length pair is modelled as a 5-port network including inter-element couplings between sum and difference rows.

4.3 Cascading the Unit Cells Using Their Scattering Parameters

To obtain an efficient selection procedure for the appropriate design parameters, the scattering parameters of the unit cell are extracted from HFSS^{TM}. Since the design of full array takes a lot of time in HFSS^{TM}, the extracted and enlarged S-matrices according to the desired amplitude and phase distribution are cascaded after the unit cells with appropriate radiation control parameters for the array to have desired aperture distributions are selected using a gradient-based search algorithm in MATLAB^{TM}.

Cascading networks using their ABCD parameters is possible and needs no extra calculation, but the networks strictly have 2 ports. In this case, the ones to be cascaded have 5 ports, so S-parameters are used. Yet, this requires derivation.

The configuration of the cascaded networks can be seen in Figure 4.5, and the port definitions shown are used in derivation. Port 3 and 4 of the network I are connected to the port 1 and 2 of the network II, respectively.

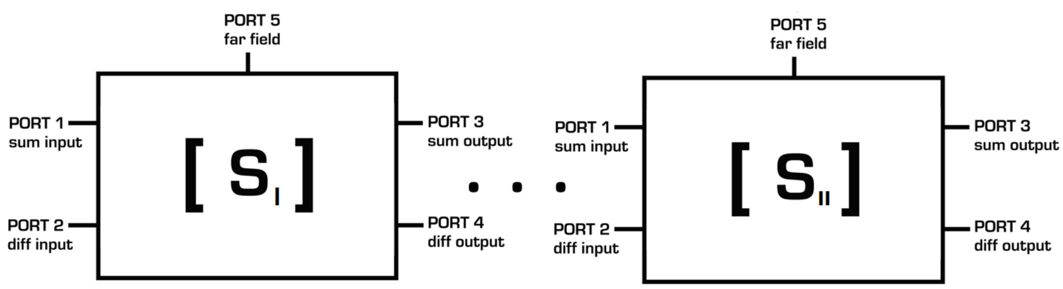

Figure 4.5: Configuration of the cascade operation

For this configuration, a connectivity matrix C is written. This matrix relates the power waves incident upon and scattered from the internal ports. For instance, Scattered power wave from the port 3 and 4 of the network I is the incident power wave to the port 1 and 2 of the network II, vice versa.

$$[b_{\text{internal}}] = [C][a_{\text{internal}}] \tag{4.4}$$

If it is written explicitly, it becomes:

$$\begin{pmatrix} b_{\text{I3}} \\ b_{\text{I4}} \\ b_{\text{II1}} \\ b_{\text{II2}} \end{pmatrix} = \begin{pmatrix} 0 & 0 & 1 & 0 \\ 0 & 0 & 0 & 1 \\ 1 & 0 & 0 & 0 \\ 0 & 1 & 0 & 0 \end{pmatrix} \begin{pmatrix} a_{\text{I3}} \\ a_{\text{I4}} \\ a_{\text{II1}} \\ a_{\text{II2}} \end{pmatrix} \tag{4.5}$$

After creating the connectivity matrix, overall S-parameters should be written into a matrix of 10x10 by separating the internal and external ports.

$$\begin{pmatrix} b_{\text{external}} \\ b_{\text{internal}} \end{pmatrix} = \begin{pmatrix} S_{\text{A}} & S_{\text{B}} \\ S_{\text{C}} & S_{\text{D}} \end{pmatrix} \begin{pmatrix} a_{\text{external}} \\ a_{\text{internal}} \end{pmatrix} \tag{4.6}$$

Here, external ports are port 1 and 2 of the network I, and port 3 and 4 of the network II. Similarly, internal ports are port 3 and 4 of the network I, and port 1 and 2 of the network II.

In order to perform algebraic operations, Equation 4.6 is partitioned to separate external and internal ports.

$$[b_{\text{external}}] = [S_{\text{A}}][a_{\text{external}}] + [S_{\text{B}}][a_{\text{internal}}] \tag{4.7}$$

$$[b_{\text{internal}}] = [S_{\text{C}}][a_{\text{external}}] + [S_{\text{D}}][a_{\text{internal}}] \tag{4.8}$$

When the connectivity matrix is substituted into Equation 4.8, it becomes:

$$[C][a_{\text{internal}}] = [S_{\text{C}}][a_{\text{external}}] + [S_{\text{D}}][a_{\text{internal}}] \tag{4.9}$$

Now, the internal incident power waves relate to the external ones.

$$[a_{\text{internal}}] = ([C] - [S_{\text{D}}])^{-1}[S_{\text{C}}][a_{\text{external}}] \tag{4.10}$$

Substituting Equation 4.10 into Equation 4.7, a relation between external incident and scattered power waves can be found. Actually, the relation is the equivalent scattering parameters of the combined network.

$$[b_{\text{external}}] = [S_{\text{A}}][a_{\text{external}}] + [S_{\text{B}}]([C] - [S_{\text{D}}])^{-1}[S_{\text{C}}][a_{\text{external}}] \tag{4.11}$$

$$[b_{\text{external}}] = ([S_{\text{A}}] + [S_{\text{B}}]([C] - [S_{\text{D}}])^{-1}[S_{\text{C}}])[a_{\text{external}}] \tag{4.12}$$

The new scattering parameters of the combined network are obtained as:

$$[S_{\text{combined}}] = [S_{\text{A}}] + [S_{\text{B}}]([C] - [S_{\text{D}}])^{-1}[S_{\text{C}}] \tag{4.13}$$

Now, it is known how networks with any number of ports can be cascaded by using their scattering parameters without being limited by the number of ports required for ABCD matrix. Hence, the derivations are to be used recursively so as to obtain the overall scattering parameters of an array with desired size and aperture field distribution in the next section. A similar method for cascade operation is described in [33].

4.4 Linear Monopulse Array Design

Deriving the scattering parameters of a combination of multi-port networks from the extracted S-matrices of the unit cell for several combinations of radiation control parameters, and using a gradient-based search algorithm, a fast and accurate design task is developed. This array design code is implemented in MATLAB™.

In order to reduce the data size and complexity, all the dimensions of the sum and difference elements in the same unit cell are taken equal, but the excitation direction may change by switching the direction of the feed line. If Bayliss distribution is used for difference array, the parameters of radiation control mechanisms of adjacent sum and difference antennas in the same unit cell will be different. Whereas N parameter sweeps are performed when the parameters of them are the same, N^2 of them should be done in Bayliss case as these adjacent elements affect each other's radiation characteristics. So as not to increase the order of complexity, a Taylor-like difference distribution is chosen for the difference array as Taylor one is applied to the sum array. In fact, a Taylor-like difference distribution is a Taylor one with a sign change beyond its bilateral symmetry plane. The aperture distributions are shown in Figure 4.6.

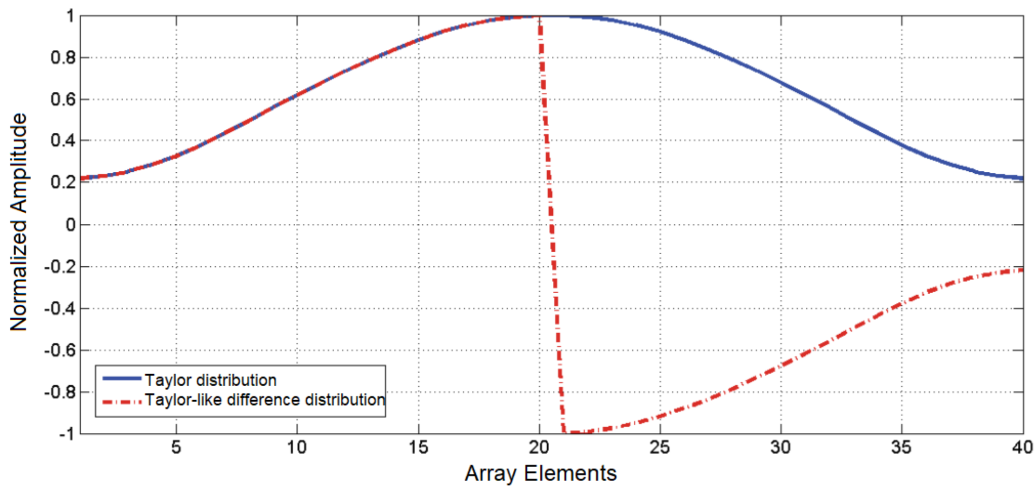

Figure 4.6: Taylor and Taylor-like difference aperture distributions

To give the mentioned aperture distributions, a gradient based search algorithm is written in MATLAB^{TM}. The algorithm needs an initial parameter set. The initial parameter set is determined choosing a curve from Figure 3.23 and Figure 3.24. The points on this curve provide the ideal amplitude distribution with nearly constant phase. By doing so, it is desired to shorten the time elapsed until the code is converged. It cascades 5-port unit cell networks with the control parameters in the set to design an N-element array with N+4 ports, 4 of which are input/output ports, and N of which are far field ports. Then, it calculates the amplitude and phase distribution over the array aperture, namely N far field ports. Determining the error between the required and realized amplitude distributions on N far field ports, it applies small perturbations to the initial set in contrast to calculated residuals to minimize the norm of residuals in the next step. It does recursively until the norm is minimized. With the minimum norm, the desired patterns are realized.

The pace of the algorithm depends on the size of the perturbations. However, the size is a trade-off that affects the final minimum norm. So, larger perturbations are used to speed up the progress since the norm is quite high for the initial set. Then, the size is made smaller as the norm of residuals gets below a pre-determined level, which is set to 2 in this design, so as not to compromise the accuracy of the results.

4.5 Verification of the Mathematical Model

In order to verify the used mathematical model, a 30-element array with 25 dB Taylor and Taylor-like difference distributions is designed in MATLAB™ by using the algorithm explained. The resultant radiation pattern is synthesized by computing the array factor with transmitted powers to 30 far field ports from the sum and difference input ports. Then, the same array is modelled and simulated in HFSS™. Then, the radiation patterns of the sum and difference arrays are compared as illustrated in Figure 4.7 and Figure 4.8, respectively.

It is seen that there is an excellent agreement between the compared patterns. Yet, note that the difference at the far-out angles results from the edge effects in the finite array environment in HFSS™.

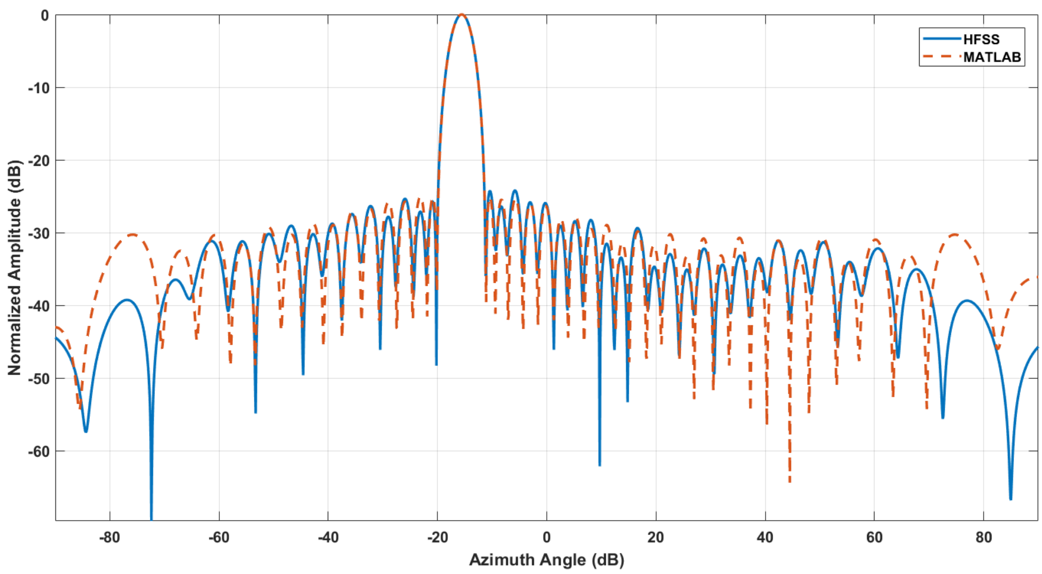

Figure 4.7: Comparison of the sum patterns: HFSS™ vs. MATLAB™ code

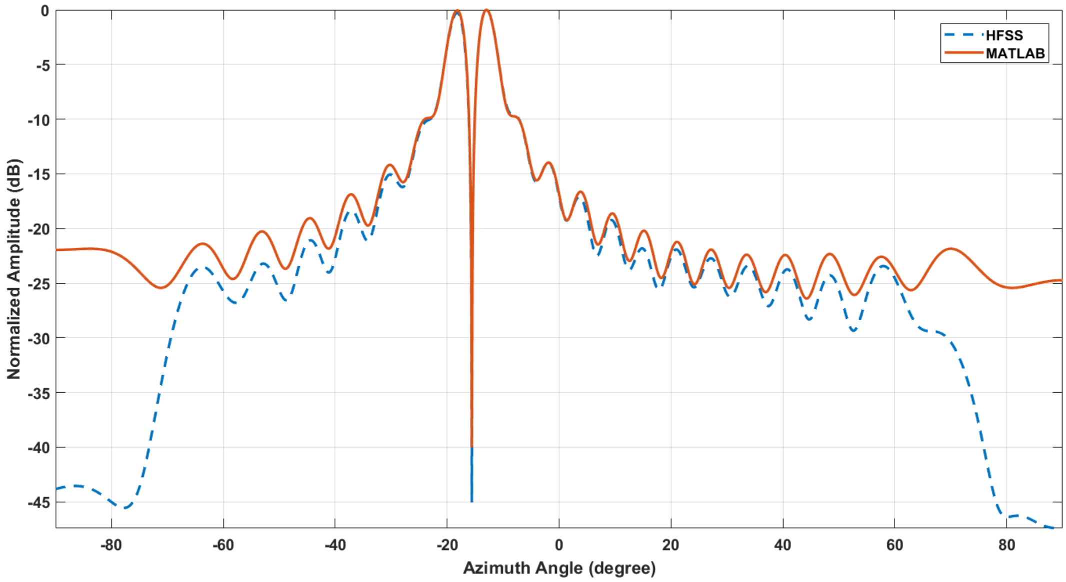

Figure 4.8: Comparison of the difference patterns: HFSS^{TM} vs MATLAB^{TM} code

Thus, the mathematical model derived gives pretty accurate results, and it can be used to quicken the design process.

CHAPTER 5

SIMULATION RESULTS OF MONOPULSE ARRAY

In this chapter, an array is designed using the method proposed in Chapter 4. Radiation patterns of the sum and difference arrays are given in Section 5.1 in the operating band. Moreover, a method to improve side lobe level is introduced and observed on radiation patterns in Section 5.2.

5.1 Radiation Patterns of Simulations

A 30-element prototype array is designed by cascading the unit cells including one sum and one difference element using the method developed in Chapter 4. The array has Taylor amplitude distribution providing 25 dB side lobe level for sum array. The same amplitude distribution is adapted to the difference array by using a Taylor-like difference distribution mentioned previously. The inter-element spacing d is chosen as 0.36 guided wavelength (λ_g) at 3.1 GHz, and it corresponds to half wavelength (0.5 λ_0) at 3 GHz. Since it is a travelling-wave array, d should be away from a half guided wavelength. Also, in terms of the free-space wavelength, it is chosen to avoid grating lobes.

The sum and difference patterns of it at the center, upper, and lower frequencies of the operating frequency band are depicted in Figure 5.2, Figure 5.3, and Figure 5.4, respectively. For the sake of completeness, the orientation of the array is given in Figure 5.1 for the notation in the radiation patterns to be clear.

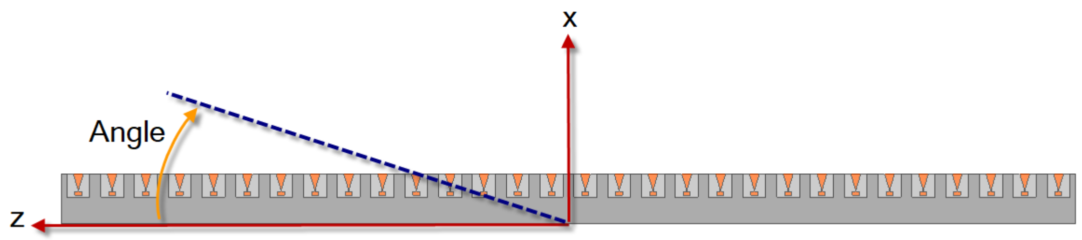

Figure 5.1: Orientation of the array

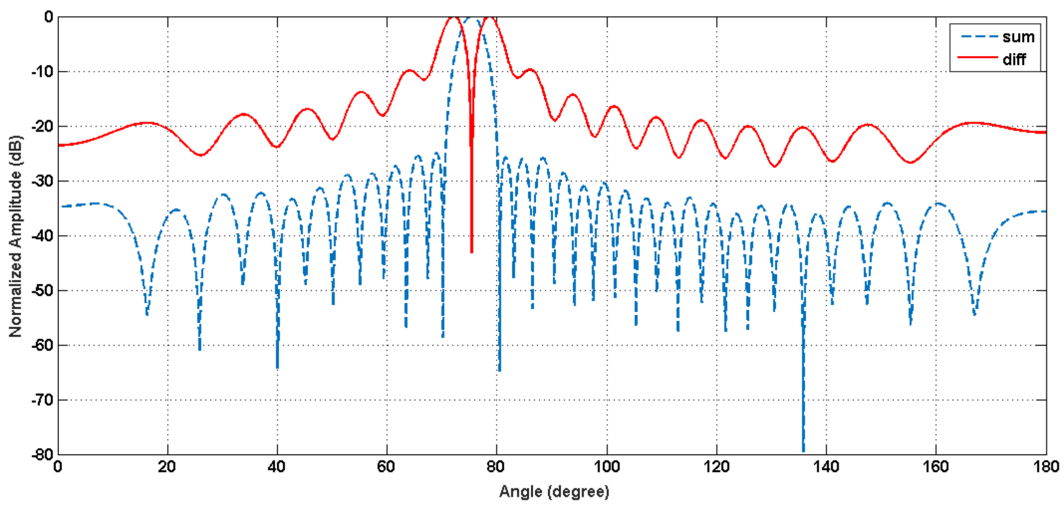

Figure 5.2: Sum and difference patterns @3.1 GHz

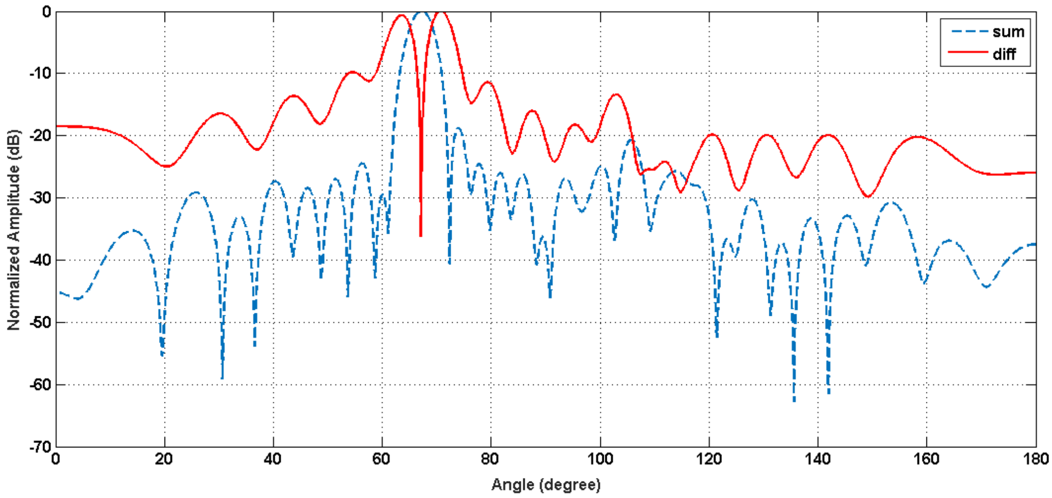

Figure 5.3: Sum and difference patterns @2.9 GHz

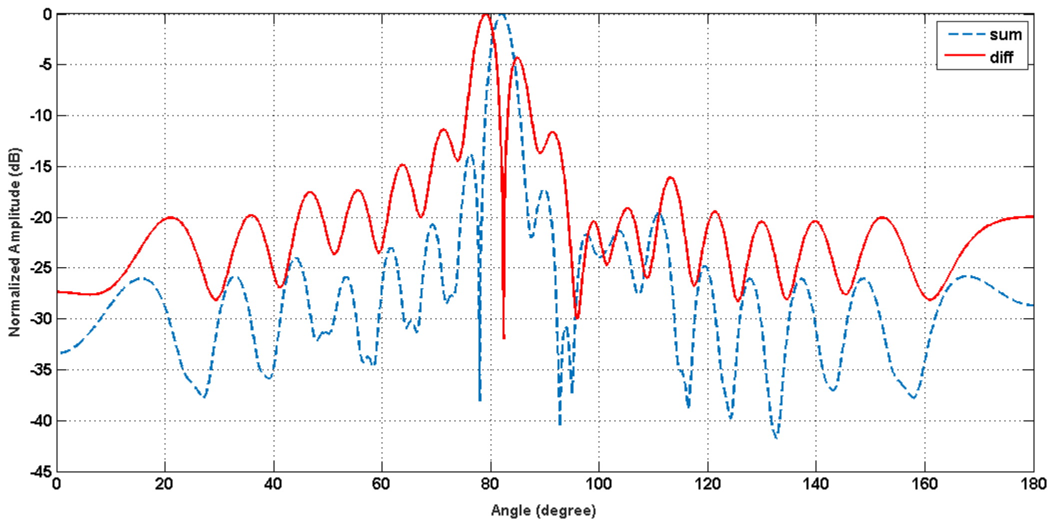

Figure 5.4: Sum and difference patterns @3.3 GHz

It can be seen that the side lobe distribution starts to deteriorate when the operating frequency deviates from the center frequency. This arises from the coupling between the closely-spaced (d/2) sum and different rows. For instance, the power coupled from the sum array to difference array leads to forward and backward propagating waves in the difference waveguide row. The backward travelling wave re-radiates from the difference array, and adds up to the radiation pattern of the sum array. This gives rise to a deterioration in the desired sum pattern, depending on the coupling level. Indeed, if the array includes only sum rows placed with a spacing of d/2, the coupling do not effect the radiation pattern. The radiation patterns of this sum array are given in Figure 5.5. In other words, even if it there is coupling between sum rows, the radiation patterns do not deteriorate as all the rows and their radiation patterns are identical.

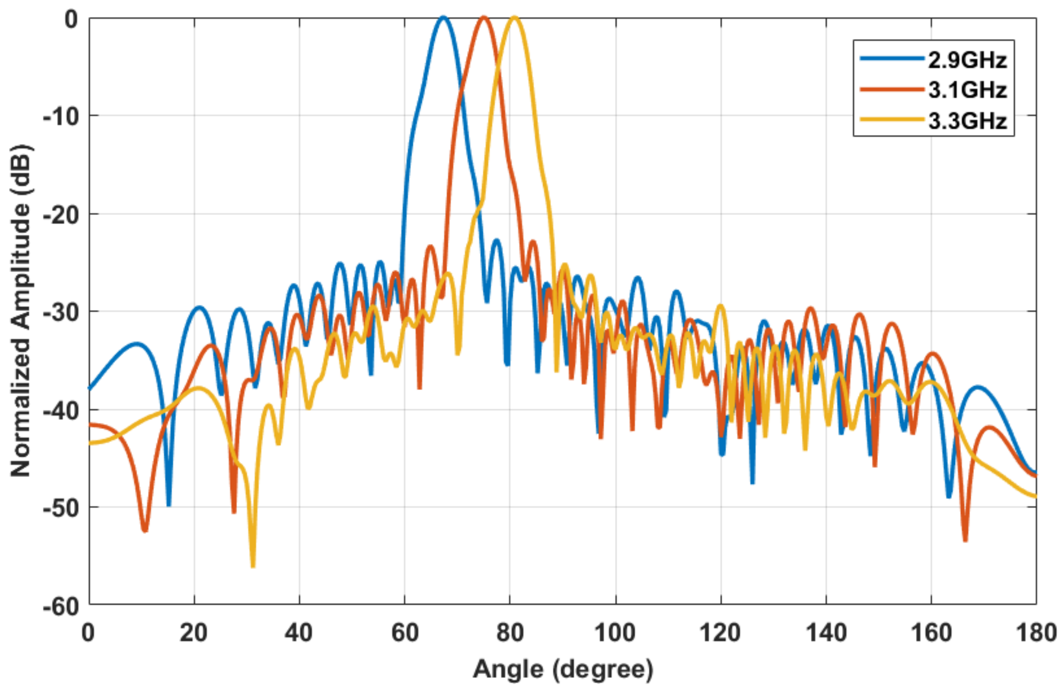

Figure 5.5: Radiation patterns of the array consisting of only sum rows at various frequencies

In fact, the effect of coupling on radiation patterns can be inferred from the steep change of the phase of the radiated E-field over frequency as shown in Figure 5.6 for several excitation levels. The phase changes 70 degrees from the low to high end of the operating frequency band. Besides, the coupling between the adjacent rows is changing over frequency band as demonstrated in Figure 5.7 for several excitation levels. This leads to an undesired ripple in amplitude distribution on the aperture. So, there is an increase in SLL on the patterns for the frequencies other than the design one.

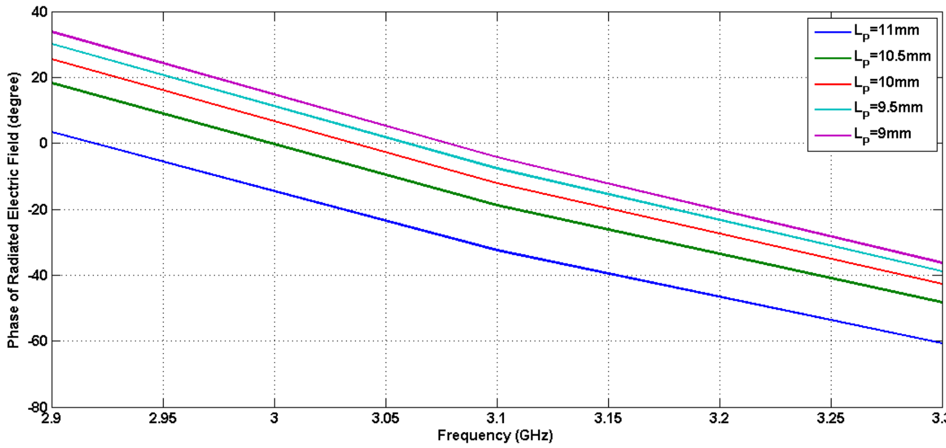

Figure 5.6: Phase of the radiated E-field vs. frequency for several probe lengths

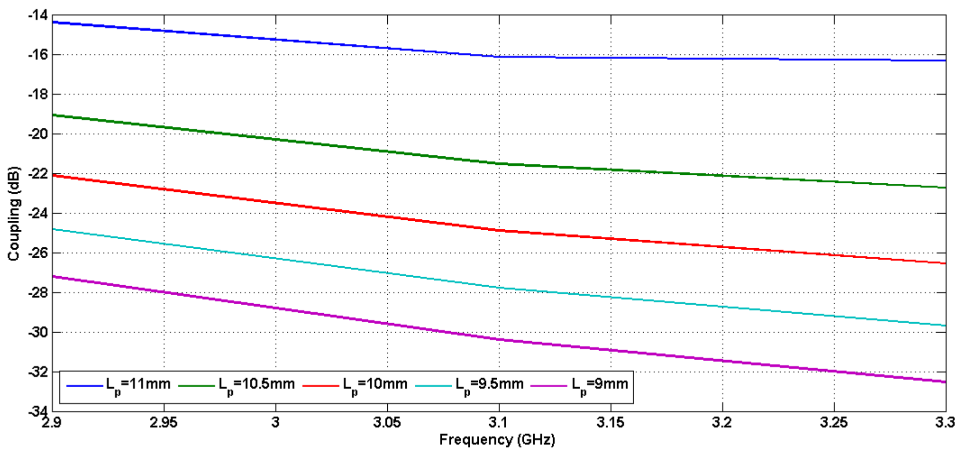

Figure 5.7: Coupling between sum and difference elements in the unit cell vs. frequency for several probe lengths

The array at the center frequency handles the coupling as it is designed at that frequency. However, the impact of the coupling on side lobes starts to be more visible as the frequency deviates more from the design frequency. Besides, there occurs an asymmetry in the twin beam of the difference channel because of the same reason. This can be overcome by decreasing the coupling. This effect can also be eased by the method explained in the Section 5.2. The coupling may be decreased by changing the unit cell structure by using a different printed antenna or a modified feed mechanism. Furthermore, the proposed method based on cascading S-parameters of 5 port unit cells can be extended to design arrays with wider bandwidths.

5.2 Method for the Improvement of the Radiation Patterns

This section introduces a method to make the level of the asymmetric beams equal in the difference channel, and to alleviate the effect of the coupling between the interleaved sum and difference arrays on side lobes.

The radiation pattern of the sum array can be represented by an array factor of N elements whose excitation coefficients a_n are the power waves transmitted from the sum input to the far field ports, where the element spacing is d.

$$AF_{sum} = \sum_{n=0}^{N-1} a_n \times e^{jnk_0 dcos(\theta)} \tag{5.1}$$

Similarly, the radiation pattern of the difference array can be represented by an array factor of N elements whose excitation coefficients b_n are the power waves transmitted from the difference input to the far field ports, where the element spacing is d.

$$AF_{diff} = \sum_{n=0}^{N-1} b_n \times e^{jnk_0 dcos(\theta)} \tag{5.2}$$

Knowing the array patterns of sum and difference arrays individually, if a small portion of the sum/difference pattern is added to the difference/sum pattern, the patterns are seen to be improved. This idea originates from the coupling between the sum and difference rows. For instance, if there is a portion of difference pattern appears in sum pattern, adding difference pattern with the same magnitude but opposite phase to the sum pattern, it can be improved. That is, in order to obtain an improved sum/difference pattern, the difference/sum pattern multiplied by a complex constants m/p is added.

The modified sum and difference radiation patterns can be represented as:

$$AFmod_{sum} = AF_{sum} + m \times AF_{diff} \tag{5.3}$$

$$AFmod_{diff} = AF_{diff} + p \times AF_{sum} \tag{5.4}$$

To choose m and p, firstly, ideal normalized patterns are generated. Obtained sum and difference patterns are normalized. Then, all possible m and p complex constants are generated, whose magnitude and phase change from 0 to 1, and 0 to 2π , respectively. All possible modified patterns are obtained for these m and p values, and renormalized. It is known that the dot product of a normalized vector with its complex conjugate equals to 1. So, inner products of ideal pattern vectors and modified patterns are generated to obtain l^2 norms. The complex constant m and p providing the maximum among these l^2 norms calculated are found. This is because the modified patterns corresponding to these m and p constants provides the least distorted patterns.

The method is applied to the designed array; i.e., a 30-element array with 25 dB Taylor amplitude distribution designed around 3.1 GHz. Note that no compensation is needed at the center frequency, 3.1 GHz as depicted in Figure 5.2. However, the patterns at other frequencies are graded up when the improvement method is applied using the m and p values in Table 5.1.

Table5.1: Complex Constants for Pattern Improvement

Frequency (GHz)	m	p
2.9	0.547 $\angle$100°	0.591 $\angle$90°
3.0	0.282 $\angle$90°	0.298 $\angle$100°
3.2	0.141 $\angle$-100°	0.107 $\angle$-100°
3.3	0.387 $\angle$20°	0.316 $\angle$-100°

Individual and compensated patterns are illustrated for sum array in Figure 5.8, for difference array in Figure 5.9 at 2.9 GHz, for sum array in Figure 5.10, for difference array in Figure 5.11 at 3 GHz, for sum array in Figure 5.12, for difference array in Figure 5.13 at 3.2 GHz, for sum array in Figure 5.14, for difference array in Figure 5.15 at 3.3 GHz.

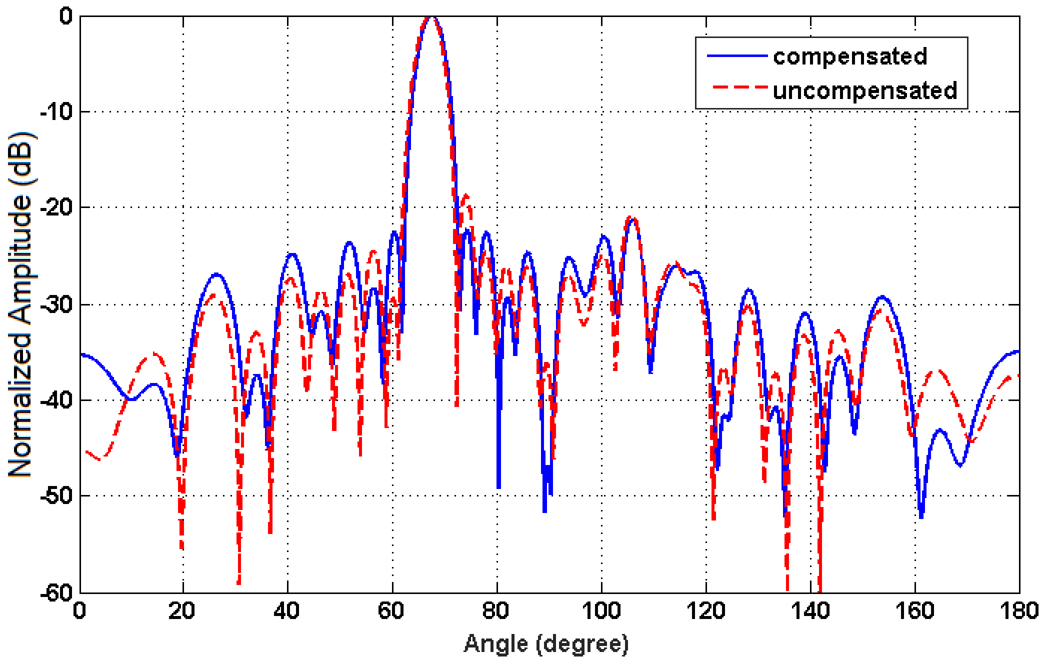

Figure 5.8: Normal and compensated sum patterns @2.9 GHz

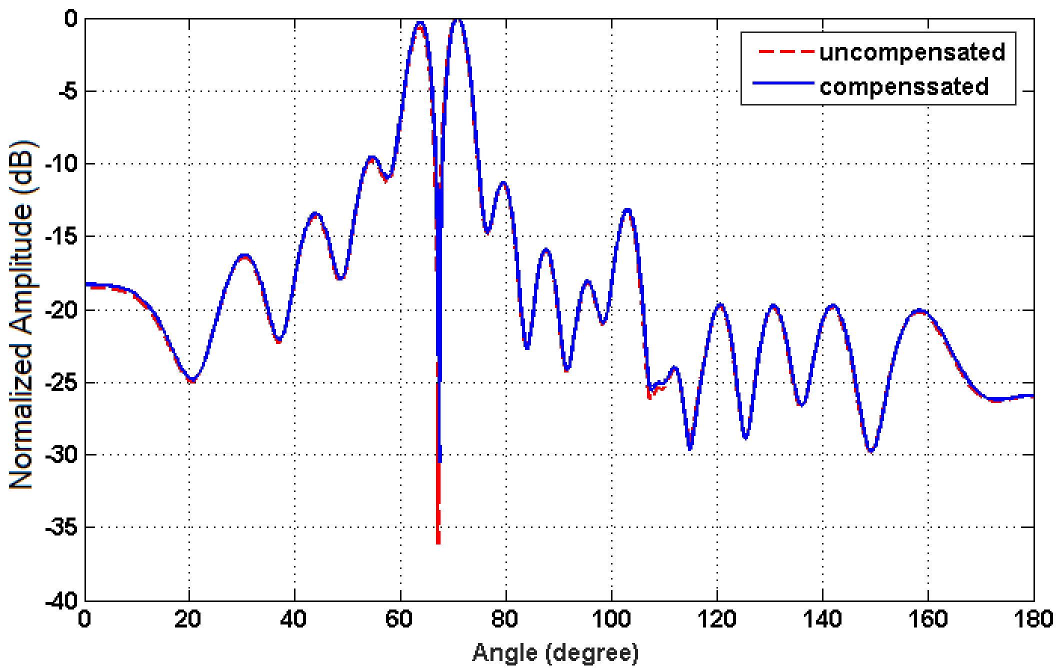

Figure 5.9: Normal and compensated difference patterns @2.9 GHz

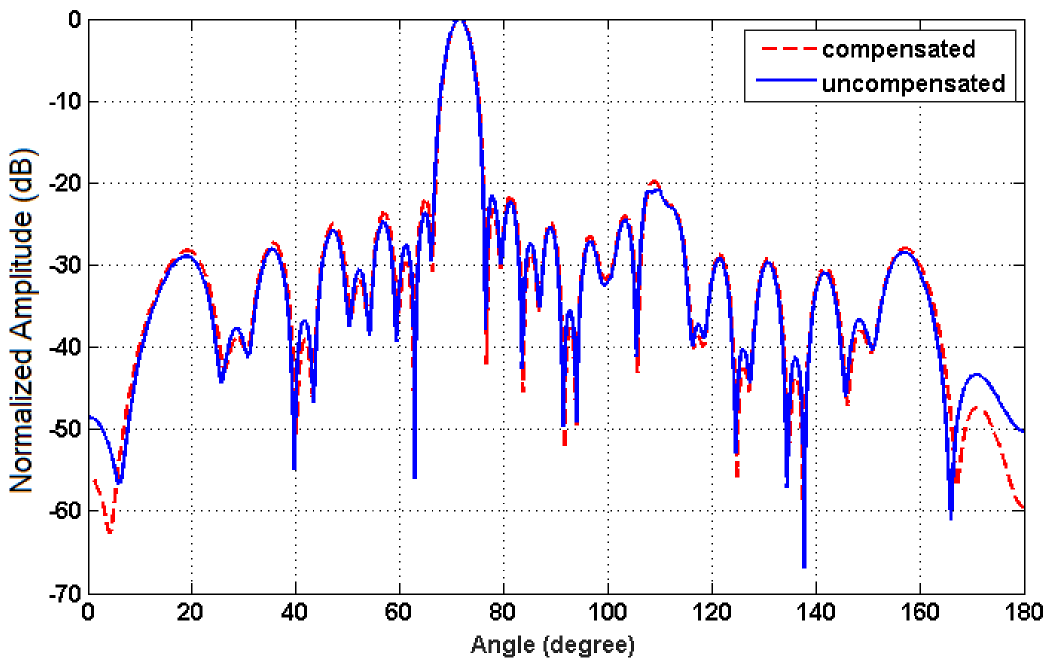

Figure 5.10: Normal and compensated sum patterns @3 GHz

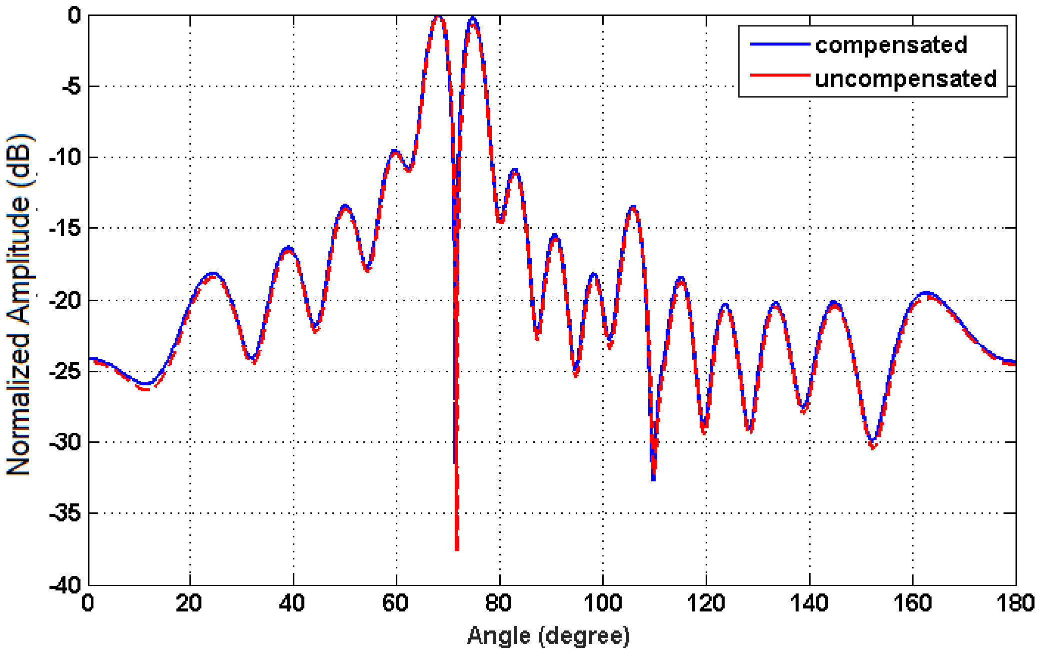

Figure 5.11: Normal and compensated difference patterns @3 GHz

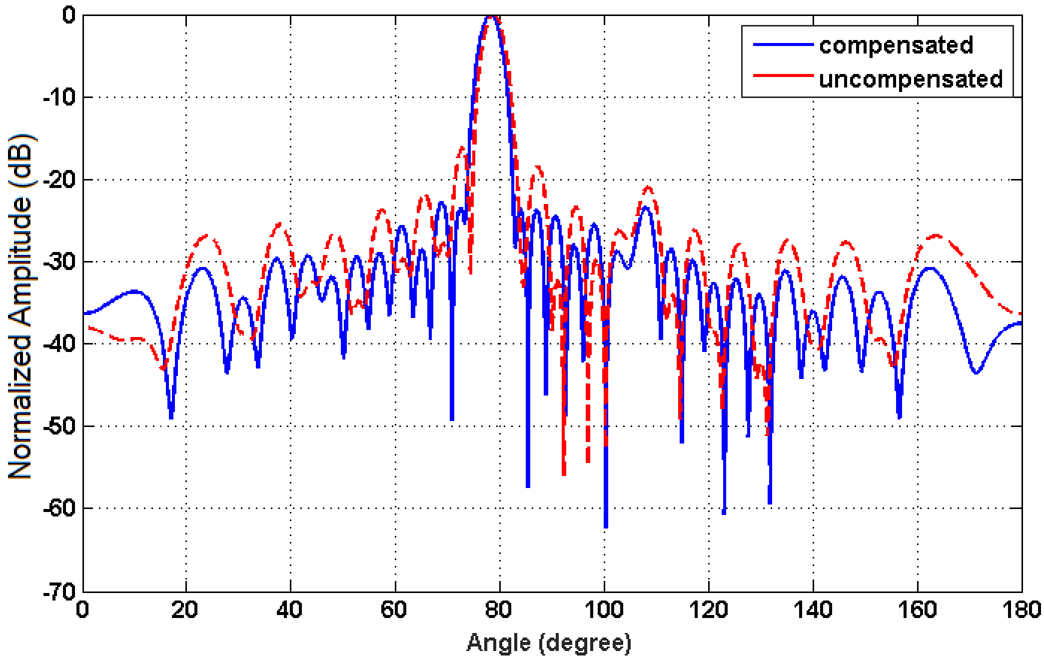

Figure 5.12: Normal and compensated sum patterns @3.2 GHz

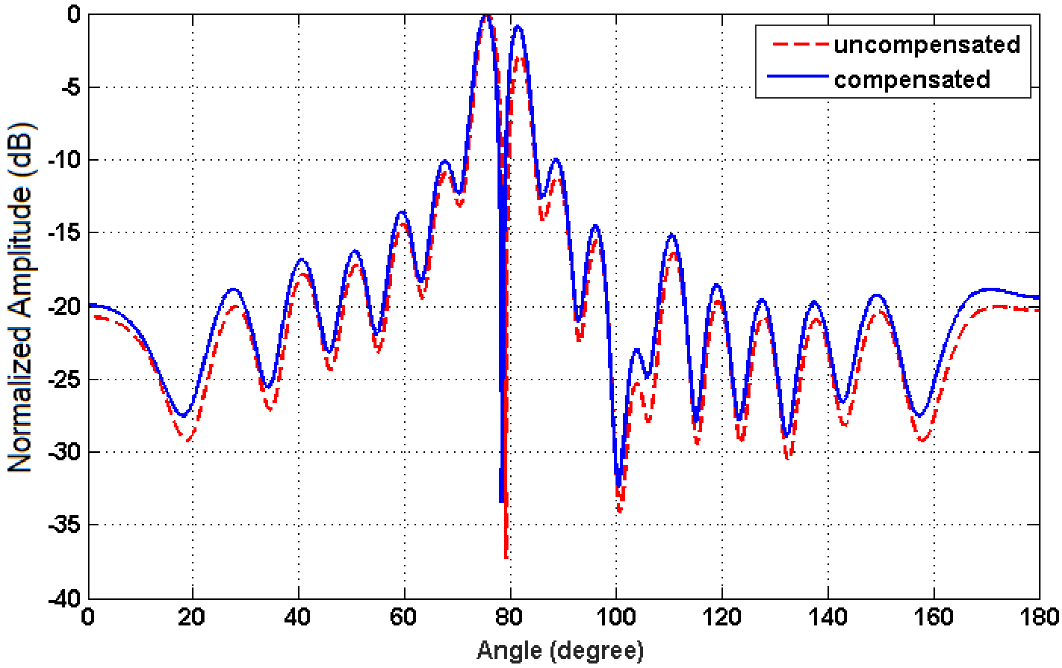

Figure 5.13: Normal and compensated difference patterns @3.2 GHz

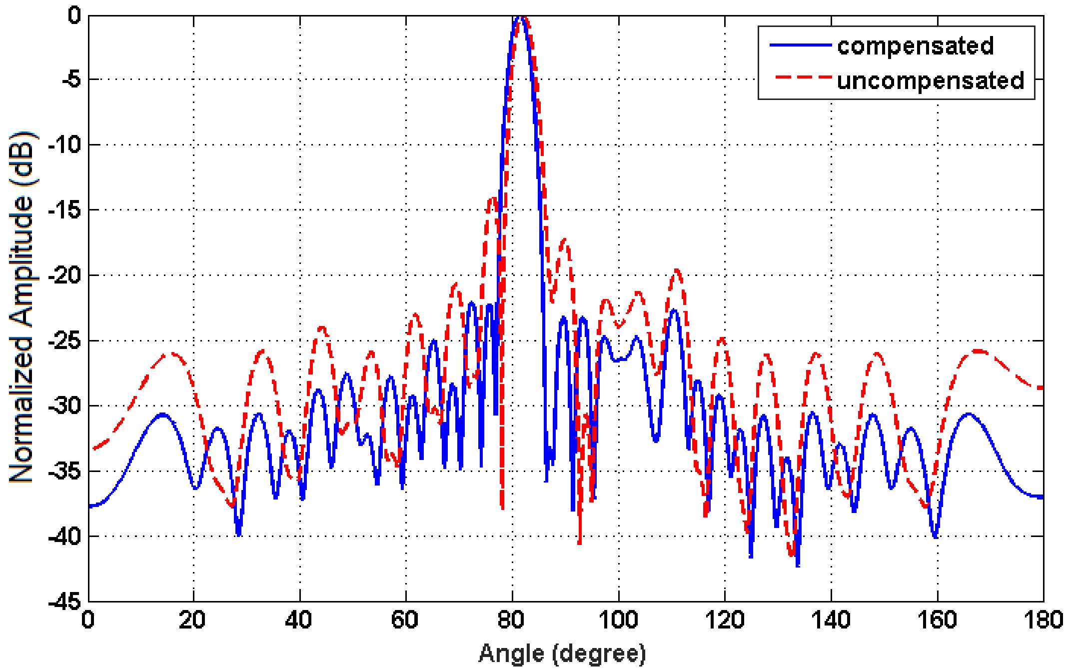

Figure 5.14: Normal and compensated sum patterns @3.3 GHz

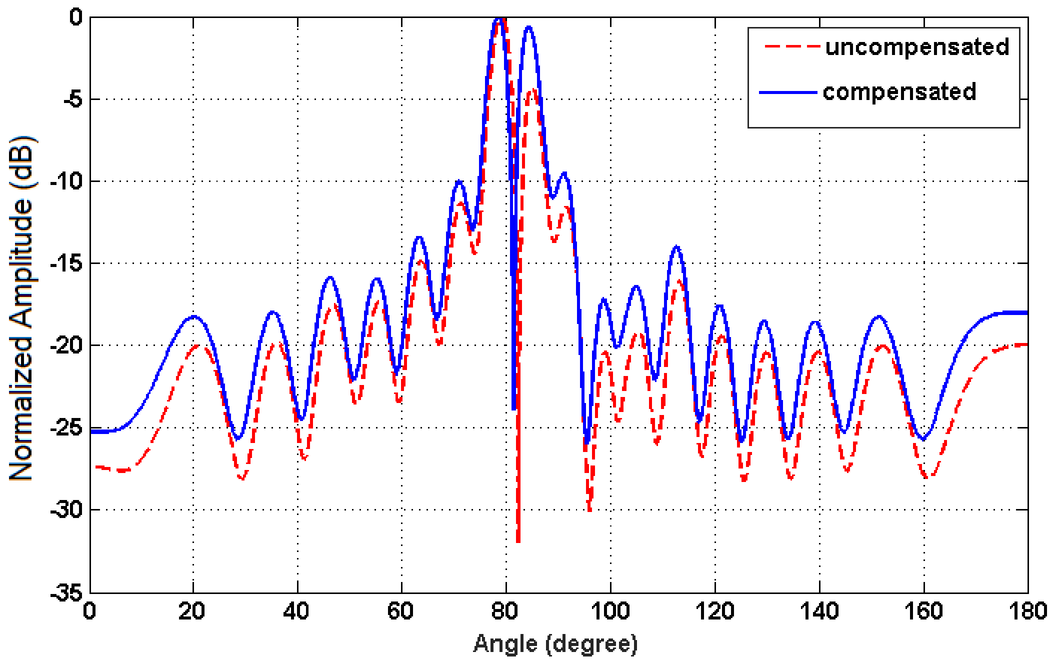

Figure 5.15: Normal and compensated difference patterns @3.3 GHz

It can be concluded that the improvement method decreases the undesired increase in side lobes due to the coupling between the sum and difference arrays. Also, it makes the top levels of the main beams of difference patterns equal. Actually, this shows that, with digital beamforming, desired patterns can be synthesized using the sum and difference patterns obtained from rows.

CHAPTER 6

MANUFACTURED PROTOTYPE OF MONOPULSE ARRAY

A 30-element array with 25 dB Taylor and Taylor-like difference amplitude distributions is designed in S-band. The array is scaled to operate around 6.2 GHz in order for the prototype to be easily manufactured. For a fast manufacturing purposes, the prototype consists of 5 sum and 5 difference rows.

Furthermore, to measure the prototype in anechoic chamber, an adapter should be designed. For this purpose, a transition from the non-standard waveguide to SMA connector is designed. The design of the adapter is presented in Section 6.1 These adapters are embedded into both sides of the array. The load side of the array is terminated via SMA 50Ω loads. The details of the production of the array is given in Section 6.2. Measured radiation patterns are presented and compared with simulations in Section 6.3. Finally, the specifications of the prototype are given in Section 6.4.

6.1 Ridged Waveguide to Coaxial Adapter Design

A transition from waveguide to coaxial connector is required for testing. So, an adapter which transmits power from the non-standard, ridged waveguide to SMA connector is designed. Impedance matching is provided by forming stepwise cavities on the ridge, and placing the SMA connector at the most suitable location on the transverse plane. Several images of the modelled adapter are given in Figure 6.1 and Figure 6.2. SMA connector is modelled by using its inner and outer diameters and a Teflon based dielectric material provided that its characteristic impedance is 50Ω.

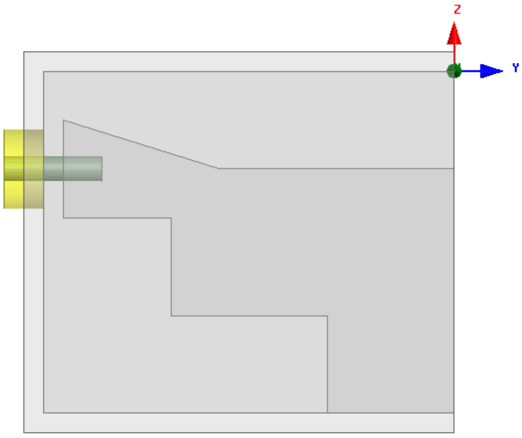

Figure 6.1: Right view of the adapter

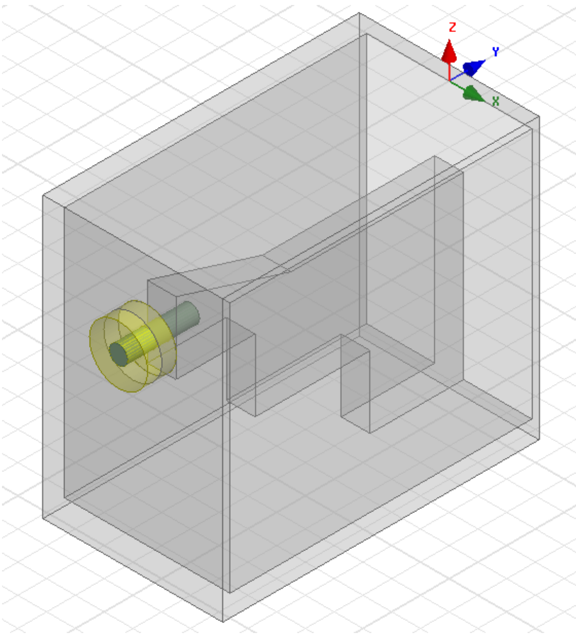

Figure 6.2: Isometric view of the adapter

On the SMA connector, a waveport is assigned between the inner and outer cylinders on the xz-plane shown in Figure 6.2. And, another waveport is assigned to the waveguide opening on the same plane. With this configuration, the model is simulated in HFSS. The return and insertion losses of the adapter are demonstrated in Figure 6.3 and Figure 6.4, respectively. It can be seen that the return loss of the adapter is below -22dB between 5.8 and 6.6 GHz. Hence, the adapter can be used without degrading the array performance.

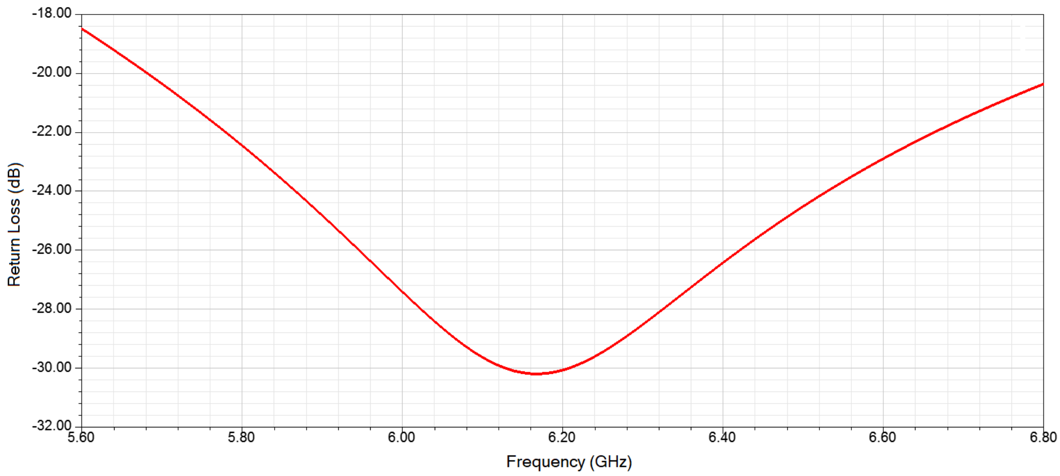

Figure 6.3: Return loss of the adapter

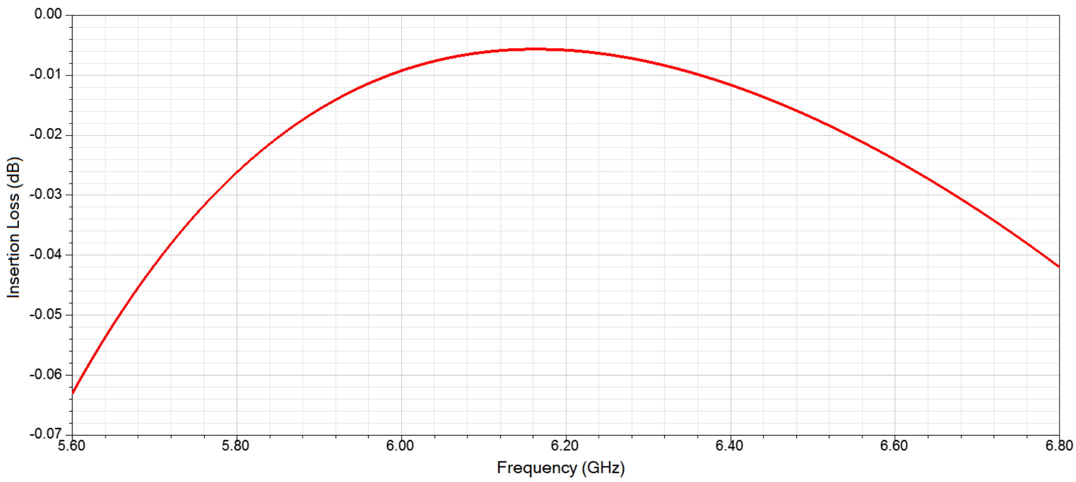

Figure 6.4: Insertion loss of the adapter

6.2 Manufacturing Process

The manufacturing process of the prototype is determined to be a fast one. So, the metallic waveguide section is divided into 2 parts for them to be bound later. The part with ridges and embedded adapter interface, as depicted in Figure 6.5, is produced using wire eroding, and CNC freeze. Then, the upper part with slots and mode suppressor walls, as depicted in Figure 6.6, is manufactured with wire eroding and CNC milling.

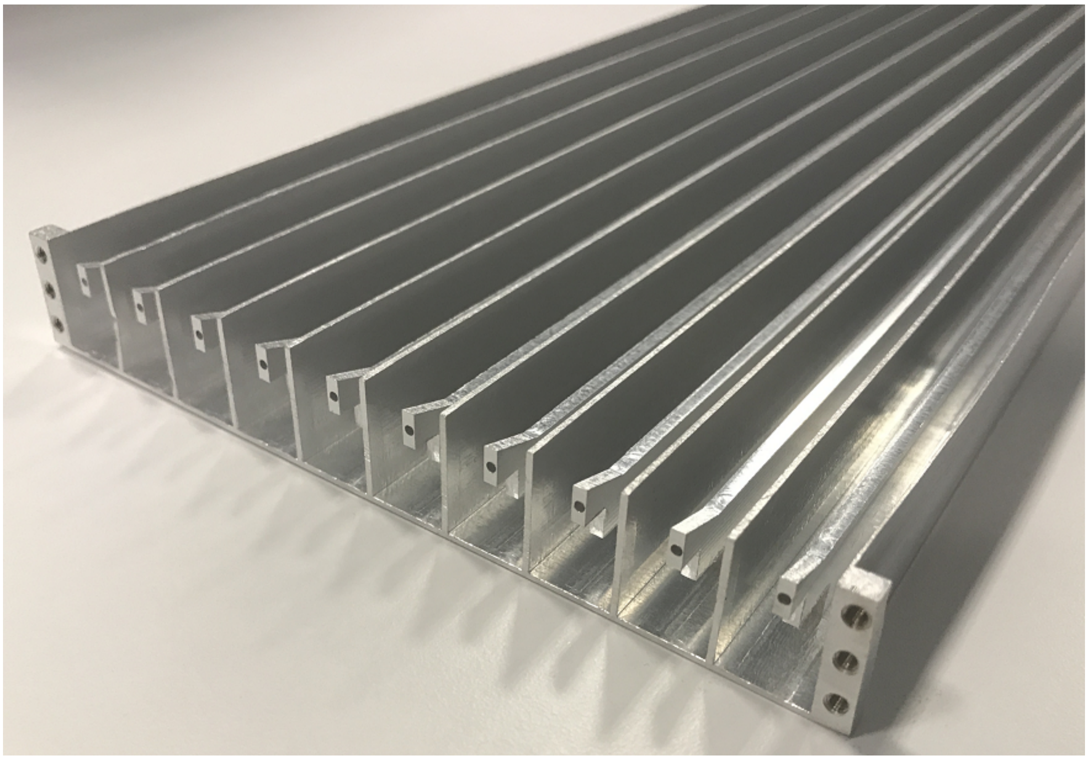

Figure 6.5: Waveguide part with ridges

Figure 6.6: Waveguide part with slots

Then, they are stuck together by using LOCTITE CF3350 film adhesive on the interface between the side walls and the upper wall of the waveguide. The combined structure is shown in Figure 6.7.

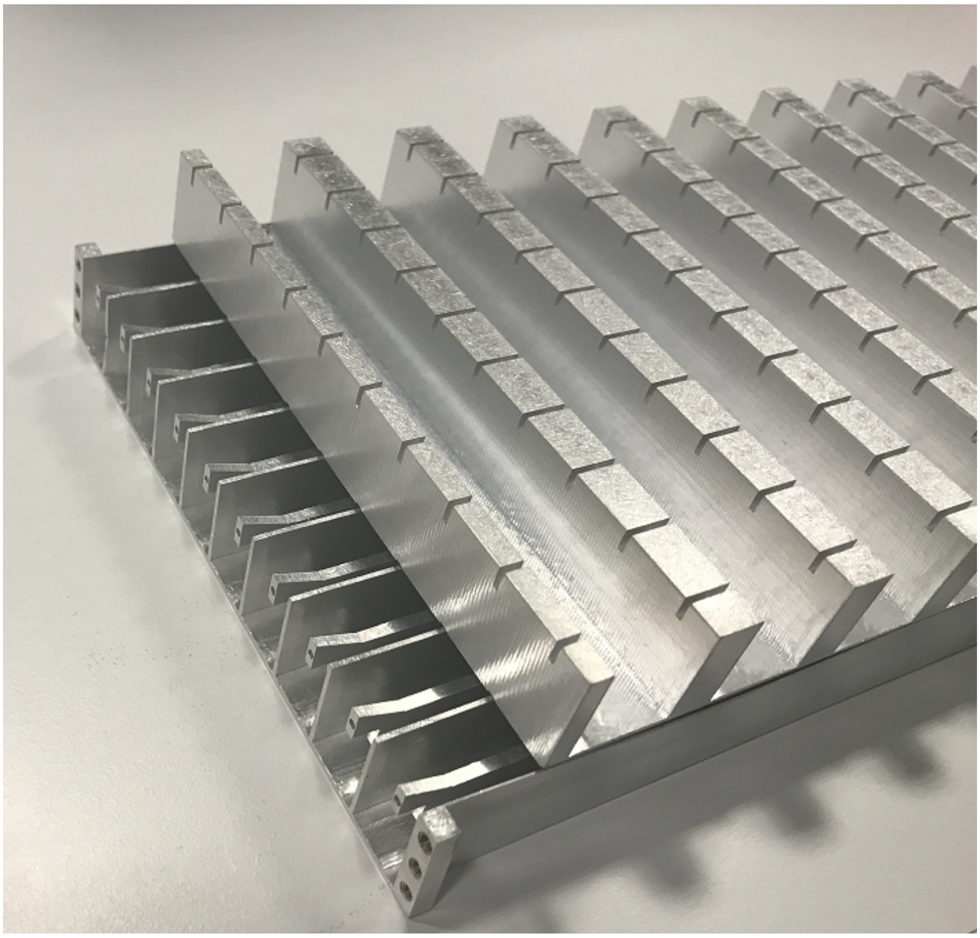

Figure 6.7: Combined metallic waveguide part

Next, the SMA adapter interface is manufactured via CNC milling. It is connected to the structure by using LOCTITE CF3350 film adhesive and screws as demonstrated in Figure 6.8.

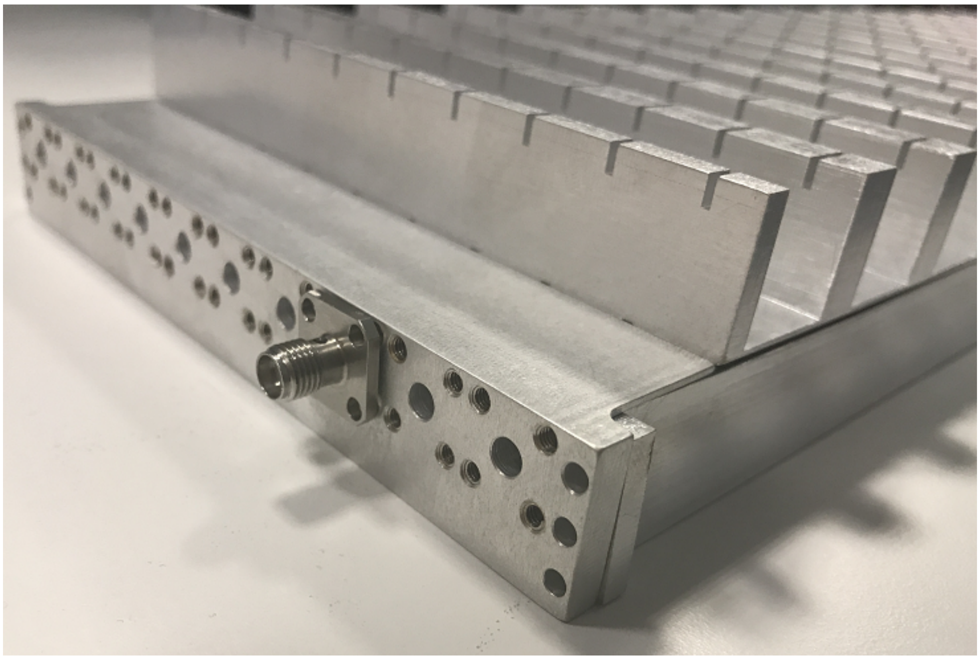

Figure 6.8: Combined metallic waveguide part with adapters

Finally, the 3-layer stripline-fed LTSAs are produced via standard multilayer PCB manufacturing process, and connected to the structure via silver epoxy. Note that one set of LTSAs includes 30 pieces for one sum row, and it is so for one difference row. The photograph of LTSA array is depicted in Figure 6.9. A picture of the combined array is given in Figure 6.10. Also, the final view of the array is depicted in Figure 6.11.

Figure 6.9: Manufactured LTSAs on a PCB

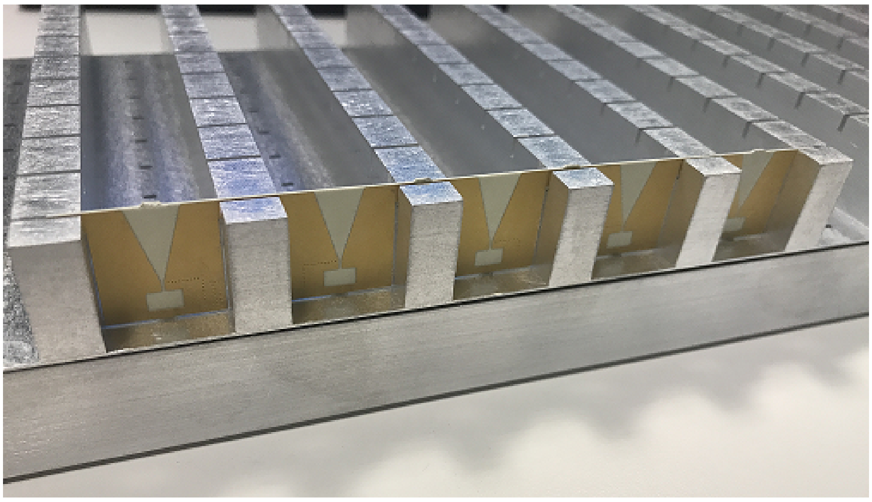

Figure 6.10: A visualization of a small portion of the full array

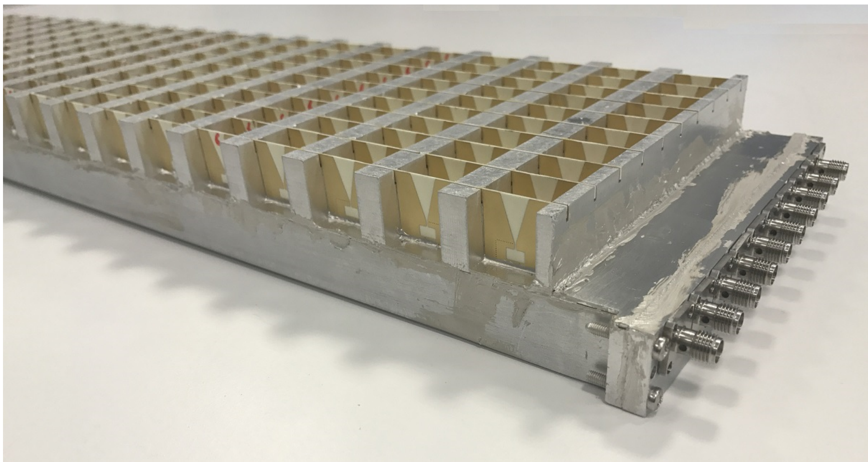

Figure 6.11: Monopulse array

6.3 Measurement Results

The radiation patterns of the manufactured array are measured in anechoic chamber as demonstrated in Figure 6.12. Planar near field measurement setup is used. The array is measured at five different frequencies, namely 5.8, 6.0, 6.2, 6.4, and 6.6 GHz, after the load side of the array is terminated via SMA 50Ω loads. In the measurements, WR137 probe antenna is used, whose lowest cutoff is 4.301 GHz, recommended frequency band is 5.85-8.20 GHz. The near field measurements are directly transformed into far field patterns by the setup. The radiation patterns from the NSI near-field measurement setup are given and compared with the simulated ones in Figure 6.13, Figure 6.14,Figure 6.15, Figure 6.16, and Figure 6.17 for 5.8, 6.0, 6.2, 6.4, and 6.6 GHz, respectively.

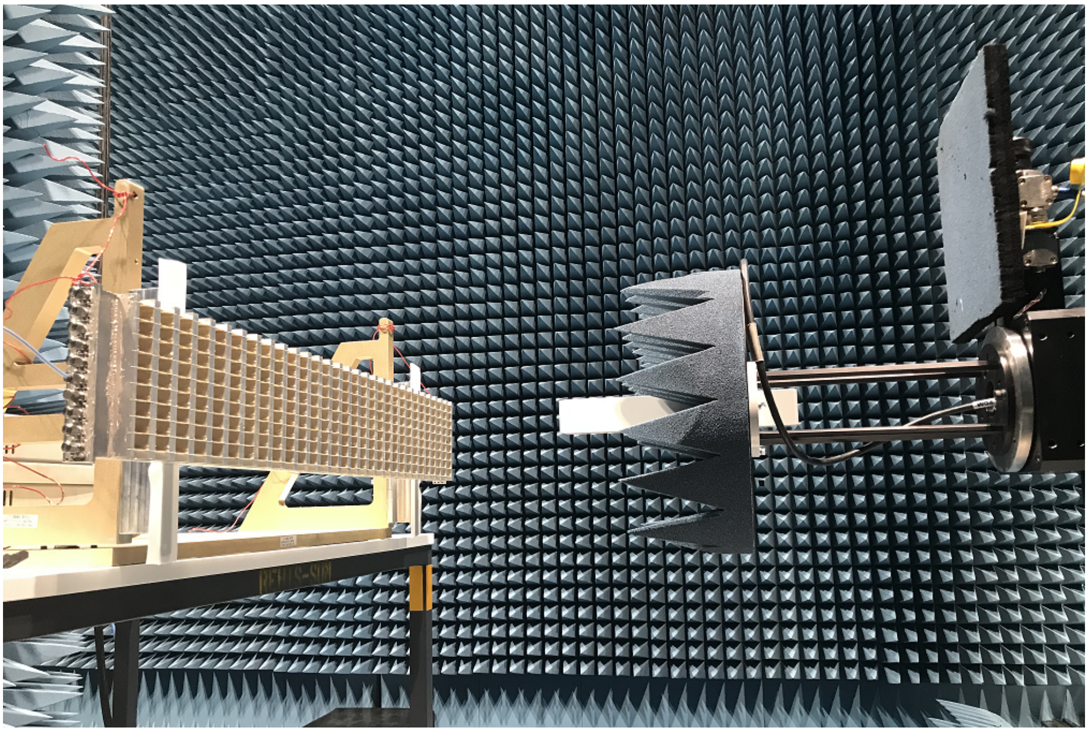

Figure 6.12: Monopulse array at NSI Near-Field Measurement Setup

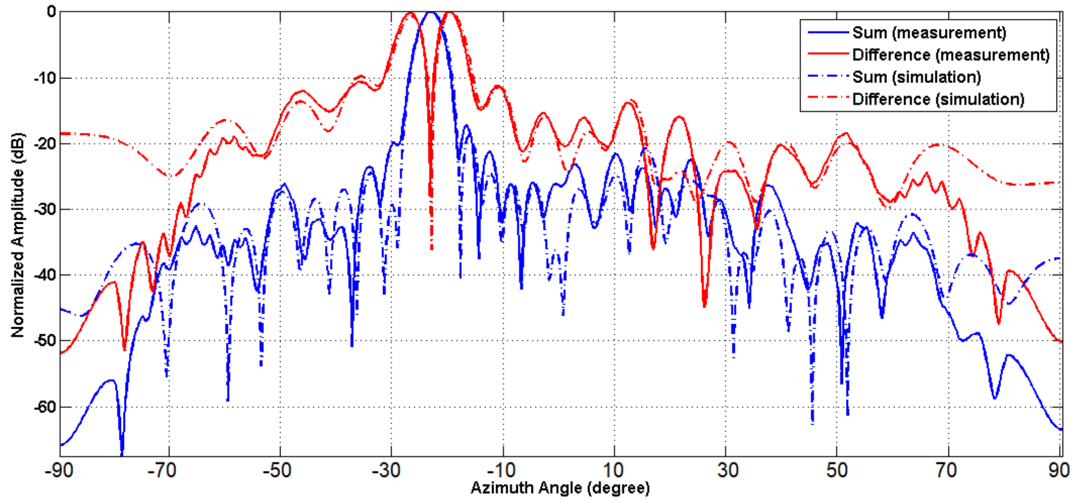

Figure 6.13: Measured patterns @5.8 GHz

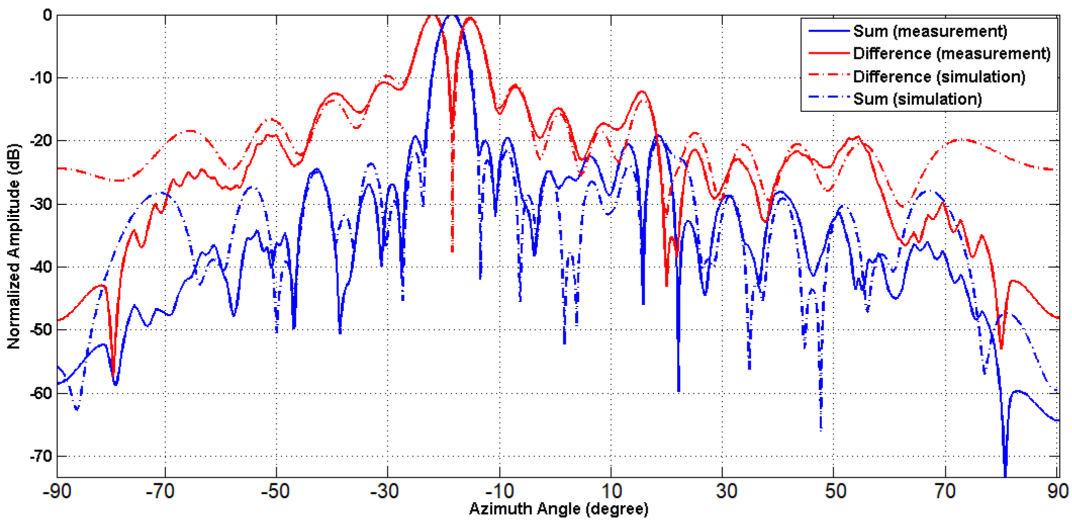

Figure 6.14: Measured patterns @6.0 GHz

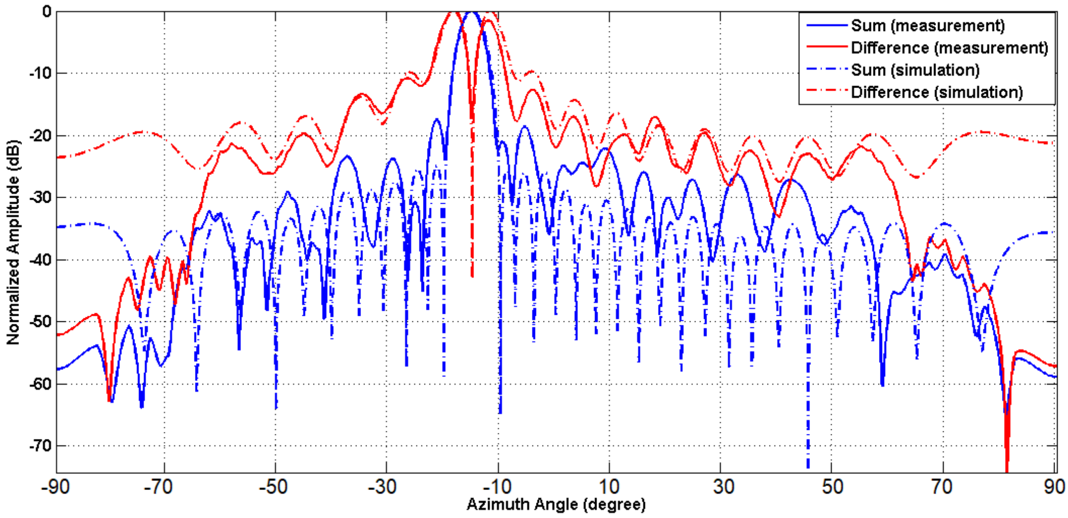

Figure 6.15: Measured patterns @6.2 GHz

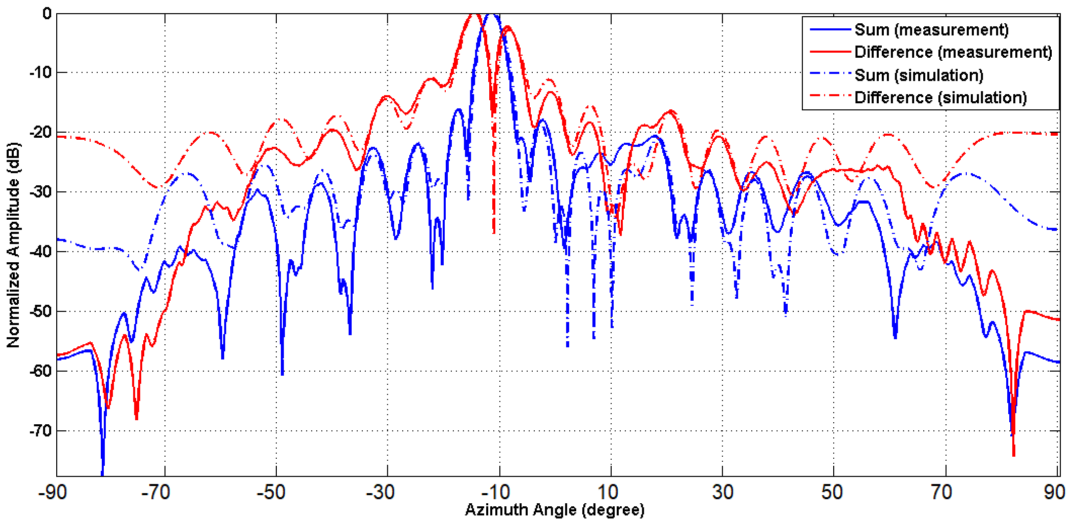

Figure 6.16: Measured patterns @6.4 GHz

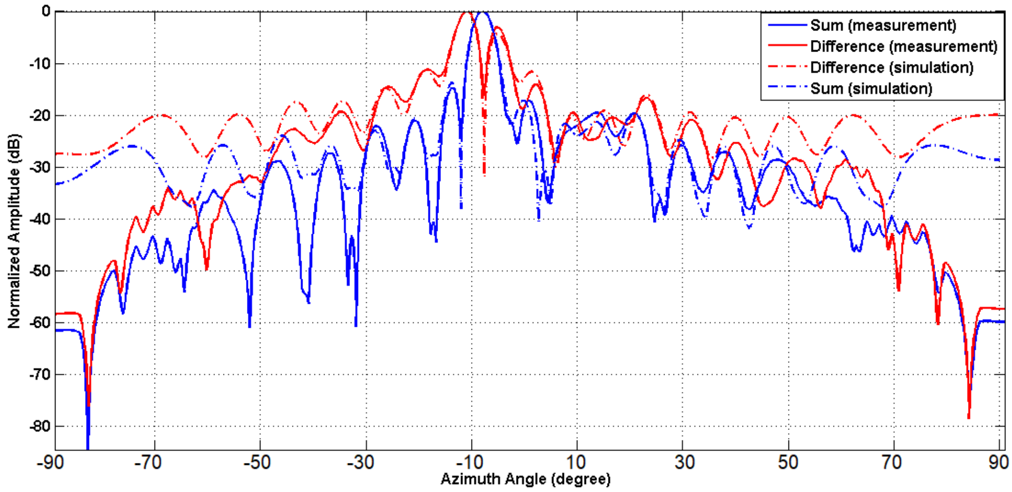

Figure 6.17: Measured patterns @6.6 GHz

It can be seen that the array can perform monopulse operation. Measurement results agree well with the simulations. There is a difference in far out side lobes of simulated and measured patterns. This is caused by the planar near-field measurement method. Although an increase in SLL is expected at frequencies other than the center frequency, the amount of increase is more than expected. This is mainly due to the errors in manufacturing and mechanical assembly. When LTSAs do not fit perfectly to its place, the amplitude and phase of the excitations deviates from desired values. This cause a degradation in radiation patterns. More professional production techniques such as brazing can be used to obtain arrays with better performance.

6.3.1 Improved Measurement Results

The increase in SLL can be eased if the digital beamforming method mentioned in Section 5.2 is applied. It is seen that the method provides an improvement on the measured results for the measured patterns. With the use of the method, SLL of sum patterns stays below -19 dB in the whole frequency band, and the top levels of the twin lobes in difference patterns are made equal. All improved sum and difference patterns are illustrated in Figure 6.18 and Figure 6.19, respectively.

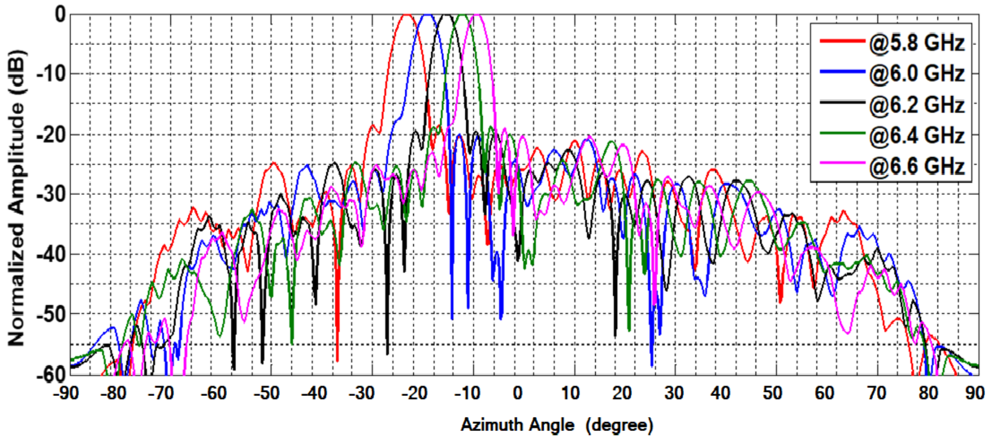

Figure 6.18: Improved sum patterns for all frequencies

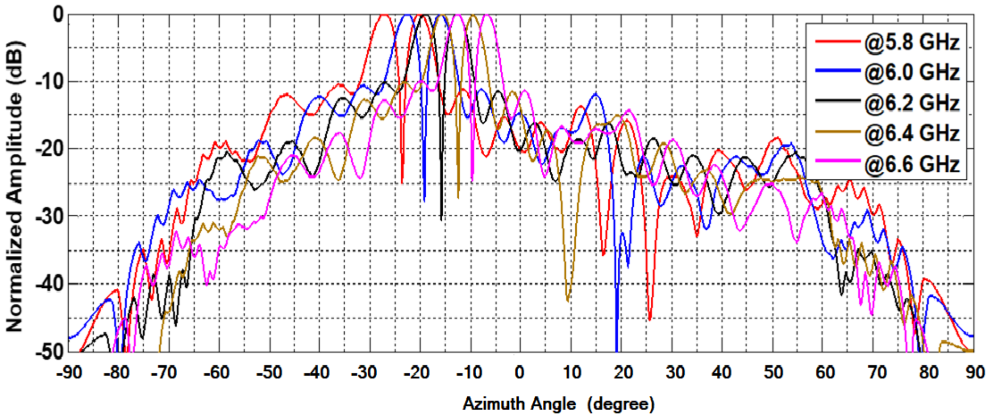

Figure 6.19: Improved difference patterns for all frequencies

Furthermore, the improved sum patterns of the measurement and simulations are demonstrated in Figure 6.20, Figure 6.21, and Figure 6.22 for 5.8, 6.2, and 6.6 GHz, respectively. Similarly, the improved difference patterns of the measurement and simulations are demonstrated in Figure 6.23, Figure 6.24, and Figure 6.25 for 5.8, 6.2, and 6.6 GHz, respectively. The difference between simulation and measurement is thought to be mainly due to manufacturing related errors as aforementioned. Note that the difference in far out side lobes (>70°) is due to the planar near-field measurement technique.

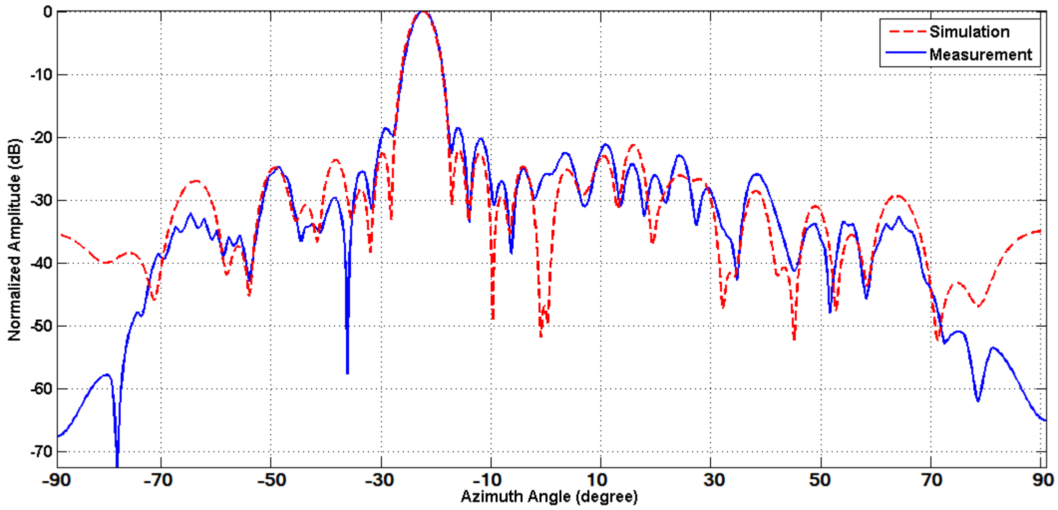

Figure 6.20: Comparison of simulation and measurement for the sum pattern @5.8 GHz

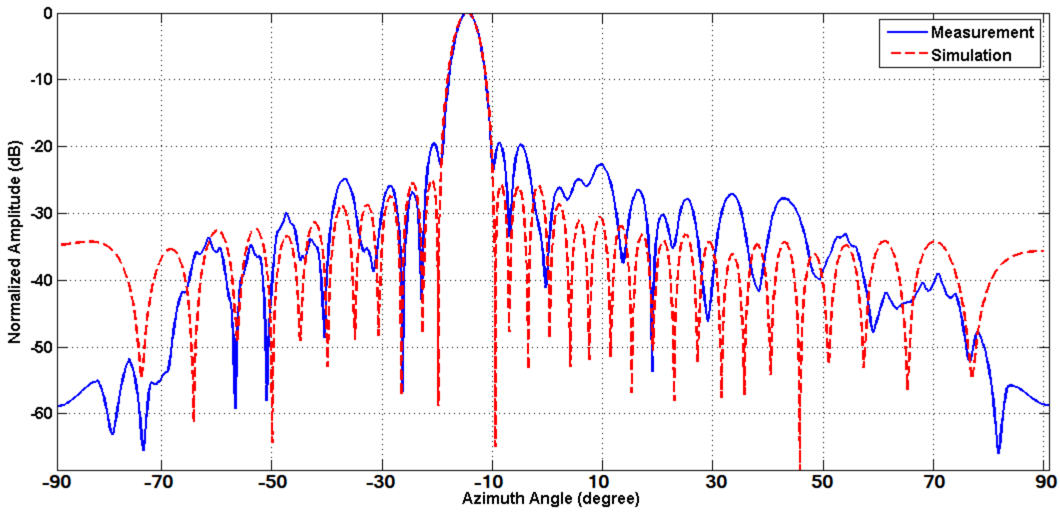

Figure 6.21: Comparison of simulation and measurement for the sum pattern @6.2 GHz

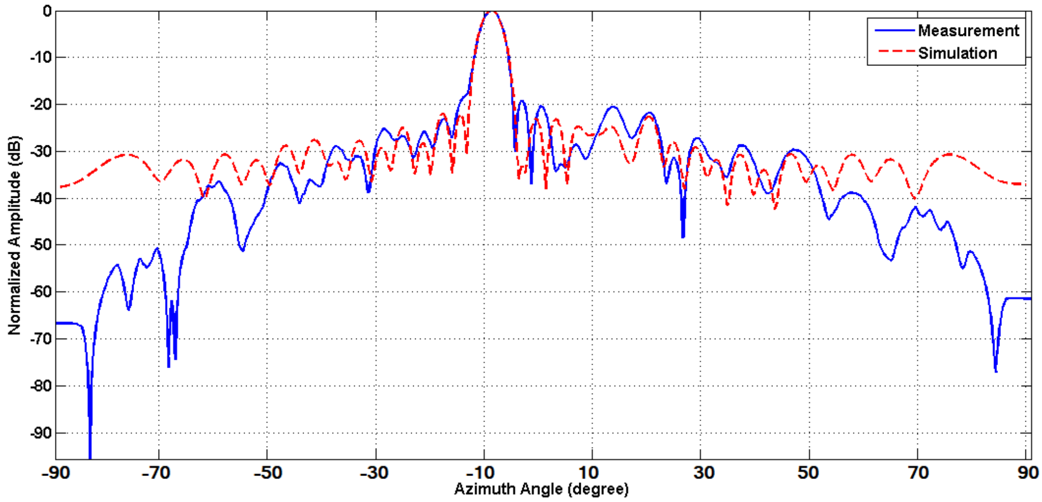

Figure 6.22: Comparison of simulation and measurement for the sum pattern @6.6 GHz

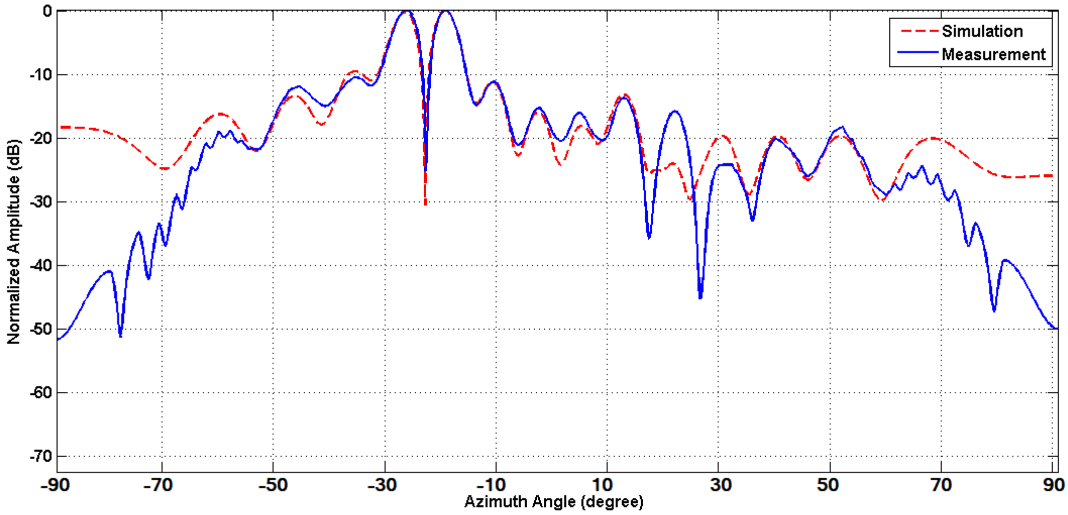

Figure 6.23: Comparison of simulation and measurement for the difference pattern @5.8 GHz

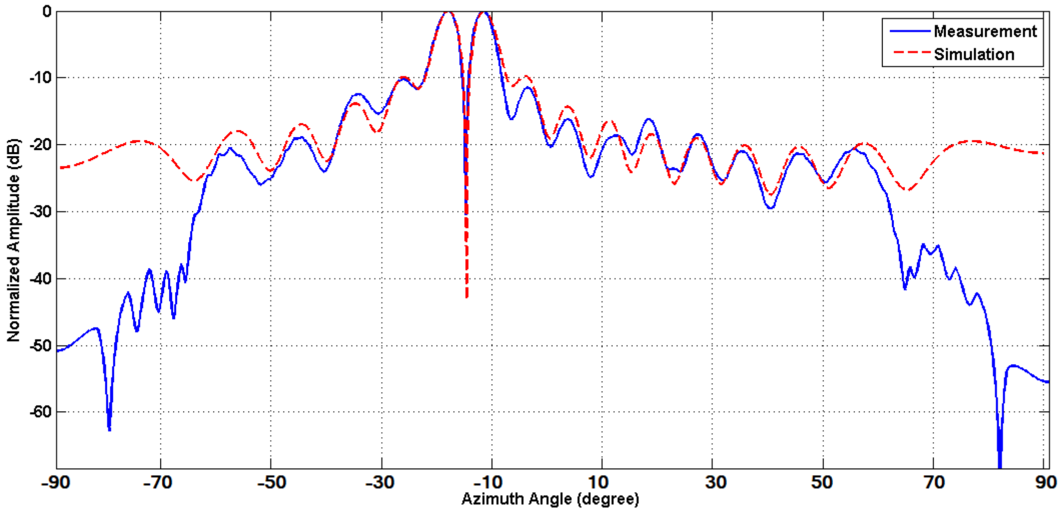

Figure 6.24: Comparison of simulation and measurement for the difference pattern @6.2 GHz

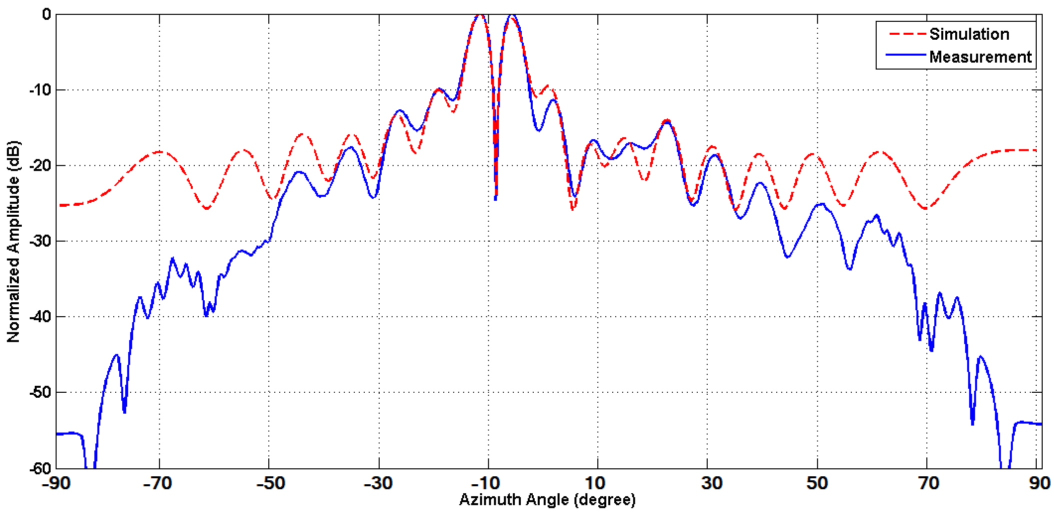

Figure 6.25: Comparison of simulation and measurement for the difference pattern @6.6 GHz

6.4 Specifications of the Manufactured Array

The specifications of the antenna listed in Table 6.1 based on the measurement results for the sake of completeness. The dimensions given belong to the manufactured prototype. While the data related to radiation patterns are obtained via planar near field measurements, the power delivered to the load (P_{load})is found measuring the scattering parameters via two-port network analyzer. Even if the unit cell is capable of operating in 20% bandwidth (offered) around the center frequency, in which the antenna has a 10 dB return loss, the measurements are performed in 13% one between 5.8 and 6.6 GHz since it is the desired operating bandwidth of the antenna.

Table6.1: Prototype Array's Specifications

Array length	750 mm
Array width	125 mm
Array height	35 mm
#of elements	30x5
Directivity	21.6 dB
Taper	25 dB
SLL @f_{center}	-20 dB
SLL_{max}	-19 dB
Null depth	below -25 dB
Operational bandwidth	13%
Offered bandwidth	20%
P_{load}	15%

CHAPTER 7

CONCLUSION

In this study, a novel antenna structure, which is the first of its kind in literature to the knowledge of author, for dual-plane monopulse operation is presented with its unique features. An S-band monopulse travelling-wave waveguide based antenna array is successfully designed with the use of non-offset longitudinal slots and printed antennas. LTSAs are used as printed antennas due to their wideband characteristics. Even though 400 MHz operational bandwidth, accounting for 13% around center frequency, is desired as it seems in radiation patterns, it offers 20% bandwidth, whereas regular closely-spaced slotted waveguide arrays provides a bandwidth no more than 10%. This is due to the fact that shrinking waveguide dimensions of slotted waveguide arrays makes the resonant behavior of the slots more intense. Indeed, the proposed hybrid topology can be said to increase the bandwidth of the closely spaced slotted waveguide arrays. For the 30-element array with 25 dB Taylor distribution, the sum array has an SLL below -22 dB in the operational bandwidth. Besides, the null depth of the difference pattern is -25 dB at worst.

It is expected that the efficiency of the array is close to 85% in the operational frequency band since the largest contribution for the losses comes from the power delivered to the load, which is 15%. The antenna can be made more efficient if the cross coupling between the closely spaced sum and difference rows is reduced. Otherwise, there is a trade-off between efficiency and SLL degradation across frequency band.

The proposed structure consists of slotted waveguide and printed LTSAs. Hence, it is easily manufactured with CNC machining techniques and standard PCB manufacturing process.

The characterization of the antennas of the designed array is performed by the application of unit cell based infinite array approach. For the excitation and phase control of an element, related parameters are swept when there is master and slave periodic boundary conditions, as well as a phase delay between these boundaries according to the travelling-wave array theory. An absorbing boundary condition, namely PML boundary, is applied to the upper surface of the unit cell.

Next, scattering parameters are extracted from simulation, and assigning a pseudo port to the PML boundary, the unit cell is represented as a 5-port network. Searching the elements with appropriate parameters for each element in the array according to the desired complex excitation constants, and cascading these 5-port networks using their scattering matrices in MATLAB™, an array with desired number of elements is realized easily without wasting time in simulations.

Finally, 30 by 5 interleaved sum and difference arrays have designed and manufactured. Manufactured prototype is measured in the planar near field measurement facility in Aselsan Inc. for the verification of the novel concept study. The measurements show that an operational monopulse array can be manufactured based on the novel structure. It is seen in the measurements that max SLL is -19 dB, and max null depth is -25 dB in the whole frequency band. The discrepancies between the measurements and the simulations are caused by fast manufacturing and assembly related problems. Besides, the concept is open to be improved. For instance, the cross coupling between closely spaced sum and difference rows degrades SLL and antenna efficiency. Thus, the study on the minimization of it is placed in the agenda as future work, as well as a design with Taylor and Bayliss distributions to lower SLL of difference rows. Furthermore, taking the scattering parameters at multiple frequencies while designing the array to handle coupling between rows in wideband is another issue as future work.

REFERENCES

[1] R. R. Kinsey, "An edge-slotted waveguide array with dual-plane monopulse," *IEEE Transactions on Antennas and Propagation*, vol. 47, no. 3, pp. 474-481, Mar. 1999.

[2] G. Gultepe, D. Dogan, O.A. Civi, "Bir tek darbe radar anten sistemi," Turkish Patent Institute 2016/18802, pending, 2016.

[3] R. R. Kinsey, "The an/tps-59 antenna row-board design," *Microwave Symposium Digest, 1974 S-MTT International*, Jun. 1974.

[4] A. E. Covington, "Some recollections of the radio and electrical engineering division of the National Research Council of Canada, 1946-1977," *Scientia Canadensis: Canadian Journal of the History of Science, Technology and Medicine*, vol. 15, no. 2, pp. 155-175, 1991.

[5] A. F. Stevenson, "Theory of slots in rectangular waveguides," *Journal of Applied Physics*, pp. 24-38, Jan. 1948.

[6] R. J. Stegen, "Longitudinal shunt slot characteristics," *Hughes Technical Memorandum, No. 261*, pp. 24-38, Nov. 1951.

[7] A. Oliner, "The impedance properties of narrow radiating slots in the broad face of rectangular waveguide: Part i - theory," *IRE Transactions on Antennas and Propagation*, vol.5, no.1, pp. 4-11, Jan. 1957.

[8] R. S. Elliott, "Traveling wave antennas," in *Antenna Theory and Design*, Hoboken, NJ: John Wiley, 2003, ch. 9.

[9] Y. T. Lo, S. W. Lee, "The design of waveguide-fed slot arrays," in *Antenna Handbook vol. 2*, New York: Van Nostrand Reinhold, 1988, ch. 12.

[10] T. A. Milligan, "Traveling-wave antennas," in *Modern Antenna Design*, Hoboken, NJ: John Wiley, 2005, ch. 10.

[11] D. Dogan, "Dual polarized slotted waveguide array antenna," Dept. Elect. Electron. Eng., Middle East Tech. Univ., Ankara, Turkey, 2011.

[12] M. I. Skolnik, "Tracking radar," *Radar Handbook 3rd. ed.*, D. D. Howard, New York: McGraw Hill, 2008, ch. 9.

[13] S. M. Sherman, D.K. Barton, "Terminology, definitions, and notation," *Monopulse Principles and Techniques*, Norwood, MA: Artech House, 2011, ch.2.

[14] D. K. Barton, S.A. Leonov, "Monopulse," *Radar Technology Encyclopedia*. Norwood, MA: Artech House, 1998, pp.275-278.

[15] S. M. Sherman, D.K. Barton, "Monopulse in array antennas," *Monopulse Principles and Techniques*, Norwood, MA: Artech House, 2011, ch. 7.

[16] S. M. Sherman, D.K. Barton, "Introduction," *Monopulse Principles and Techniques*, Norwood, MA: Artech House, 2011, ch. 1.

[17] S. M. Sherman, D.K. Barton, "Tracking radar applications of monopulse," *Monopulse Principles and Techniques*, Norwood, MA: Artech House, 2011, ch. 13.

[18] S. M. Sherman, D.K. Barton, "Components used in uonopulse," *Monopulse Principles and Techniques*, Norwood, MA: Artech House, 2011, ch 4.

[19] A. I. Leonov, K. I. Fominchev, "Monopulse radar," Foreign Technology Division US Air Force Systems Command, 1970.

[20] H. Wang, D. Fang, X. G. Chen, "A compact single layer monopulse microstrip antenna array," *IEEE Transactions on Antennas and Propagation*, vol. 54, pp. 503-509, Feb. 2006.

[21] Huang, Zhou, Chio, "Wideband dual-polarized and dual-monopulse compact array for sar system integration applications," *IEEE Geoscience and Remote Sensing Letters*, vol. 13, pp. 1203-1207, Jun. 2016.

[22] J. T. Branigan. U.S. patent 4,958,166. Sept. 18 1990.

[23] J. T. Nemit. U.S. patent 4,164,742. Aug. 14 1979.

[24] R. C. Laverick U.S. patent 3,636,563. Jan. 18 1972.

[25] W. Wu, J. Yin, N. Yuan, "Design of an efficient X-Band waveguide-fed microstrip patch array," *IEEE Transactions on Antennas and Propagation*, vol. 55, pp. 1933-1939, Jul. 2007.

[26] Rogers Corp. *Ro4003c™ high frequency material insertion loss comparison with other material types*[Online]. Available: https://www.rogerscorp.com

[27] Microtech Inc. *Rectangular rigid waveguide specifications*[Online]. Available: http://www.microtech-inc.com

[28] T.-S. Chen, "Calculation of the parameters of ridge waveguides," *IRE Transactions on Microwave Theory and Techniques*, vol. 5, pp . 12-17, Jan. 1957.

[29] M. Nagui. *VSWR Measuring Equipment and Techniques* [Online]. Available: http://www.doe.carleton.ca/ nagui/labequip/SWRmeter/SWRmeter.pdf

[30] P. J. Gibson, "The vivaldi aerial," *Microwave Conference 9th European*, vol.51, p.197, Sept. 1979.

[31] D. Schaubert, E. Kollberg, T. Korzeniowski, T. Thungren, J. Johansson, K. Yngvesson, "Endfire tapered slot antennas on dielectric substrates," *IEEE Transactions on Antennas and Propagation*, vol. 33, pp. 1392-1400, Dec. 1985.

[32] B. S. K. Lekshmi, I. J. Raglend, "Parametric study of tapered slot antenna for wide band applications," *International Conference on Computation of Power, Energy, Information and Communication*, pp. 71-77, Sept. 2015.

[33] G. R. Simpson "A generalized n-port cascade connection," *Microwave Symposium Digest, 1981 IEEE MTT-S International*, pp. 507-509, Jun. 1981.